THE EFFECT OF CRACKS ON THE DYNAMIC BEHAVIOR OF BARS AND SHAFTS

by

Kevin Ralph Collins

Thesis submitted to the Faculty of the

Virginia Polytechnic Institute and State University

in partial fulfillment of the requirements for the degree of

Master of Science

in

Civil Engineering

APPROVED:

Raymond H. Plaut, Chairman

Kamal B. Rojiani

Siegfried M. Holzer

November 29, 1989

Blacksburg, Virginia

THE EFFECT OF CRACKS ON THE DYNAMIC BEHAVIOR OF BARS AND SHAFTS

by

Kevin Ralph Collins

Raymond H. Plaut, Chairman

Civil Engineering

(ABSTRACT)

Nondestructive methods of detecting cracks in structural components and machinery are important, both in preventing failures and in establishing maintenance procedures. This thesis considers how the vibration behavior of cracked members can be modelled mathematically and how these mathematical models may lead to advancements in crack detection procedures. Two separate cases are considered: the longitudinal vibration of a cracked bar and the coupled vibrations of a cracked rotating shaft.

In the longitudinal vibration study, the equation of motion is developed for a cantilevered bar with a symmetric surface crack. Next, Galerkin's Method is used to obtain one- and two-term approximate solutions. Both forced and free vibrations of the bar are analyzed. Graphical results showing the relationships between displacement and crack size, crack position, and forcing frequency are presented and discussed. Spectral analysis is used to compare uncracked and cracked bar behavior. Finally, a sensitivity analysis of the forced vibration case is conducted to observe how the forcing frequency affects the rate of change of steady-state response at the onset of cracking.

In the second part of the thesis, a similar analysis is conducted for a cracked, simply-supported, Timoshenko shaft rotating at a constant angular speed. The equations of motion derived by Wauer (b) are used as the basis of the study. Again, Galerkin's Method is applied to obtain approximate solutions. Time histories and spectra are used to observe how changes in various parameters influence the vibration behavior. The effects of mass eccentricity and gravity are studied. Finally, the effect of a periodic axial impact load is considered.

Dedication

I would like to dedicate this thesis to my parents.

Acknowledgements

I would like to thank Dr. Raymond Plaut for his patience, his guidance, and his support throughout my work on this project. Also, I would like to thank Dr. Siegfried Holzer and Dr. Kamal Rojiani for their time in serving on my committee. Finally, I would like to acknowledge
of the Universität Karlsruhe in Karlsruhe, West Germany, whose work provided the basis for this research.

This research was supported by a Via Fellowship at Virginia Polytechnic Institute and State University and in part by the U.S. Army Research Office under Grant No. DAAL03-87-K-0040.

Table of Contents

List of Illustrations

List of Tables

Chapter 1

Introduction

1.1 Scope

The dynamic behavior of cracked structures is an interesting and potentially complex field of research which has received much attention in recent years. The complexity of the problem results from the nonlinearity introduced by the presence of a crack. Chang and Petroski (1986) summarized the influence of cracks on dynamic behavior by the following statement:

> The principal effects of cracks and other geometric discontinuities are to lower natural frequencies from those of the flawless structure, and to lower the local stiffness in the vicinity of the crack.

The importance of investigating such behavior cannot be overstated, since this type of information can be helpful in detecting cracks and avoiding crack-related failures.

This thesis investigates the dynamic behavior of cracked bars and shafts from a mathematical standpoint. In particular, two cases are considered. First, the longitudinal vibration of a cracked bar is investigated. Secondly, the coupled vibrations of a rotating shaft are analyzed. In both cases, the equations of motion are presented in dimensional form. These equations reflect changes in both

the stiffness and damping characteristics of the system due to the crack. Then, Galerkin's Method is used to obtain approximate solutions to the equations. The resulting equations are then nondimensionalized and solved exactly and/or numerically. Finally, relationships between various system parameters are illustrated in graphs and conclusions are drawn from them.

1.2 Literature Review

Surface cracks affect the dynamic behavior of any structure by introducing a nonlinearity into the governing equations of motion. In particular, a crack introduces nonlinearity in the stiffness (Mayes and Davies, 1980). However, Rogers and Hollingshead (1988) comment that the influence of a crack on the damping of the system also may be important. The following paragraphs provide a brief review of how such nonlinearities have been analyzed by other researchers.

A cracked shaft possesses many of the characteristics associated with a bilinear oscillator due to the changes in stiffness and/or damping at the crack location during the shaft's motion. The study of bilinear oscillators has received considerable attention. Natsiavas (a) provides an exact solution for a single-degree-of-freedom system which is strongly nonlinear and is subjected to harmonic excitation. In his model, he only considers nonlinearity in the restoring force. He also provides a systematic method of determining the integration constants, phase angles, and crossing points (i.e., the points at which the restoring force changes slope) for the bilinear system. Thompson et al. (1983) investigate bilinear oscillators using topological dynamics and discuss applications in marine technology. Furthermore, the authors provide a brief mathematical background for their bilinear formulation. Thompson, in collaboration with Ghaffari (1983) and with Stewart (1986), considers a damped oscillator with bilinear stiffness and investigates its behavior near resonance. They utilize numerical integration of known analytical solutions in each region of constant stiffness, changing the parameters at the appropriate switching points. In addition, they discuss some of the potential dangers of using numerical integration to detect resonant responses. Thompson and Elvey (1984)

use the concept of an oscillator with bilinear stiffness to model the behavior of mooring towers and discuss how higher damping can eliminate subharmonic resonances which are often prevalent in nonlinear systems. Shaw and Holmes (1983) consider a single-degree-of-freedom oscillator with bilinear stiffness subject to periodic forcing and linear damping. Choi and Noah (1988) consider a similar model subjected to harmonic excitation. In a pair of later papers, Shaw (1985a, b) considers the one-degree-of-freedom model constrained by symmetrical stops.

The concept of bilinear stiffness has many applications in material science. Zastrau (1985), in his analysis of cracks in reinforced concrete, discusses the crack-induced nonlinearity by using piecewise-linear force-displacement curves, both with and without gaps. Bert and Gordaninejad (1985) investigate multimodular materials and approximate the nonlinear stress-strain curves of these materials by piecewise-linear curves. They develop both closed-form solutions and transfer matrix solutions. Miller and Butler (1988) analyze the piecewise-linear restoring force of an elastic-perfectly plastic material by modelling the system as a single-degree-of-freedom oscillator using piecewise-linear stiffnesses to reflect the material behavior.

The above papers have focused entirely on nonlinear stiffness; they have not discussed the potential for nonlinear damping. However, as stated earlier, the effect of cracks on system damping may be an important factor to take into account in cracked structures. Shaw (1986) analyzes a system with a piecewise-linear dry friction characteristic. Dragani and Repaci (1979) investigate a single-degree-of-freedom system with stops in which both nonlinear stiffness and damping are considered. Bapat and Sankar (1986) also examine a single-degree-of-freedom model with piecewise-linear damping and stiffness. Likewise, Natsiavas (b) also treats nonlinearity in the damping by modelling both the stiffness and the damping as bilinear functions.

For nonlinear systems, the solution of the resulting equations of motion (if available) may be complex. Perturbation methods are used by Schmied and Krämer (1984), Wen and Wang (1988), and Gudmundson (1982). Modal analysis is also a common solution technique (Grabowski, 1980,1984; Feng et al., 1989). The use of Fourier series solutions is applied by Maezawa (1961),

Maezawa and Furukawa (1973), Maezawa et al. (1980), and Watanabe (1984). For complex modelling, the finite element method is utilized extensively (Bachschmid et al., 1984; Zastrau, 1985; Mayes and Davies, 1980; Grabowski, 1982,1984; Skrikerud and Bachmann, 1986; Gudmundson, 1983; Schmalhorst, 1988).

The first part of this thesis focuses on the longitudinal vibration of a cantilevered bar with a surface crack. Previous work on this topic is sparse. Gudmundson (1982) studies the longitudinal vibration of a bar with a central crack and a bar with a circular hole. He develops formulas for the "disturbed" eigenfrequencies in terms of crack parameters and the "undisturbed" eigenfrequencies. In a later paper (1983), Gudmundson discusses the coupling of longitudinal and bending deformation for a beam in which the crack remains open at all times. Dentsoras and Dimarogonas (1983) consider a cantilever beam with a crack at the fixed end and subjected to a longitudinal harmonic force. They use the Paris-Erdogan model of fatigue crack propagation and focus on crack propagation at or near resonance. Haisty and Springer (1985) investigate two crack models for the longitudinal vibration of a cracked uniform beam. One model utilizes a linear spring, while the second model incorporates a reduced cross-section in the cracked region. Springer et al. (1987) develop a model of a cracked longitudinal beam which can be used to predict shifts in the natural frequency caused by the discontinuity. An interesting feature of their work is the application of an analogy between the potential flow theory of fluids and the longitudinal vibration theory of solids to develop a relationship between crack length and damaged area. Lastly, Papadopoulos and Dimarogonas (1988) focus on the coupling of flexural and longitudinal vibration in their study of a cracked shaft in which the crack is assumed to remain open. Their work examines both forced and free vibrations.

The second part of this thesis discusses the results of an analysis of the vibrational behavior of a rotating shaft. Much attention has been focused on this topic. Muszynska (1982) investigates cracked shafts with non-symmetric cross-sections. Schmied and Krämer (1984), in their analysis, incorporate a continuous function to model the opening and closing of a breathing crack. Similarly, Papadopoulos and Dimarogonas (1988) model the time-varying stiffness of the crack as a truncated

cosine series. Gasch et al. (1988), in dealing with hollow shafts, provide a comparison of results between simplified crack models and "exact" crack models based on thin-walled shell theory. Ichimonji and Watanabe (1988) consider a simple rotor model with a crack oriented at 45 degrees with respect to the shaft axis and model the breathing nature of the crack by considering torsional deflections. The above-mentioned literature is just a brief sample; for additional information, the interested reader is referred to a comprehensive literature survey by Wauer (a).

As a final note, nonlinearities in a rotating shaft can be introduced by other mechanisms in addition to cracks, and the resulting behavior may be similar to that of a cracked shaft. In a set of papers by Neilson and Barr (1987, 1988a, 1988b), nonlinear behavior is introduced into the model by piecewise-linear support conditions. Choi and Noah (1987) consider the equations of motion which incorporate piecewise-linear bearing forces.

Chapter 2

Longitudinal Vibration of a Cracked Bar

2.1 Physical Model

The physical model for the longitudinal vibration study is as shown in Figure 2.1(a). The model consists of a horizontal cantilevered bar of length L subjected to harmonic excitation. The bar is fixed at the left end and free at the right end. A right-handed coordinate system is located at the left end, with the x-axis coinciding with the centroidal axis of the bar. The bar is uniform and is composed of a homogeneous, linearly elastic material. The following notation is used to describe the properties (dimensional quantities) of the bar:

E = modulus of elasticity of the material (constant)

A = cross-sectional area of the bar (constant)

μ = mass per unit length (constant)

ε = crack width parameter

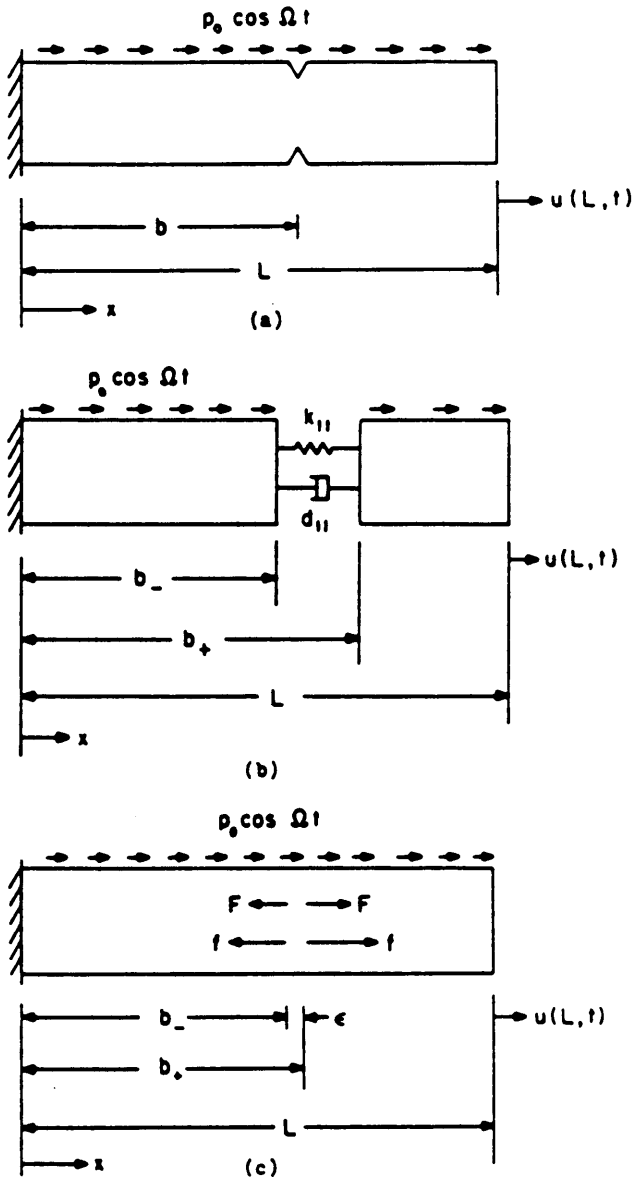

Figure 2.1. Models: (a) Physical model for longitudinal vibration; (b) Model in which spring and dashpot represent elastic and damping properties at the crack; (c) Uniform bar with generalized forces F and f which model the local change in stiffness and damping for an open crack.

d_e = external viscous damping coefficient

d_i = internal (viscoelastic) damping coefficient

d_c = dry friction damping coefficient at the crack

t = time

$p(x, t) = p_0 \cos \Omega t$ = imposed harmonic excitation distributed along the bar

$u(x, t)$ = axial displacement

b = crack location $(0 < b < L)$

The crack is assumed to be configured so that bending of the shaft will not take place (i.e., symmetric discontinuity).

An important observation to make at this point is that since the bar is horizontal, with gravity assumed to act downward, the effect of gravity will not play a role in the following analysis. The effect of gravity may play an important role in the vibrational behavior of other bar configurations.

2.2 Mathematical Model

The basis for the mathematical model is shown in Figure 2.1(b) and Figure 2.1(c). The development of the field equations follows that used by Wauer (b) in modelling a cracked rotating shaft and therefore many of the details will not be included here. Figure 2.1(b) illustrates the use of a spring and dashpot to represent the stiffness and damping, respectively, of the crack. The spring stiffness is defined as k_{11} and the damping coefficient of the dashpot is defined as d_{11}. It is assumed in the following development that $d_{11} = d_i k_{11}$. Figure 2.1(c) shows how generalized forces can be

used to model a crack in a uniform bar. The elastic properties of the crack are replaced by a pair of self-equilibrating forces F located at x = b. Similarly, the viscous properties of the crack are replaced by a pair of self-equilibrating forces f at x = b. These forces are present only when the crack is to be open; they disappear when the crack is considered closed. This concept of modelling the properties of the crack by generalized forces follows that of Kirmser (1944), Thomson (1949), Petroski (1981), Petroski and Glazik (1980) and Chang and Petroski (1986). For $0 < x < b_-$ and $b_+ < x < L$, where

$$b_+ = b + \frac{\varepsilon}{2} \tag{2.1a}$$

$$b_- = b - \frac{\varepsilon}{2} \tag{2.1b}$$

$$b_+ - b_- = \varepsilon \to 0 \tag{2.1c}$$

the governing equation can be written as

$$\mu u_{tt} + d_e \mu u_t + (1 - \Lambda) d_c \delta(x - b) \mu u_t - \mathrm{EA}(u_{xx} + d_i u_{txx}) = p_0 \cos \Omega t \tag{2.2}$$

The subscripts t and x refer to partial derivatives with respect to time and axial coordinate, respectively, and $\delta(x - b)$ is the Dirac delta function. The value of Λ determines which terms remain in the equation for an open or closed crack. Mathematically,

$$\Lambda = \begin{cases} 1 \text{ for an open crack} \\ 0 \text{ for a closed crack} \end{cases} \tag{2.3}$$

For the given problem, the boundary conditions are

$$u(0,t) = 0 \tag{2.4a}$$

$$\mathrm{EA}(u_x + d_i u_{tx})\big|_{(L,t)} = 0 \tag{2.4b}$$

At the crack, the transition conditions for a closed crack are

$$u(b_+, t) = u(b_-, t) \tag{2.5a}$$

$$u_t(b_+, t) = u_t(b_-, t) \tag{2.5b}$$

and for an open crack they are

$$EA(u_x + d_i u_{tx})|_{(b_-, t)} = EA(u_x + d_i u_{tx})|_{(b_+, t)} \tag{2.6a}$$

$$EA(u_x + d_i u_{tx})|_{(b_-, t)} = k_{11}[u(b_+, t) - u(b_-, t)] + d_{11}[u_t(b_+, t) - u_t(b_-, t)] \tag{2.6b}$$

In (2.2), the Dirac delta function acts to incorporate the friction component of the system damping created when the crack is closed. During the bar's motion, the crack will be open for part of the cycle and closed at all other times. In actuality, this opening and closing is continuous and is commonly referred to as a "breathing" crack. However, for simplicity, this development will assume that at any point in the cycle the crack is either completely open or completely closed. During the portion of the cycle when the crack is closed, the friction at the interface of the crack will be modelled by modifying the external damping so that

$$d_e = \begin{cases} d_e \text{ for an open crack} \\ d_e + d_c\delta(x - b) \text{ for a closed crack} \end{cases} \tag{2.7}$$

The net effect of the above assumptions about crack breathing and dry friction is to create a system with piecewise-linear stiffness and damping characteristics.

The equation of motion for the piecewise-linear system can be shown to be (for $0 < x < L$)

$$\begin{aligned} &\mu u_{tt} + d_e\mu u_t + (1 - \Lambda)d_c\delta(x - b)\mu u_t - EAu_{xx} - EAd_i u_{txx} \\ &- \Lambda(F + f)[\delta(x - b_+) - \delta(x - b_-)] - p_0 \cos \Omega t = 0 \end{aligned} \tag{2.8}$$

where Λ is as defined in (2.3). The quantity (F + f) can be defined in terms of the axial displacement $u(x, t)$ as follows. From a simple static calculation, the relative displacement at the crack is

$$u(b_+, t) - u(b_-, t) = \varepsilon \frac{F(t)}{EA} \tag{2.9}$$

Similarly, the viscous damping is assumed to be of the form

$$u_t(b_+, t) - u_t(b_-, t) = \varepsilon \frac{f(t)}{d_i EA} \tag{2.10}$$

The compliance at the crack, c_{11}, is defined by

$$u(b_+, t) - u(b_-, t) = c_{11} EA u_x(b, t) \tag{2.11}$$

where $c_{11} = \frac{1}{k_{11}}$ (see Figure 2.1b) and the value of u_x can be evaluated at $x = b_+$ or $x = b_-$. Then

$$u_t(b_+, t) - u_t(b_-, t) = c_{11} EA u_{tx}(b, t) \tag{2.12}$$

Combining (2.11) and (2.12) and using (2.9) and (2.10), one obtains

$$F + f = \frac{1}{\varepsilon} (EA)^2 c_{11} (u_x + d_i u_{tx})|_{(b,t)} \tag{2.13}$$

Papadopoulos and Dimarogonas (1988) provide values of a nondimensional crack compliance which is a function of the ratio of the crack depth and the bar diameter. These values are based on a crack which is only on one side of the bar, so that the crack is not a symmetric discontinuity. However, even though the crack model used in this thesis assumes a symmetric discontinuity, the values of c_{11} in their paper (see Figure 3 of Papadopoulos and Dimarogonas, 1988) will be used in the nondimensional equations which will be developed in the upcoming paragraphs. This is unfortunate, but it is unavoidable since the references do not provide data for compliances based on symmetric discontinuities. This thesis will focus on small crack depths (i.e., ratios of crack depth to bar diameter between 0 and 0.2).

In order to obtain approximate solutions to the above equation of motion, Galerkin's Method is applied. The assumed solution $u(x, t)$ is written as a finite sum of products of a function of time

and a function of the coordinate x, where the function of x must satisfy all of the boundary conditions in (2.4). A choice of $u(x, t)$ which satisfies the above is

$$u(x, t) = \sum_{k=1}^{N} u_k(t) \sin \theta_k x \tag{2.14}$$

where

$$\theta_k = \frac{2k-1}{2L}\pi \tag{2.15}$$

The above function for $u(x, t)$ is substituted into the left side of the equation of motion and the result is made orthogonal to each function of x included in the series. That is, after multiplying through by $\sin \theta_n x$ (where the subscript n identifies the integer value of each assumed mode shape k), integrating both sides of the equation from 0 to L, and using the orthogonality property of the sine functions, one obtains a set of N ordinary differential equations with respect to time. During the above procedure, when integrating the Dirac delta functions $\delta(x - b_+)$ and $\delta(x - b_-)$, it is helpful to simplify the results by using trigonometric identities in conjunction with equations (2.1). For example,

$$\begin{aligned}\int_0^L [\delta(x-b_+) - \delta(x-b_-)] \sin \theta_n x \, dx &= \sin \theta_n b_+ - \sin \theta_n b_- \\ &= \sin\left(\theta_n b + \theta_n \tfrac{\varepsilon}{2}\right) - \sin\left(\theta_n b - \theta_n \tfrac{\varepsilon}{2}\right) \\ &= 2 \sin\left(\theta_n \tfrac{\varepsilon}{2}\right) \cos(\theta_n b) \\ &\simeq \varepsilon \theta_n \cos \theta_n b\end{aligned} \tag{2.16}$$

assuming in the last step that $\varepsilon\theta_n$ is small. Following the integration, one arrives at the following nondimensional form of the ordinary differential equations:

$$\frac{d^2\tilde{u}_n}{d\tau^2} + \tilde{d}_e \frac{d\tilde{u}_n}{d\tau} + (1-\Lambda)\tilde{d}_c \sin\gamma_n\tilde{b}\sum_{k=1}^{N}(\sin\gamma_k\tilde{b})\frac{d\tilde{u}_k}{d\tau}$$
$$+ \tilde{d}_i(2n-1)^2\frac{d\tilde{u}_n}{d\tau} + (2n-1)^2\tilde{u}_n - \Lambda\tilde{c}_{11}(2n-1)\cos\gamma_n\tilde{b}\sum_{k=1}^{N}(2k-1)(\cos\gamma_k\tilde{b})\tilde{u}_k \qquad (2.17)$$
$$- \Lambda\tilde{c}_{11}\tilde{d}_i(2n-1)\cos\gamma_n\tilde{b}\sum_{k=1}^{N}(2k-1)(\cos\gamma_k\tilde{b})\frac{d\tilde{u}_k}{d\tau} = \frac{1}{(2n-1)}\cos\tilde{\Omega}\tau$$
$$n = 1, 2, ..., N$$

where the nondimensional quantities (represented by the superscript ~) are

$$\tilde{d}_e = \frac{2L}{\pi}\sqrt{\frac{\mu}{EA}}\,d_e \qquad (2.18a)$$

$$\tilde{d}_c = \frac{4}{\pi}\sqrt{\frac{\mu}{EA}}\,d_c \qquad (2.18b)$$

$$\tilde{d}_i = \frac{\pi}{2L}\sqrt{\frac{EA}{\mu}}\,d_i \qquad (2.18c)$$

$$\tilde{c}_{11} = \frac{2EA}{L}\,c_{11} \qquad (2.18d)$$

$$\tilde{\Omega} = \frac{2L}{\pi}\sqrt{\frac{\mu}{EA}}\,\Omega \qquad (2.18e)$$

$$\tilde{u}_n = \frac{\pi^3 EA}{16L^2 p_0}\,u_n \qquad (2.18f)$$

$$\tilde{b} = \frac{b}{L} \qquad (2.18g)$$

$$\gamma_n = \theta_n L = \frac{2n-1}{2}\pi \qquad (2.18h)$$

The variable τ represents the nondimensional time parameter and is equal to

$$\tau = \frac{\pi}{2L}\sqrt{\frac{EA}{\mu}}\, t \tag{2.18i}$$

Due to the breathing crack, a transition condition is necessary to determine the value of Λ. For longitudinal vibration, Λ is determined by evaluating the axial strain at the crack, $u_x(b, t)$. Using (2.14), this transition condition becomes

$$u_x(b, t) = \sum_{k=1}^{N} u_k(t)[\theta_k \cos(\theta_k b)] \begin{cases} \geq 0 \text{ for an open crack} \\ < 0 \text{ for a closed crack} \end{cases} \tag{2.19}$$

For N terms, after multiplying through by the constant $\frac{2L}{\pi}$ (> 0) as well as dividing through by the factor relating $u_n(t)$ and $\tilde{u}_n(\tau)$, and substituting for the nondimensional quantity $\tilde{b} = \frac{b}{L}$, the transition formula in nondimensional form becomes

$$\sum_{k=1}^{N} \tilde{u}_k(\tau)[(2k-1)\cos \gamma_k \tilde{b}] \begin{cases} \geq 0 \text{ for an open crack} \\ < 0 \text{ for a closed crack} \end{cases} \tag{2.20}$$

2.3 Solution

The solution of the nondimensional ordinary differential equations depends on the number of terms used to approximate $\tilde{u}(x, \tau)$. For $N = 1$, the general ordinary differential equation can be written in the form

$$\frac{d^2\tilde{u}_n}{d\tau^2} + B_n \frac{d\tilde{u}_n}{d\tau} + A_n \tilde{u}_n = \frac{1}{(2n-1)} \cos \tilde{\Omega}\tau \tag{2.21}$$

for which a closed-form solution is available in each region where A_n and B_n are constant. For $N > 1$, the resulting equations become coupled and numerical integration is a more practical sol-

ution technique. The exact form of the equations for N = 1 and N = 2, as well as their solutions, will be presented later.

The computer program used to arrive at solutions (whether exact or numerical) is based on the guidelines used by Thompson in his papers on bilinear oscillators (for example, Thompson and Stewart, 1986). The highlights of the program are as follows:

- The program looks for the change in sign of the transition condition and converges to the transition time within a tolerance of 1.0×10^{-8} as used by Bapat and Sankar (1986).

- The program searches for the steady-state condition by using the concept of Poincaré mapping. This technique involves comparing the value of the displacement function at some time τ to its value at a time $\tau + (2j\pi/\tilde{\Omega})$ where j is the order of the desired harmonic. For simple harmonic motion, j = 1. If these values agree (within a given tolerance for computer applications), then steady state has been achieved.

- After detecting the steady-state conditions, the program searches for the maximum displacement of the free end of the bar by finding points in time at which the velocity is equal to zero (within a tolerance of 1.0×10^{-3}). The maximum displacement is then the largest of these relative maxima.

When the exact solution is available and feasible to use (N = 1 case), the program uses the closed-form solution for an underdamped system, which is the case for the parameters used in this thesis. When numerical integration is required, the IMSL (International Mathematics and Statistical Libraries) subroutine DIVPAG is utilized. The DIVPAG subroutine offers two numerical integration options: integration by Adams-Moulton Method or by Gear's Stiff Method. In this thesis, the Adams-Moulton Method is used. Since DIVPAG only integrates first-order equations, appropriate transformations are used to convert the second-order ordinary differential equations into first-order ordinary differential equations.

2.4 Forced Vibration: One-Term Approximation

As stated earlier, the one-term approximation can be written in the form

$$\frac{d^2\tilde{u}_n}{d\tau^2} + B_n \frac{d\tilde{u}_n}{d\tau} + A_n \tilde{u}_n = \frac{1}{(2n-1)} \cos \tilde{\Omega}\tau \tag{2.21}$$

where the natural frequency squared, A_n, is

$$A_n = (2n-1)^2 - \Lambda \tilde{c}_{11} (2n-1)^2 (\cos \gamma_n \tilde{b})^2 \tag{2.22a}$$

and the damping coefficient, B_n , is

$$B_n = (1-\Lambda)(\sin \gamma_n \tilde{b})^2 \tilde{d}_c + \tilde{d}_e + (2n-1)^2 \tilde{d}_i - \Lambda \tilde{c}_{11} \tilde{d}_i (2n-1)^2 (\cos \gamma_n \tilde{b})^2 \tag{2.22b}$$

and

$$\Lambda = \begin{cases} 1 \text{ if } \tilde{u}_n(\tau) \cos \gamma_n \tilde{b} \geq 0 \\ 0 \text{ if } \tilde{u}_n(\tau) \cos \gamma_n \tilde{b} < 0 \end{cases} \tag{2.22c}$$

This equation describes a one-degree-of-freedom system with bilinear stiffness and damping. For n = 1, such a system possesses damping and stiffness characteristics as shown in Figure 2.2.

For the one-term approximation (which can involve any n), the closed-form solution is well-known; in term of the parameters of (2.21), it is

$$\tilde{u}_n(\tau) = \hat{C} e^{(-B_n \tau/2)} \cos\left(\frac{\tau}{2}\sqrt{4A_n - B_n^2} - \Psi\right) + \frac{\cos(\tilde{\Omega}\tau - \Theta)}{(2n-1)\sqrt{\tilde{\Omega}^2 B_n^2 + (A_n - \tilde{\Omega}^2)^2}} \tag{2.23a}$$

where

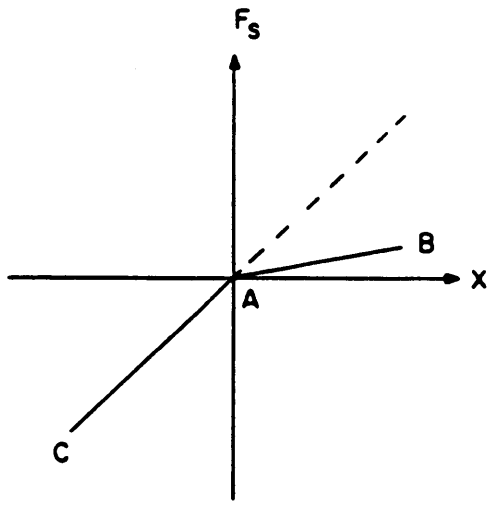

(a)

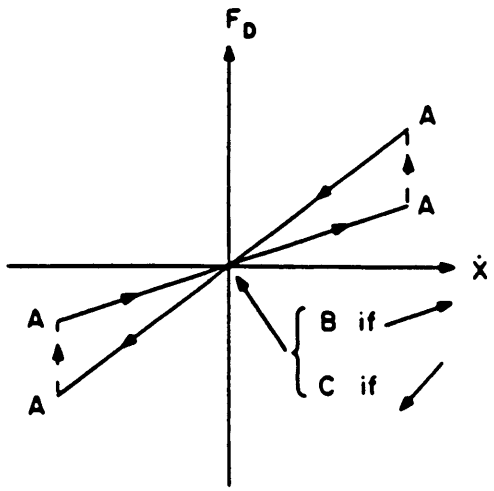

(b)

Figure 2.2. **Characteristics:** Stiffness (a) and damping (b) characteristics of the one-term approximation (n = 1). The diagrams only apply for simple harmonic motion. Note that the damping characteristic does not change at the origin, but when the velocity is a maximum or minimum.

$$\Theta = \tan^{-1}\left(\frac{\tilde{\Omega} B_n}{A_n - \tilde{\Omega}^2}\right) \tag{2.23b}$$

and $\hat{C}$ and Ψ are constants which depend on initial conditions. However, since the system is non-linear (piecewise linear), the exact solutions in each region must be matched at the transition points.

In any computerized procedure such as the one used in this thesis, it is important to understand how numerical errors may accumulate as a result of discretization. To this end, Tables 2.1, 2.2, and 2.3 provide the results of some small-scale numerical accuracy tests related to the program discussed earlier. The goals of the tests are to study how error may accumulate over time, how the tolerances can affect the results, and how the results based on the numerical integration technique differ from the results based on the exact solution.

Tables 2.1 and 2.2 provide time history data for the longitudinal vibration of a bar using various values for the transition tolerance. Table 2.1 focuses on how the transition condition can introduce numerical errors over a long period of time for a shaft which does not have a crack. Mathematically, the no-crack condition is obtained by setting $\tilde{c}_{11} = 0$ and $\tilde{b} = 0$, which implies that A_n and B_n are constant for all time. Therefore, an exact solution is available for all time. The values in the table compare the "exact" value of the end displacement of the bar (obtained from a separate linear analysis) and the value obtained using the program with the parameters as stated above. The end displacement of the bar is given by

$$\tilde{u}(L, \tau) = \tilde{u}_n(\tau) \sin \gamma_n = (-1)^{n+1} \tilde{u}_n(\tau) \tag{2.24}$$

The program uses the exact solution in each region, and matches the solutions at the transition points. Percentage differences between the two values are provided. The table reveals that the switching procedure introduces a small amount of numerical error which accumulates over time. This error is reduced as the transition tolerance is made more stringent.

Table 2.1. The effect of the transition tolerance on the results (uncracked bar)

TIME	EXACT	1.0×10^{-3}		1.0×10^{-4}		1.0×10^{-5}		1.0×10^{-6}	
τ	$\tilde{u}(L, \tau)$	$\tilde{u}(L, \tau)$	% error	$\tilde{u}(L, \tau)$	% error	$\tilde{u}(L, \tau)$	% error	$\tilde{u}(L, \tau)$	% error
1.57080	0.705426	0.705426	0	0.705426	0	0.705426	0	0.705426	0
4.71239	-1.86401	-1.86381	0.011	-1.86401	0	-1.86401	0	-1.86401	0
32.9867	4.81694	4.81775	0.017	4.81694	0	4.81694	0	4.81694	0
64.4027	4.99239	4.99384	0.029	4.99240	≃0	4.99239	0	4.99239	0
127.235	4.99999	5.00197	0.040	5.00000	≃0	4.99999	0	4.99999	0
314.014	-0.626511	-0.615345	1.78	-0.626508	≃0	-0.626505	≃0	-0.626505	≃0

NOTES:
(a) $n = 1$, $\tilde{b} = \tilde{c}_{11} = 0$, $\tilde{\Omega} = 1$, $\tilde{d}_1 = 0.01$, $\tilde{d}_2 = \tilde{d}_3 = 0.1$
(b) initial displacement = initial velocity = 0

Table 2.2. The effect of the transition tolerance on the results (cracked bar)

TIME	1.0×10^{-2}	1.0×10^{-4}	1.0×10^{-6}	1.0×10^{-8}	DIVPAG (1.0×10^{-6})
τ	$\tilde{u}(L, \tau)$	$\tilde{u}(L, \tau)$	$\tilde{u}(L, \tau)$	$\tilde{u}(L, \tau)$	$\tilde{u}(L, \tau)$
1.57080	0.715998	0.715998	0.715998	0.715998	0.715998
4.71239	-1.84731	-1.84762	-1.84761	-1.84761	-1.84761
32.9867	4.84145	4.84435	4.84434	4.84434	4.84434
64.4027	4.98498	4.98304	4.98299	4.98299	4.98299
127.235	4.99079	4.98535	4.98534	4.98534	4.98534
314.034	-1.13106	-1.13853	-1.13853	-1.13853	-1.13853

NOTES:
(a) $n = 1$, $\tilde{b} = 0.5$, $\tilde{c}_{11} = 0.10$, $\tilde{d}_v = 0.01$, $\tilde{d}_s = \tilde{d}_t = 0.1$, $\tilde{\Omega} = 1$
(b) initial displacement = initial velocity = 0

Table 2.2 also considers the impact of the transition tolerance, but applies to a cracked bar. For this case, no continuous solution for all time is available. Nevertheless, the effect of the transition tolerance can be observed. Again, the exact solution in each region is used and the solutions are matched at the transition points. As with Table 2.1, Table 2.2 shows that numerical error does enter into the results when the tolerance is lax. Also, in Table 2.2, the last column includes the time history data obtained from numerical integration for the same cracked bar. By comparing the results from the analysis using the closed-form solution to the results from the numerical integration, one notices that the results are identical for the number of digits shown in the table. Upon observation of the untruncated numbers, one notes that the agreement ends at the fourth or fifth decimal place, which is within the range of accuracy of the double-precision routine used here. This agreement is somewhat surprising since numerical integration is an approximate procedure, but the strict error control tolerance of 1.0×10^{-9} (NOT the transition tolerance) chosen within the DIVPAG procedure seems to be effective in providing accurate results.

Table 2.3 provides the results of the investigation into how the tolerance on the Poincaré points affects the determination of steady state. A no-crack condition is again assumed. The transition tolerance was set at 1.0×10^{-8}. The tolerance for the Poincaré points is not an absolute tolerance but instead is a percentage tolerance. The table provides information on the maximum value of the steady-state end displacement, $\tilde{u}_{max}$, and the corresponding time τ_{max}. The table clearly shows the problem of determining a single tolerance which works for all cases. If the chosen tolerance is too strict, the program will not detect a steady-state condition due to numerical errors in the storage of digits and in the discretization. On the other hand, if the chosen tolerance is too lax, the program will prematurely determine that the steady state has been reached. Due to this difficulty, it is important to note that the results to follow are not based on a single value of the Poincaré tolerance. Tolerances have been adjusted slightly as necessary to obtain the results. Time history plots have been used to verify the choices of tolerances.

The "standard case" used in the longitudinal vibration study consists of the following values:

Table 2.3. The effect of the Poincaré point tolerance

FORCING FREQUENCY $\bar{\Omega}$	MEASURED QUANTITIES	TOLERANCES (%)			
		0.1	0.001	0.0001	0.00001
1.0	$\bar{u}_{max}$	5.000000	•••	•••	•••
	τ_{max}	193.208			
3.0	$\bar{u}_{max}$	0.140042	0.125778	0.124660	•••
	τ_{max}	14.6566	41.8624	92.1283	
5.0	$\bar{u}_{max}$	0.0562671	0.0424100	•••	•••
	τ_{max}	8.79546	38.3181		

NOTES:
(a) ••• = Program did not detect a steady-state condition
(b) $n = 1$, $\bar{b} = \bar{c}_{11} = 0$, $\bar{d}_e = 0.01$, $\bar{d}_v = \bar{d}_s = 0.1$, transition tolerance = 1×10^{-6}

$\tilde{b} = 0.5$

$\tilde{c}_{11} = 0.1$

$\tilde{\Omega} = 1.0$

$\tilde{d}_c = 0.01$

$\tilde{d}_e = 0.1$

$\tilde{d}_i = 0.1$

$$\tilde{u}_n|_{\tau=0} = \frac{d\tilde{u}_n}{d\tau}|_{\tau=0} = 0$$

The choice of $\tilde{c}_{11} = 0.1$, for a circular bar, corresponds to a length/radius (L/R) ratio of about 3.3 for a crack depth/diameter ratio (denoted as a/D in Papadopoulos and Dimarogonas, 1988) of 0.2, or an L/R ratio of 11 for an a/D ratio of 0.3. The chosen values for $\tilde{d}_c$, $\tilde{d}_e$, and $\tilde{d}_i$ are not based on any experimental data but are simply "educated guesses" at the order of magnitude of such parameters.

In Figure 2.3, a time history plot for the n = 1 mode under standard conditions is presented. The nondimensional end displacement, given by equation (2.24), is plotted on the ordinate axis. The abscissa represents the nondimensional time τ. (For all of the subsequent graphs, unless otherwise noted, all plotted quantities are nondimensional.). It is seen that a steady state is reached quickly.

An important goal of this thesis is to investigate how the crack affects the steady-state amplitude of motion (based on the mathematical model). Figures 2.4 through 2.10 provide this information by showing how the maximum steady-state end displacement, $\tilde{u}_{max}$, varies with respect to the forcing frequency $\tilde{\Omega}$, the compliance $\tilde{c}_{11}$, and the crack location $\tilde{b}$. Each figure contains three graphs cor-

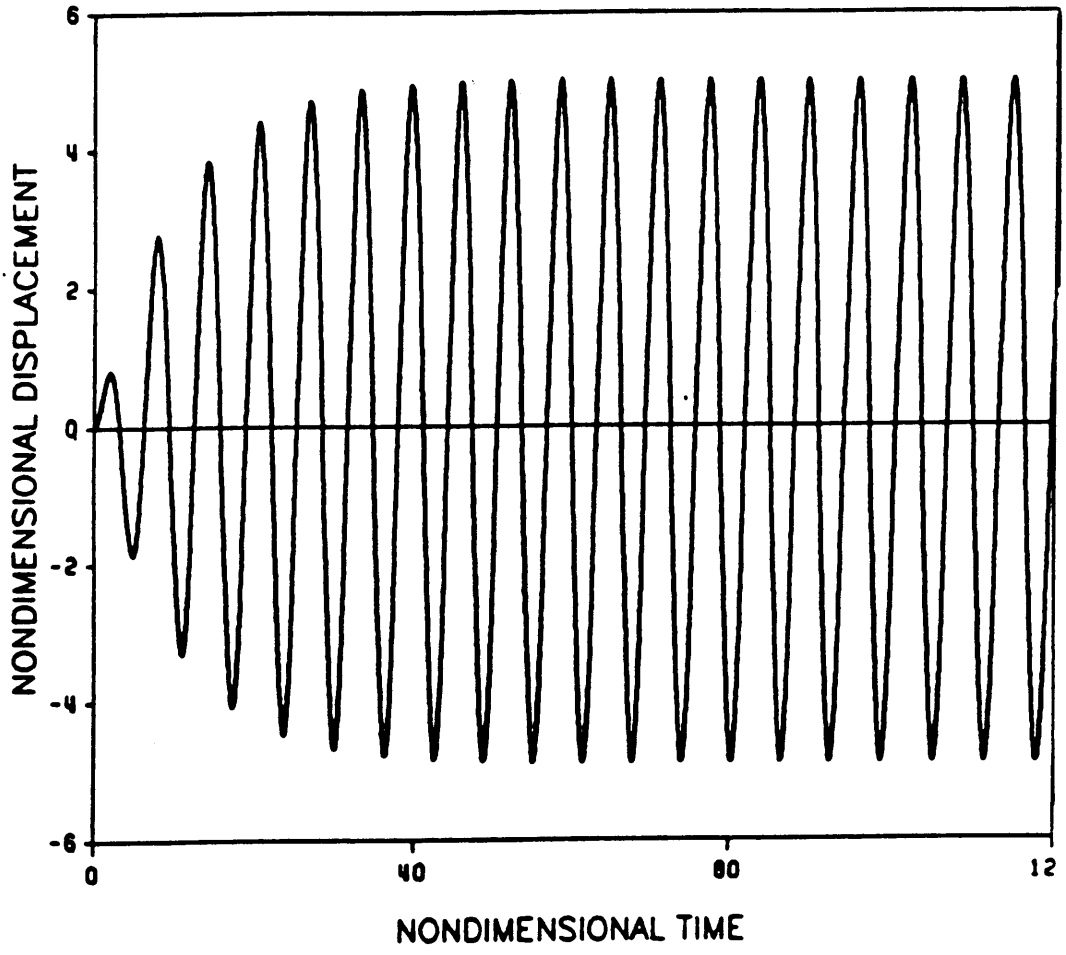

Figure 2.3. Standard case behavior: Time history for n = 1 mode under standard conditions.

responding to a mode number n = 1, 2, or 3. Within each graph, three curves are shown. The BREATHING curves represent the value of $\tilde{u}_{max}$ obtained by using the computer program discussed earlier. The OPEN curves represent the value of $\tilde{u}_{max}$ obtained by assuming that the crack remains open at all times. Likewise, the CLOSED curves represent the value of $\tilde{u}_{max}$ obtained by assuming a closed crack for all time. Since there is no transition condition for the OPEN and CLOSED systems, these cases are linear and the value of $\tilde{u}_{max}$ is obtained by using the amplitude of the particular solution in equation (2.23), namely

$$\tilde{u}_{max} = \frac{1}{(2n-1)\sqrt{\tilde{\Omega}^2 B_n^2 + (A_n - \tilde{\Omega}^2)^2}} \tag{2.25}$$

Within all of the graphs, the appropriate mode (n value) and forcing frequency $\tilde{\Omega}$ (if applicable) are shown. Unless otherwise stated, all nonvaried parameters have their standard case values.

Figure 2.4 reflects the effect of the forcing frequency on the steady-state amplitude. In all three cases, the BREATHING curve falls between the OPEN and CLOSED curves. As expected, each mode exhibits its maximum amplitude when the forcing frequency is near the natural frequency of the uncracked bar, which is equal to $(2n-1)$ for the n^{th} mode. It is important to note the difference in the scales for the ordinate axis for each mode. Clearly, the n = 1 mode exhibits the largest displacements since this mode has the lowest stiffness and damping coefficients, as can be deduced from equations (2.22).

Figures 2.5 through 2.7 show how the value of the compliance, $\tilde{c}_{11}$, affects the steady-state response. The CLOSED curve does not vary with $\tilde{c}_{11}$ because for this case $\Lambda = 0$, so that all $\tilde{c}_{11}$ terms vanish. In Figure 2.5(c), the OPEN curve and the BREATHING curve overlap. The OPEN solution may rise or fall with increasing $\tilde{c}_{11}$, depending on the particular mode and the forcing frequency. This behavior results from the trade-off in the denominator of equation (2.25) between the A_n and $\tilde{\Omega}^2$ terms. For the cases shown, as $\tilde{c}_{11}$ increases (implying a larger crack), the value of $\tilde{u}_{max}$ increases for the BREATHING crack solution.

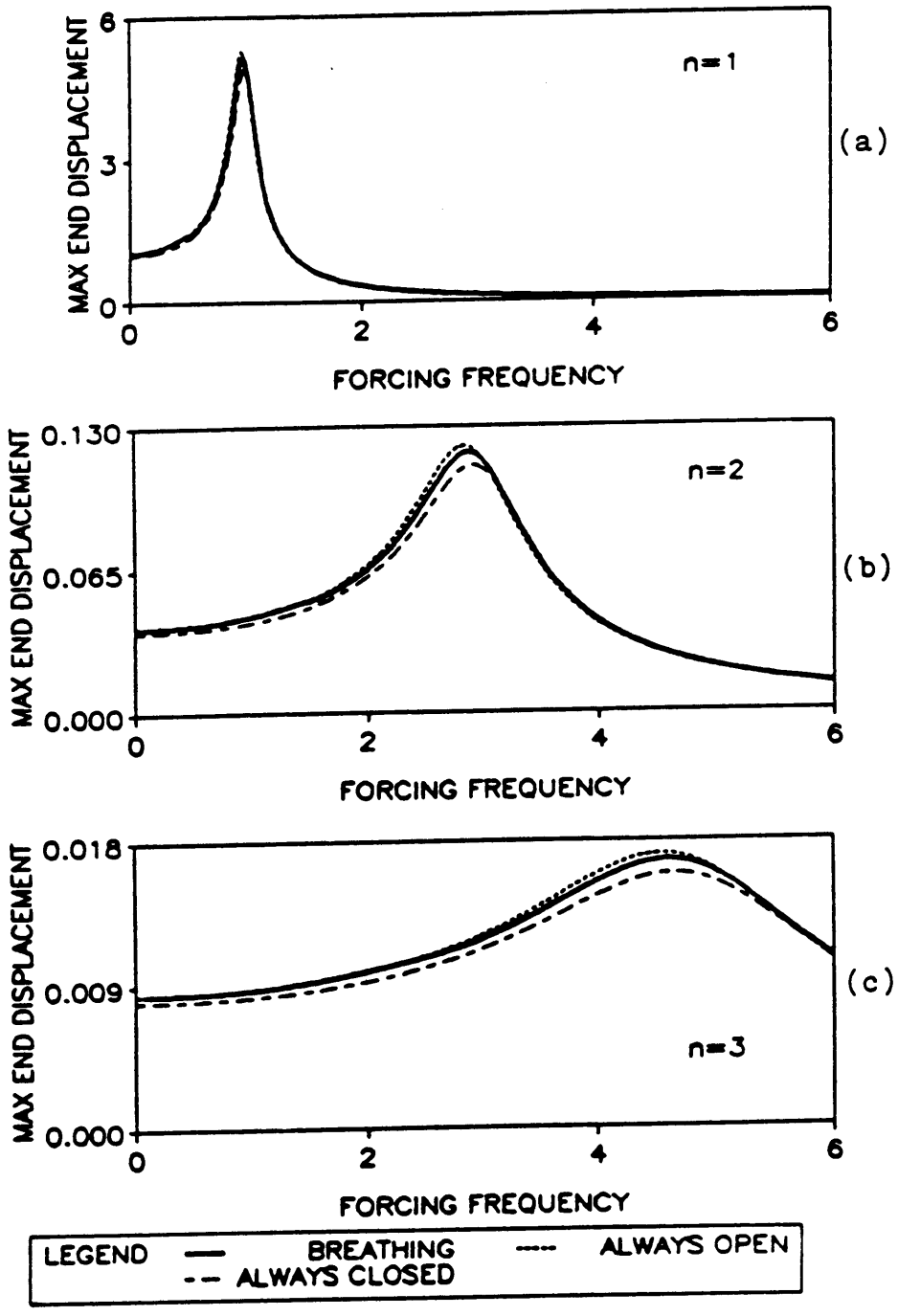

Figure 2.4. **Maximum end displacement vs. forcing frequency $\tilde{\Omega}$:** Graphs illustrate how the forcing frequency affects the maximum steady-state response. (a) n = 1; (b) n = 2; (c) n = 3.

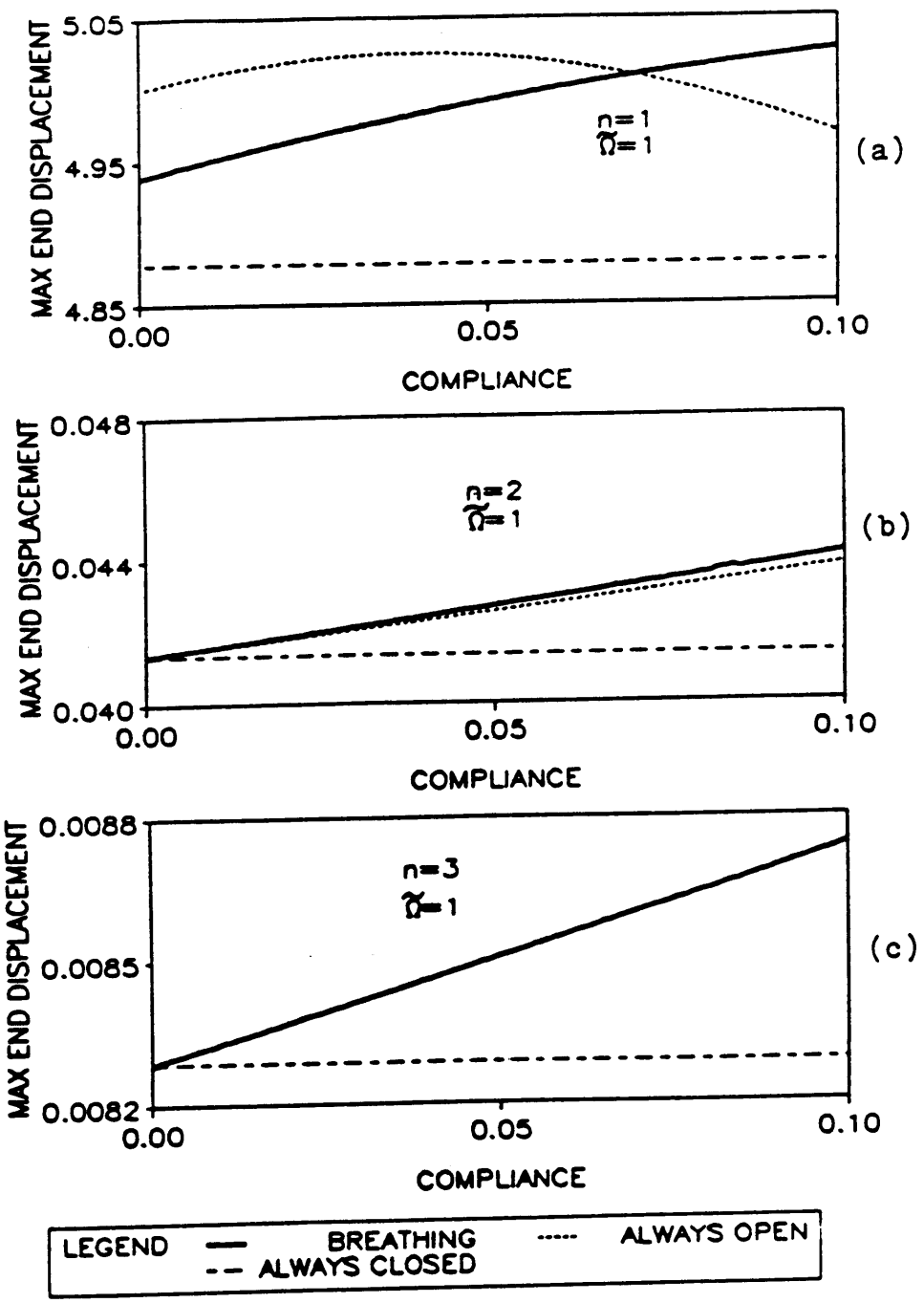

Figure 2.5. Maximum end displacement vs. $\tilde{c}_{11}$ ($\tilde{\Omega} = 1$): Graphs illustrate how the compliance affects the maximum steady-state response. (a) n = 1; (b) n = 2; (c) n = 3.

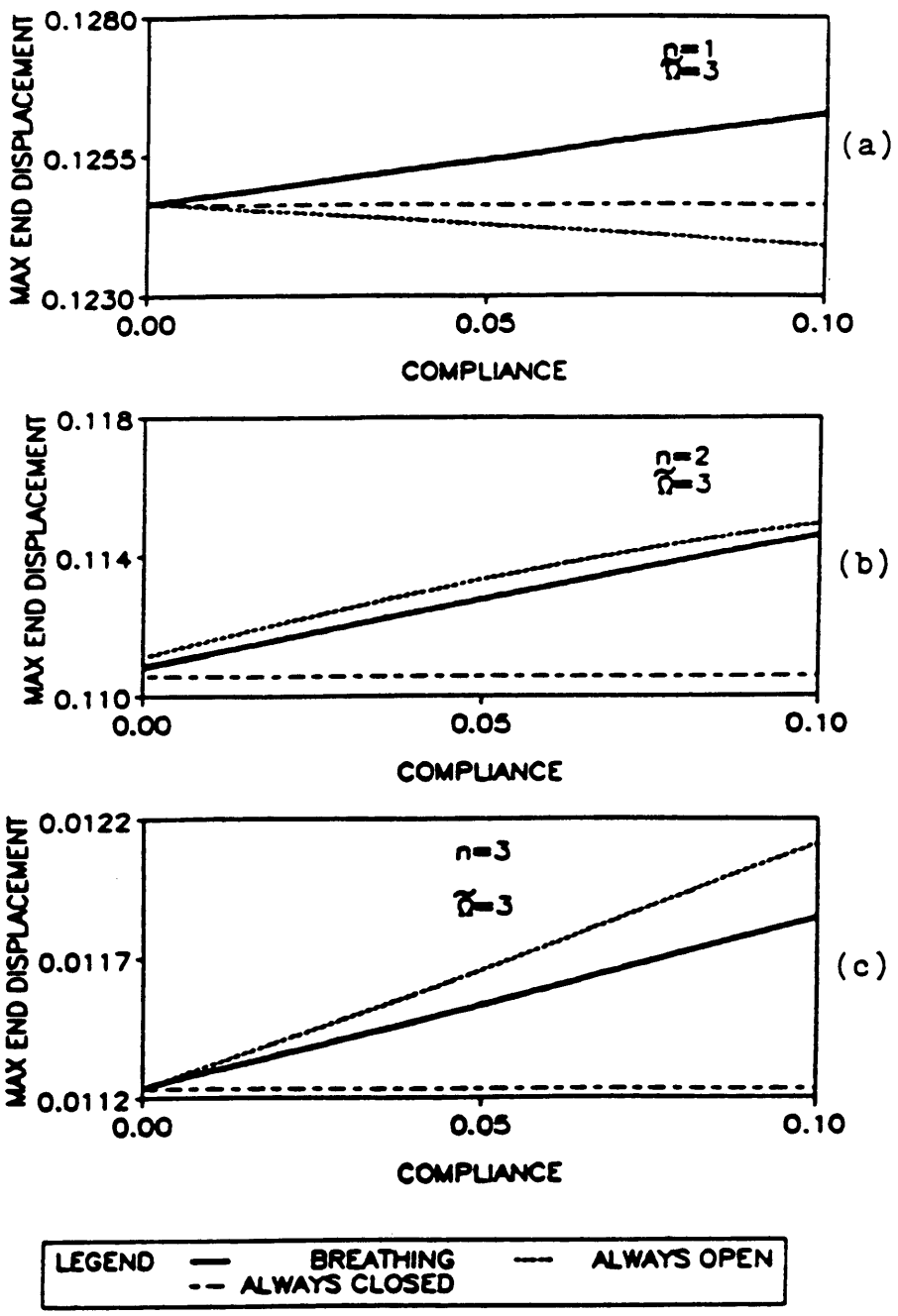

Figure 2.6. Maximum end displacement vs. $\tilde{c}_{11}$ ($\tilde{\Omega} = 3$): Graphs illustrate how the compliance affects the maximum steady-state response. (a) n = 1; (b) n = 2; (c) n = 3.

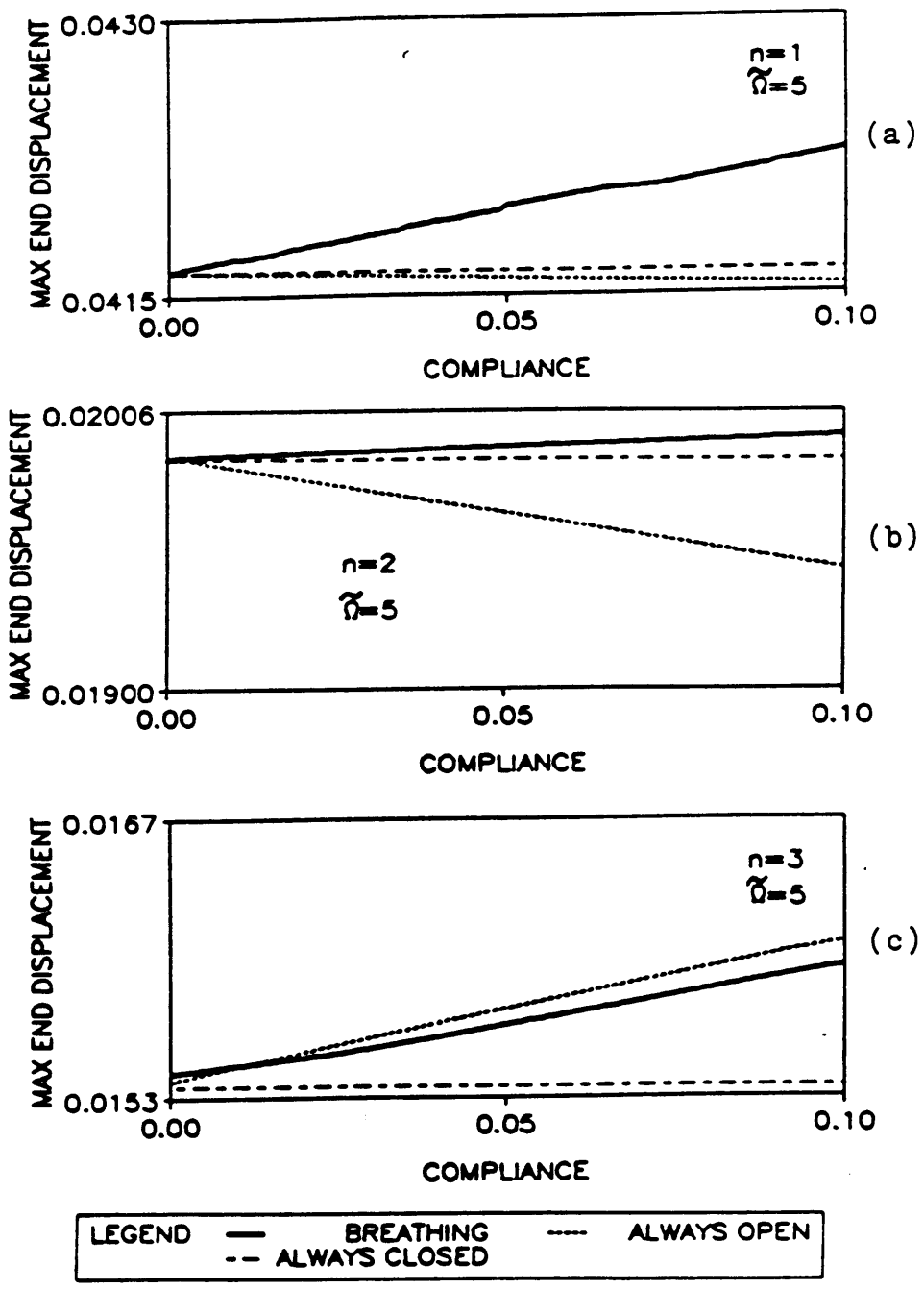

Figure 2.7. **Maximum end displacement vs. $\tilde{c}_{11}$ ($\tilde{\Omega}=5$):** Graphs illustrate how the compliance affects the maximum steady-state response. (a) n = 1; (b) n = 2; (c) n = 3.

Finally, Figures 2.8 through 2.10 illustrate how $\tilde{u}_{max}$ varies with the crack location $\tilde{b}$. In Figure 2.8(c), the OPEN and BREATHING curves are indistinguishable, as they were in Figure 2.5(c). The CLOSED curves, which in some cases appear to be perfectly horizontal, in fact are not constant horizontal lines. The CLOSED response does indeed vary with $\tilde{b}$ as can be seen from (2.22b) and (2.23). However, this variation is very small with respect to the (2n-1) terms for those combinations of n and $\tilde{\Omega}$ away from resonance. Near resonance, $(A - \tilde{\Omega}^2)^2$ becomes small and the effect of $\tilde{b}$ is more evident in the $\tilde{\Omega}^2 B_n^2$ term of the denominator of equation (2.25). When the crack is located at a node point of a particular mode, no significant effect is evident in the curves. However, when the crack is located such that the transition condition is identically zero for all time, all three curves approach the same value (in Figure 2.8(a), the choice of ordinate scaling distorts the displacements at $\tilde{c}_{11} = 0.1$ so that the curves don't appear to be close to each other).

The logic behind including the OPEN and CLOSED curves is to observe if the nonlinear, breathing crack behavior can be adequately approximated by the linear behavior of the OPEN or CLOSED cases. As the graphs indicate, only in some cases does the OPEN solution provide a reasonably close approximation. Therefore, the previous investigations of other researchers who consider only open cracks (for example, Gudmundson, 1983) may not always accurately reflect the vibrational behavior of the bar.

2.5 Forced Vibration: Two-Term Approximation

The two-term approximation results in two ordinary differential equations of motion. For any two modes, say n and m, the resulting equations, from equation 2.17, are of the form

$$\frac{d^2\tilde{u}_n}{d\tau^2} + B_{nn}\frac{d\tilde{u}_n}{d\tau} + B_{nm}\frac{d\tilde{u}_m}{d\tau} + A_{nn}\tilde{u}_n + A_{nm}\tilde{u}_m = \frac{1}{(2n-1)}\cos\tilde{\Omega}\tau \qquad (2.26)$$

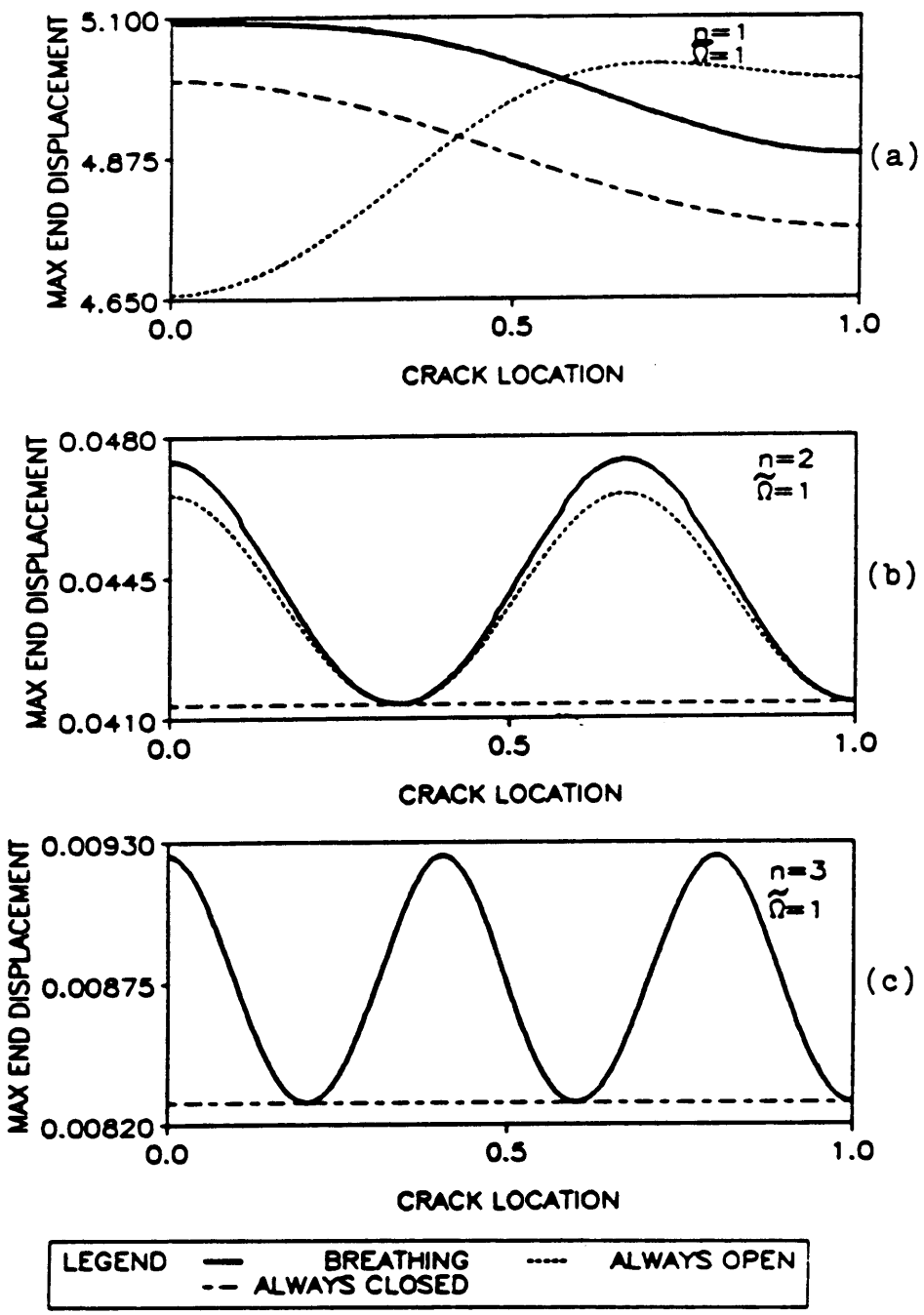

Figure 2.8. Maximum end displacement vs. $\tilde{b}$ ($\tilde{\Omega}=1$): Graphs illustrate how the crack location affects the maximum steady-state response. (a) n = 1; (b) n = 2; (c) n = 3.

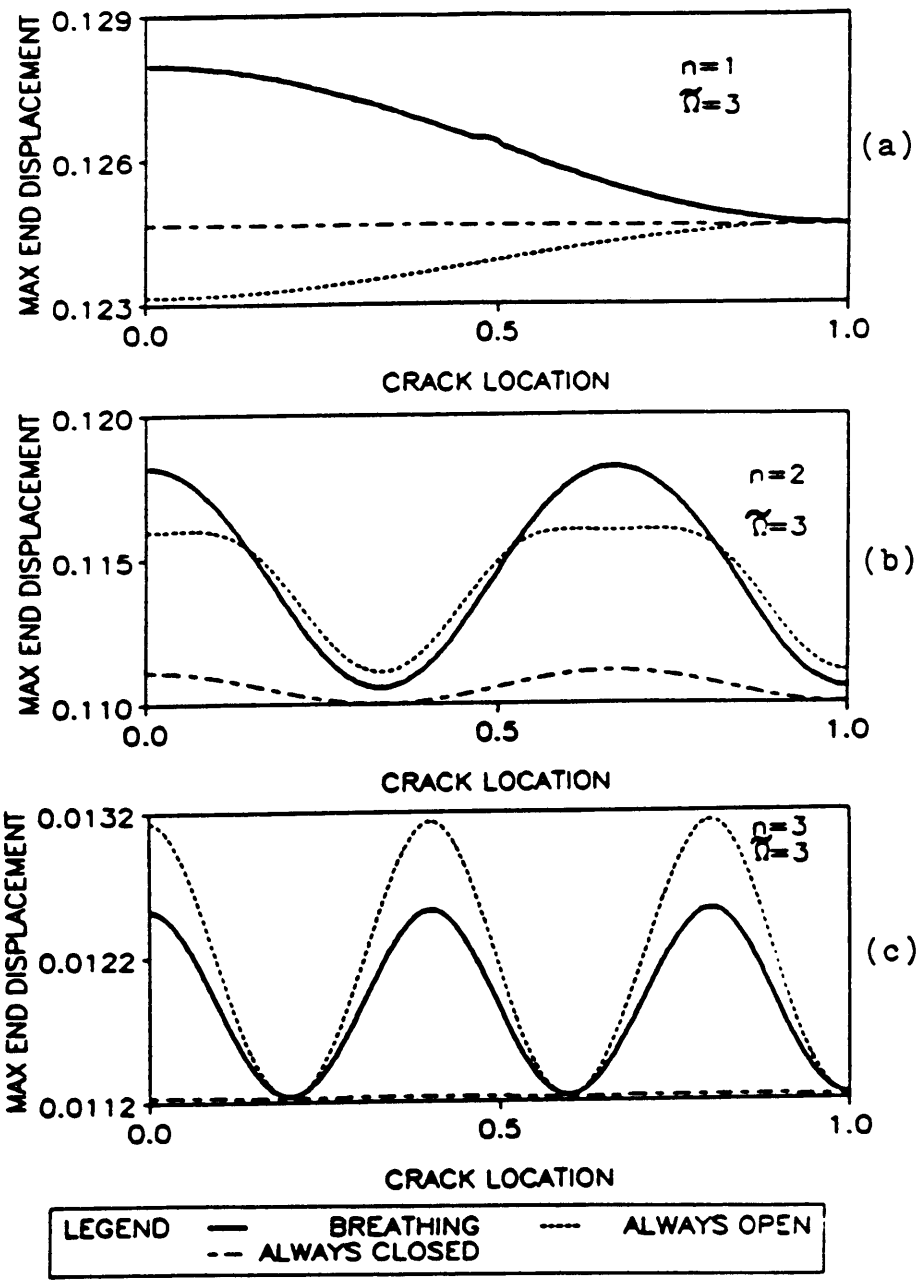

Figure 2.9. Maximum end displacement vs. $\tilde{b}$ ($\tilde{\Omega}=3$): Graphs illustrate how the crack location affects the maximum steady-state response. (a) $n=1$; (b) $n=2$; (c) $n=3$.

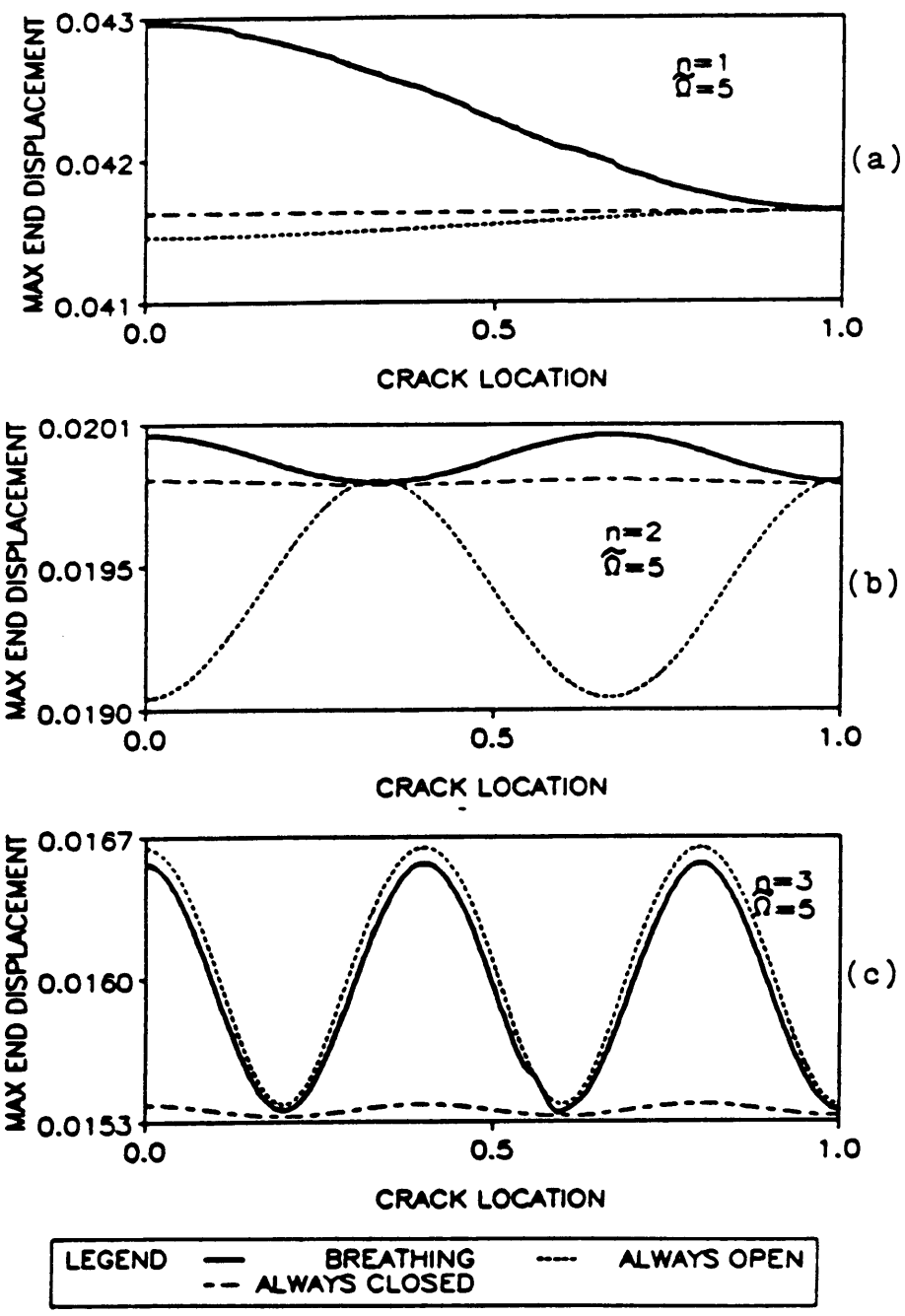

Figure 2.10. Maximum end displacement vs. $\tilde{b}$ ($\tilde{\Omega}=5$): Graphs illustrate how the crack location affects the maximum steady-state response. (a) n = 1; (b) n = 2; (c) n = 3.

$$\frac{d^2\tilde{u}_m}{d\tau^2} + B_{mn}\frac{d\tilde{u}_n}{d\tau} + B_{mm}\frac{d\tilde{u}_m}{d\tau} + A_{mn}\tilde{u}_n + A_{mm}\tilde{u}_m = \frac{1}{(2m-1)}\cos\tilde{\Omega}\tau \tag{2.27}$$

where

$$A_{nn} = (2n-1)^2 - \Lambda\tilde{c}_{11}(2n-1)^2(\cos\gamma_n\tilde{b})^2 \tag{2.28a}$$

$$A_{mm} = (2m-1)^2 - \Lambda\tilde{c}_{11}(2m-1)^2(\cos\gamma_m\tilde{b})^2 \tag{2.28b}$$

$$A_{nm} = A_{mn} = -\Lambda\tilde{c}_{11}(2m-1)(2n-1)(\cos\gamma_m\tilde{b})(\cos\gamma_n\tilde{b}) \tag{2.28c}$$

$$B_{nn} = \tilde{d}_e + (2n-1)^2\tilde{d}_i - \Lambda(2n-1)^2\tilde{d}_i\tilde{c}_{11}(\cos\gamma_n\tilde{b})^2 + (1-\Lambda)\tilde{d}_c(\sin\gamma_n\tilde{b})^2 \tag{2.28d}$$

$$B_{mm} = \tilde{d}_e + (2m-1)^2\tilde{d}_i - \Lambda(2m-1)^2\tilde{d}_i\tilde{c}_{11}(\cos\gamma_m\tilde{b})^2 + (1-\Lambda)\tilde{d}_c(\sin\gamma_m\tilde{b})^2 \tag{2.28e}$$

$$\begin{aligned} B_{nm} = B_{mn} &= (1-\Lambda)\tilde{d}_c(\sin\gamma_m\tilde{b})(\sin\gamma_n\tilde{b}) \\ &- \Lambda\tilde{c}_{11}\tilde{d}_i(2m-1)(2n-1)(\cos\gamma_m\tilde{b})(\cos\gamma_n\tilde{b}) \end{aligned} \tag{2.28f}$$

and

$$\Lambda = \begin{cases} 1 \text{ if } \tilde{u}_n(\tau)(2n-1)\cos\gamma_n\tilde{b} + \tilde{u}_m(\tau)(2m-1)\cos\gamma_m\tilde{b} \geq 0 \\ 0 \text{ if } \tilde{u}_n(\tau)(2n-1)\cos\gamma_n\tilde{b} + \tilde{u}_m(\tau)(2m-1)\cos\gamma_m\tilde{b} < 0 \end{cases} \tag{2.29}$$

The end displacement of the bar is given by

$$\tilde{u}(L,\tau) = (-1)^{n+1}\tilde{u}_n(\tau) + (-1)^{m+1}\tilde{u}_m(\tau) \tag{2.30}$$

Figures 2.11 and 2.12 give time histories of the two-mode case (n = 1,m = 2) using all standard conditions *except* the forcing frequency $\tilde{\Omega}$. In Figure 2.11, $\tilde{\Omega} = 0.6$ and in Figure 2.12, $\tilde{\Omega} = 2.5$. These values are chosen in order to avoid resonance in one mode which might hide any modal interaction taking place. As with the one-mode study, the initial conditions are zero, i.e.,

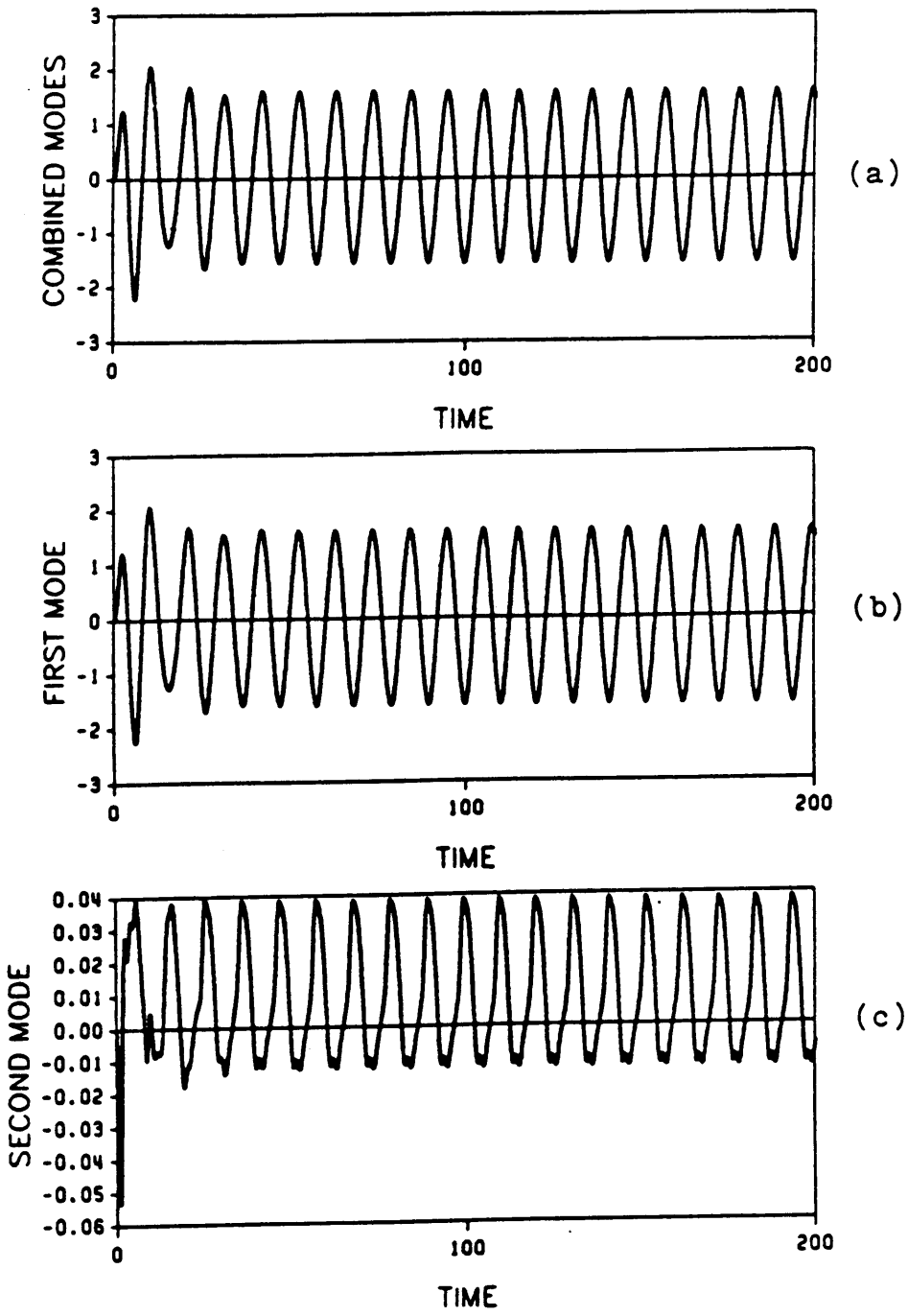

Figure 2.11. Two-mode time history ($\tilde{\Omega} = 0.6$): (a) $\tilde{u}_1 - \tilde{u}_2$; (b) $\tilde{u}_1$; (c) $-\tilde{u}_2$. Note the behavior of the second-mode component.

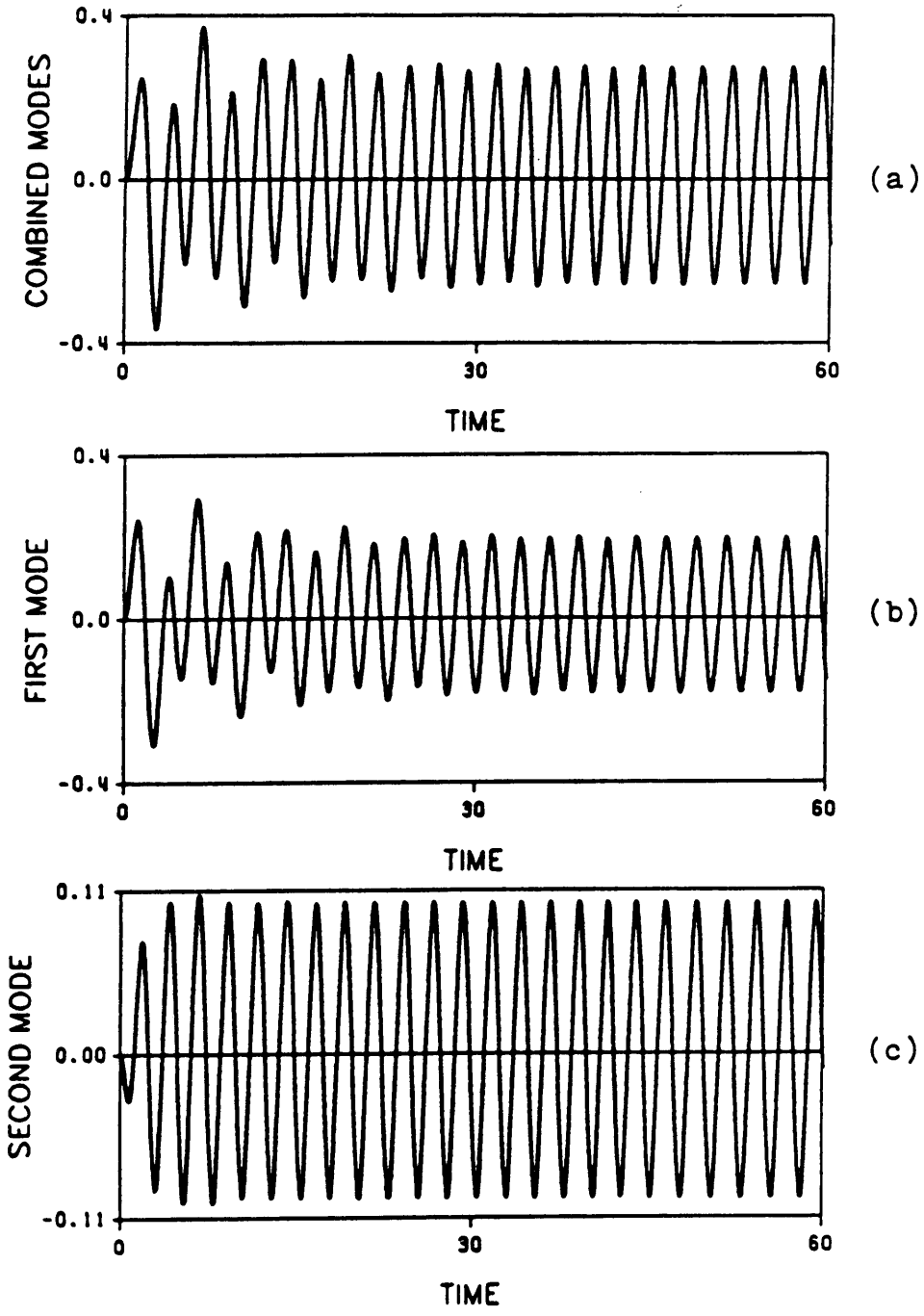

Figure 2.12. Two-mode time history ($\tilde{\Omega} = 2.5$): (a) $\tilde{u}_1 - \tilde{u}_2$; (b) $\tilde{u}_1$; (c) $-\tilde{u}_2$. Note that the second mode has a greater impact on the combined-mode behavior.

$$\tilde{u}_1|_{\tau=0} = \tilde{u}_2|_{\tau=0} = 0 \tag{2.31a}$$

$$\frac{d\tilde{u}_1}{d\tau}|_{\tau=0} = \frac{d\tilde{u}_2}{d\tau}|_{\tau=0} = 0 \tag{2.31b}$$

In the graphs, the ordinate axes labeled "combined modes" refer to the end displacement represented by equation (2.30) with n = 1 and m = 2; that is, the end displacement is given by $\tilde{u}(L, \tau) = \tilde{u}_1(\tau) - \tilde{u}_2(\tau)$. The label "first mode" refers to the $\tilde{u}_1(\tau)$ term and "second mode" refers to the $-\tilde{u}_2(\tau)$ term. The negative sign is incorporated in the "second mode" graphs in order to better visualize how the "combined modes" graph is obtained. As Figure 2.11 illustrates, the "second mode" exhibits an interesting behavior for $\tilde{\Omega} = 0.6$. To help explain this, Figure 2.13 provides the spectral analysis results for this case. A scaling factor of 500 is required to relate the spectral response peaks to an actual amplitude of $\tilde{u}_{max}$ (i.e., $\tilde{u}_{max}$ = 1/500(spectral response)). The appropriate conversion factor will be indicated in the figure caption of all spectra. The figure provides information for both a cracked bar and an uncracked bar whose longitudinal vibrational behavior is represented by the two-mode approximation. The spectrum for the uncracked bar exhibits a response at the forcing frequency $\tilde{\Omega} = 0.6$ as expected (within the numerical error of such a procedure). However, the presence of a crack excites responses at integer multiples of the forcing frequency, i.e., at $2\tilde{\Omega}$, $3\tilde{\Omega}$, etc... (A peak at $3\tilde{\Omega}$ does indeed exist but is too small to be shown on the graph.) The implication of this result is that by comparing the spectrum of a bar suspected of having a crack with its "flawless" counterpart, one can verify the presence of a crack.

As with the one-mode approximation, it is appropriate to investigate how the maximum steady-state response varies with $\tilde{b}$ and $\tilde{c}_{11}$ for the two-mode approximation. However, only one particular forcing frequency is pursued here due to the computational time and effort required to generate such graphs. Figure 2.14 illustrates how the maximum steady-state response, $\tilde{u}_{max}$, varies with $\tilde{b}$ and $\tilde{c}_{11}$ for $\tilde{\Omega} = 0.6$. All unvaried parameters have their standard case values. Again, $\tilde{u}_{max}$ increases with increasing $\tilde{c}_{11}$. However, it varies in a somewhat irregular manner with respect to $\tilde{b}$, but the general

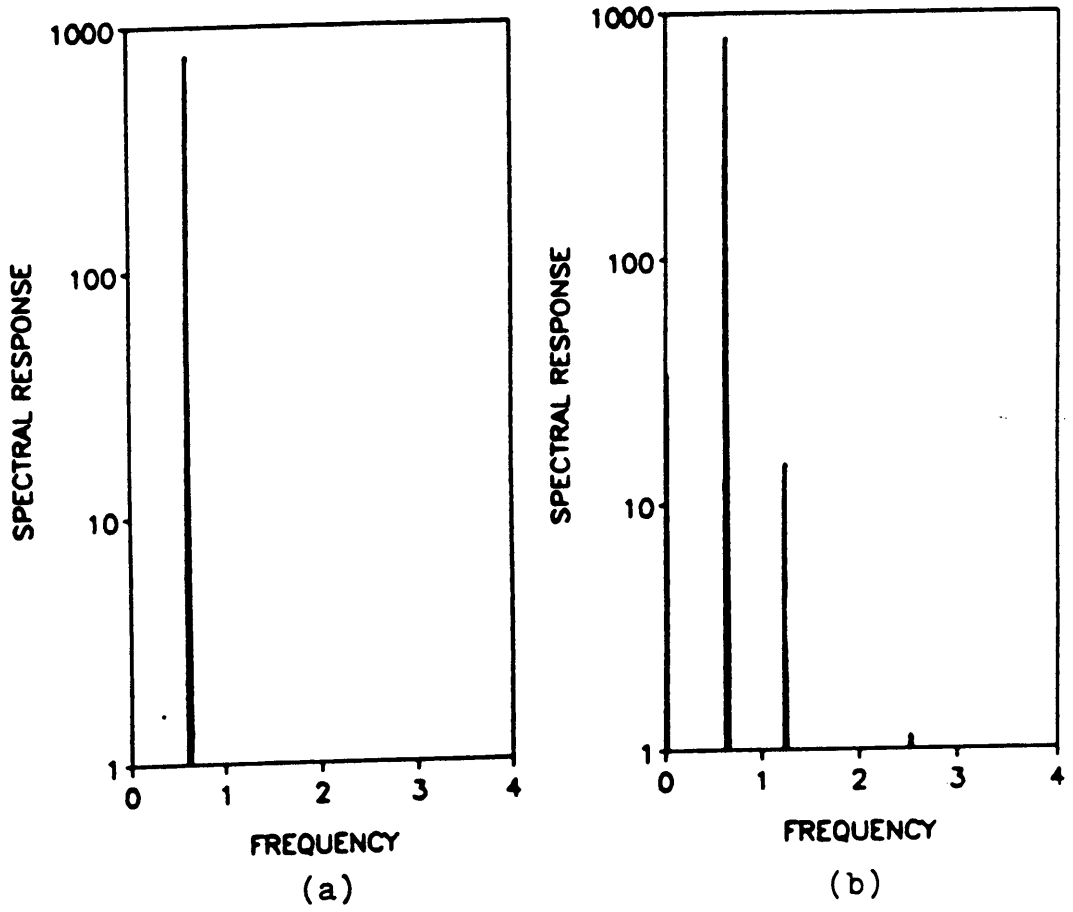

Figure 2.13. Spectra for forced vibration (two-mode approximation, $\tilde{\Omega} = 0.6$): (a) Response for an uncracked bar; (b) Response for a cracked bar. Spectral response scale factor = 1/500.

tendency is for $\tilde{u}_{max}$ to drop off with higher $\tilde{b}$. No direct comparison between these results and those of the one-mode approximation is possible since the $\tilde{\Omega}$ values are different.

The previous graphs do not provide insight into how coupling influences the two-mode results. However, Table 2.4 provides data which enables one to see the effect of the coupling on the magnitude of the end displacements for each individual mode. For the two-mode case, the total end displacement is the sum of the end displacements of the individual modes. In the table, the end displacements of these component modes are shown, as well as the end displacements of each individual mode taken as a one-mode case alone. The one-mode results were obtained by numerical integration to avoid introducing any discrepancy between exact solutions and numerical solutions. Several different combinations of $\tilde{c}_{11}$ and $\tilde{b}$ are included, and all values corresponding to a given $\tilde{\Omega}$ (= 1 or 3 in the table) are obtained at the same time in its history. As the table shows, the individual modes in both the one-mode and two-mode cases are almost equal in magnitude, which implies that the coupling effect is small. Consequently, one may conclude that it is a good approximation of the two-mode result at a given time to simply superpose the corresponding one-mode results.

2.6 Free Vibrations Without Damping

Before concluding the longitudinal vibration study, it seems appropriate to investigate the vibratory motion of the system when it is free of external excitation and damping. The following paragraphs discuss this case for both one- and two-term approximations.

When the one-term approximation is modified for an unforced, undamped system, the governing ordinary differential equation reduces to

$$\frac{d^2\tilde{u}_n}{d\tau^2} + A_n\tilde{u}_n = 0 \tag{2.32}$$

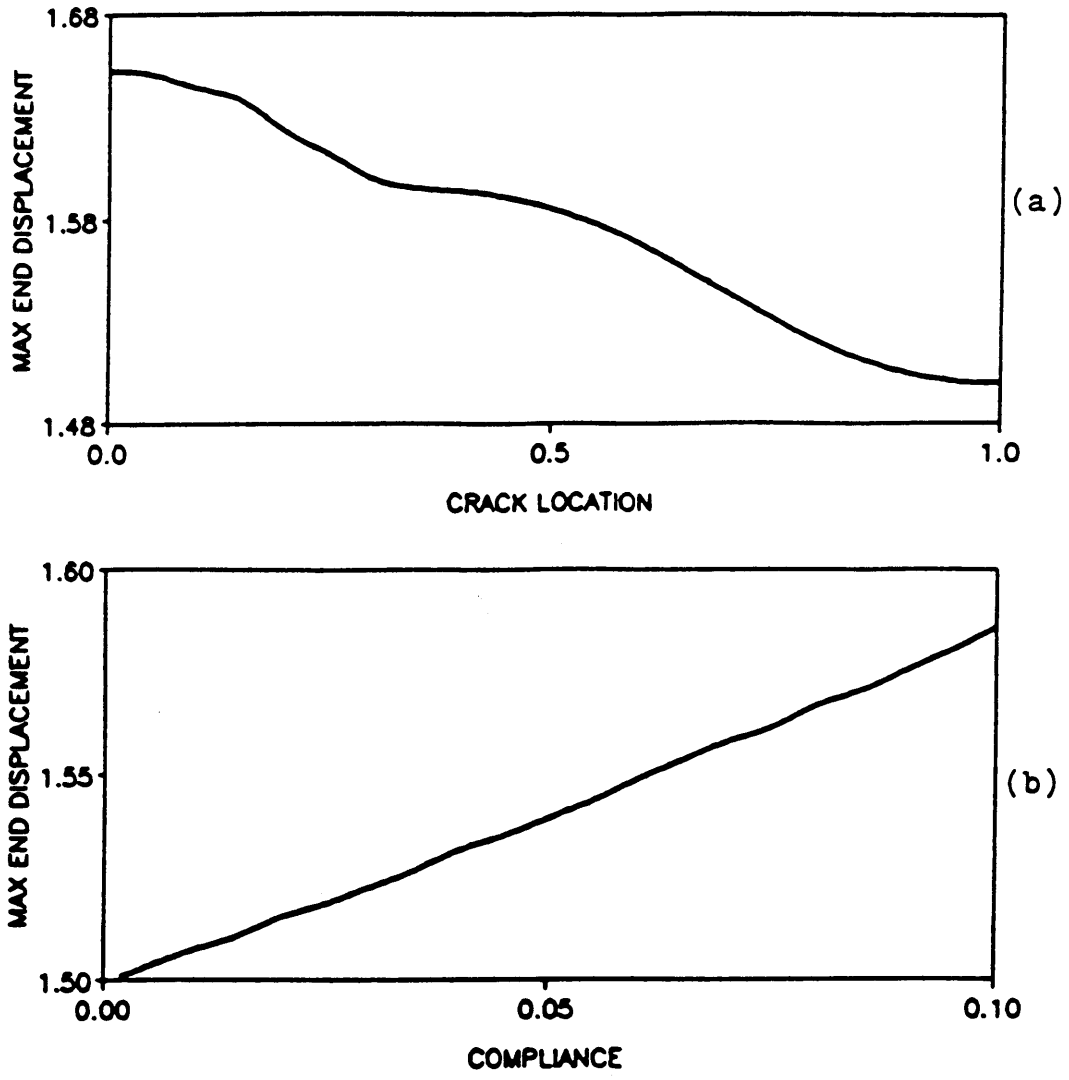

Figure 2.14. Maximum end displacement (two-mode approximation, $\tilde{\Omega} = 0.6$) vs. $\tilde{b}$ and vs. $\tilde{c}_{11}$: (a) Variation with $\tilde{b}$; (b) Variation with $\tilde{c}_{11}$.

Table 2.4. Comparison of results for two-mode analysis and one-mode analysis

$\tilde{c}_{11}$	$\tilde{b}$	$\tilde{\Omega}=1,\ \tau=251.327$				$\tilde{\Omega}=3,\ \tau=83.7758$			
		TWO-MODE		ONE-MODE		TWO-MODE		ONE-MODE	
		$\tilde{u}_1$	$-\tilde{u}_3$	n = 1	n = 2	$\tilde{u}_1$	$-\tilde{u}_3$	n = 1	n = 2
0.05	0.25	-0.462836	-0.0381311	-0.457969	-0.0414161	-0.121409	0.000977935	-0.122260	0.000916859
	0.75	-0.0778820	-0.0435757	-0.0747891	-0.0407698	-0.123170	0.00910750	-0.123925	0.00938696
0.10	0.25	-0.933701	-0.0355868	-0.916428	-0.0418021	-0.118332	0.00222186	-0.120152	0.00184299
	0.75	-0.164235	-0.0445840	-0.149575	-0.0404729	-0.120879	0.0191699	-0.123579	0.0196368

NOTE: $\tilde{d}_e = 0.01$, $\tilde{d}_o = \tilde{d}_t = 0.1$, initial displacement = initial velocity = 0

where A_n is as defined in equation (2.22a). Since the system is piecewise linear, in order to find the natural frequency of the system, it is necessary to consider the period of motion as the sum of the half-periods of motion for the open and closed phases. Denoting the period of motion as T, with suitable subscripts, the required T_{system} is

$$T_{system} = \frac{1}{2}(T_{open}) + \frac{1}{2}(T_{closed}) \tag{2.33a}$$

or

$$\frac{2\pi}{\tilde{\omega}_{system}} = \frac{1}{2}\left(\frac{2\pi}{\tilde{\omega}_{open}}\right) + \frac{1}{2}\left(\frac{2\pi}{\tilde{\omega}_{closed}}\right) \tag{2.33b}$$

where $\tilde{\omega}$ is the nondimensional natural frequency of the appropriate phase. Using equation (2.22a),

$$\tilde{\omega}^2_{open} = A_n|_{\Lambda=1} = (2n-1)^2[1 - \tilde{c}_{11}(\cos \gamma_n \tilde{b})^2] \tag{2.34a}$$

and

$$\tilde{\omega}^2_{closed} = A_n|_{\Lambda=0} = (2n-1)^2 \tag{2.34b}$$

After some algebra, the system natural frequency is (for any n)

$$\tilde{\omega}_{system} = \frac{2(2n-1)\sqrt{1 - \tilde{c}_{11}(\cos \gamma_n \tilde{b})^2}}{1 + \sqrt{1 - \tilde{c}_{11}(\cos \gamma_n \tilde{b})^2}} \tag{2.35}$$

For n = 1, the system frequency reduces to

$$\tilde{\omega}_1 = \frac{2\sqrt{1 - \tilde{c}_{11}(\cos \frac{\pi}{2} \tilde{b})^2}}{1 + \sqrt{1 - \tilde{c}_{11}(\cos \frac{\pi}{2} \tilde{b})^2}} \tag{2.36}$$

Figure 2.15 illustrates how the one-mode, n = 1, natural frequency varies with respect to $\tilde{c}_{11}$ and $\tilde{b}$. Note that the slope in Figure 2.15(a) is zero at $\tilde{b} = 0$ and at $\tilde{b} = 1$, as can be verified by evaluating

$\frac{\partial \tilde{\omega}_1}{\partial \tilde{b}}$ at $\tilde{b} = 0$ and 1. Note that for a given $\tilde{b}$, as the crack moves from the fixed end to the free end, the natural frequency of the n = 1 mode increases. Also, for a given $\tilde{b}$, the frequency drops off as the compliance $\tilde{c}_{11}$ increases. This is as expected, since a larger $\tilde{c}_{11}$ implies a larger crack which decreases the axial stiffness during the open-crack phase of the motion.

For the two-mode case, an analysis of the natural frequency for free, undamped vibration is not as straightforward. In fact, it is not possible to get a frequency of motion for the two-mode case since it is not possible to define a particular mode which applies for all time. For the one-mode case, an $\tilde{\omega}_{\text{system}}$ is obtainable since there is only one mode governing for all time; the nonlinearity cannot cause a change in mode shape because there is no other mode shape. However, for the two-mode case, the nonlinearity may cause a change in mode at the transition point.

Despite the difficulty discussed above, it can be assumed for investigation purposes that the natural frequency can be obtained in the same manner as for the one-mode case. An $\tilde{\omega}_{\text{pseudo}}$ can be computed by assuming that a mode remains in place for all time. Using the same logic as for the one-mode case, and noting that for the first mode (n = 1), $\tilde{\omega}_{\text{closed}} = 1$, the lower (fundamental) frequency is

$$\tilde{\omega}_{\text{pseudo}} = 2\left(\frac{\tilde{\omega}_{\text{open}}}{1 + \tilde{\omega}_{\text{open}}} \right) \tag{2.37}$$

Figure 2.16 illustrates how the coupling affects the natural frequencies for the first mode if it is assumed that $\tilde{\omega}_{\text{pseudo}}$ is an accurate representation of the fundamental frequency in the two-mode case. Since a closed-form solution for $\tilde{\omega}_{\text{open}}$ is difficult to obtain, the values in the graph are obtained numerically. As the graphs show, the pseudo-frequency is quite close to $\tilde{\omega}_1$ obtained for the one-mode case, which supports the earlier finding that the effect of the coupling terms is small.

The results so far are based on all initial conditions being equal to zero. Yet, for free, undamped vibrations, the choice of initial conditions may greatly affect the resulting behavior. To check this,

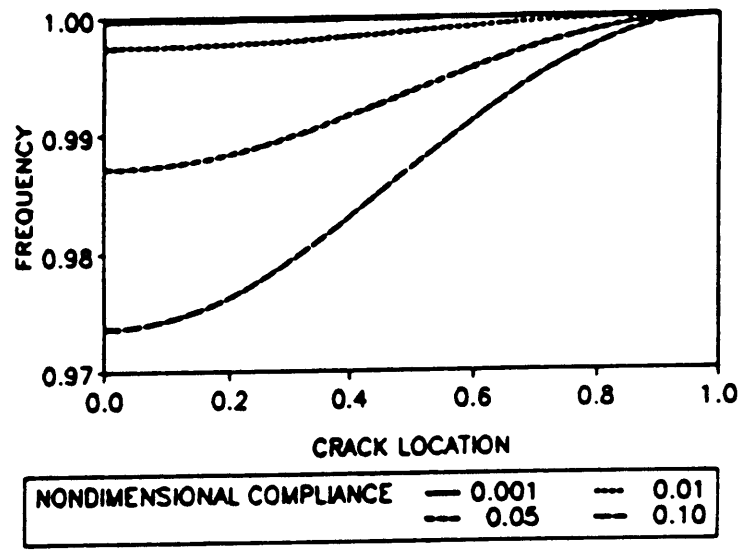

(a)

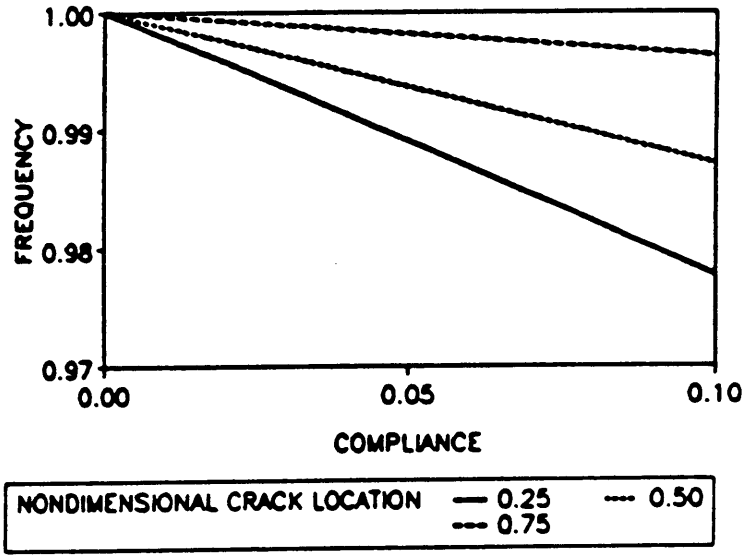

(b)

Figure 2.15. Natural frequency variation for one mode, n = 1: (a) $\tilde{\omega}_1$ vs. $\tilde{b}$; (b) $\tilde{\omega}_1$ vs. $\tilde{c}_{11}$.

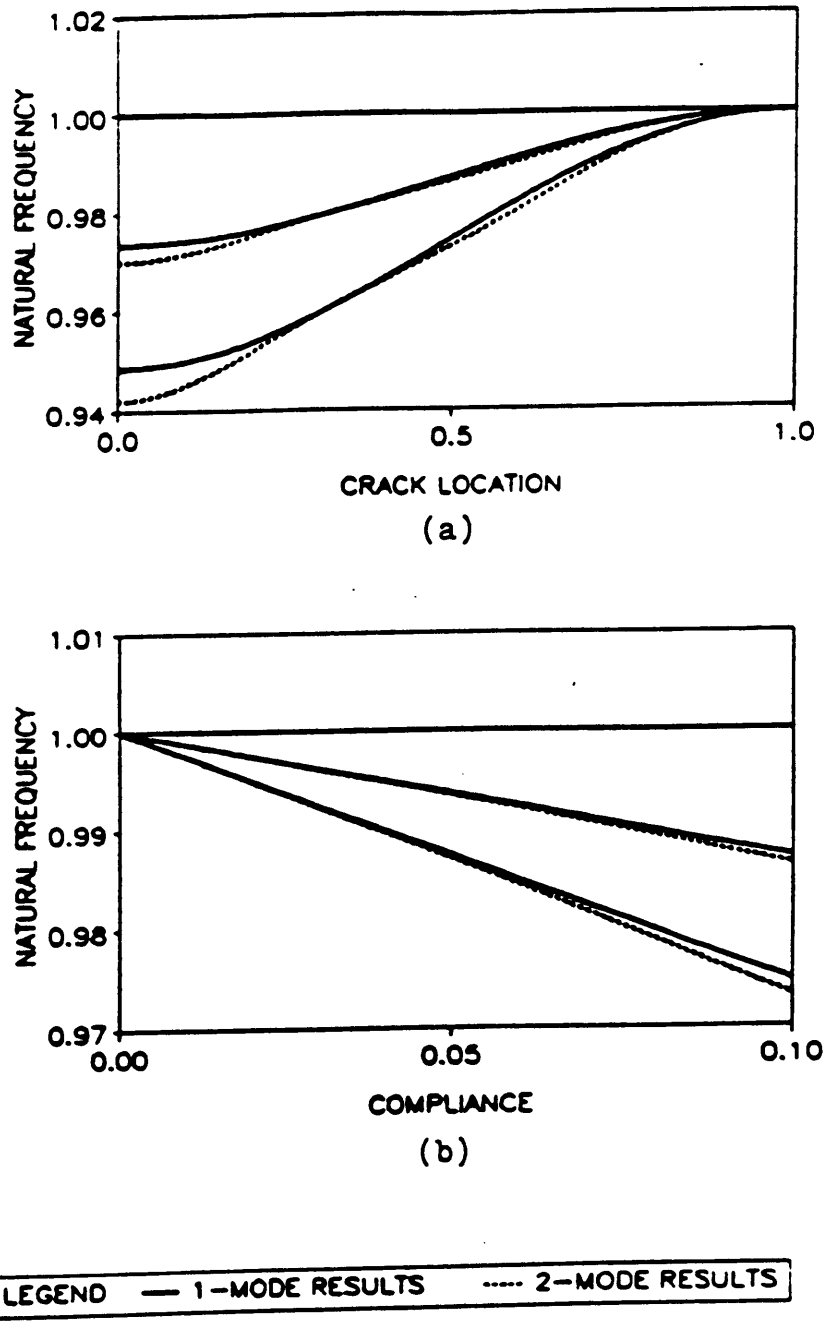

Figure 2.16. Natural frequency variation for $n = 1$, both one- and two-mode cases: (a) $\tilde{\omega}_1$ and $\tilde{\omega}_{pseudo}$ vs. $\tilde{b}$; (b) $\tilde{\omega}_1$ and $\tilde{\omega}_{pseudo}$ vs. $\tilde{c}_{11}$. Top and bottom curves represent the frequency components for the closed-crack and open-crack phases, respectively, and the middle curves represent the overall frequencies.

Figures 2.17-2.19 illustrate how initial conditions influence the two-mode approximation for free, undamped vibration. The three cases are as follows:

Case A-Figure 2.17: $\tilde{u}_1|_{\tau=0} = 1.0$ and $\tilde{u}_2|_{\tau=0} = 0.1$

Case B-Figure 2.18: $\tilde{u}_1|_{\tau=0} = 0.5$ and $\tilde{u}_2|_{\tau=0} = 0.5$

Case C-Figure 2.19: $\tilde{u}_1|_{\tau=0} = 0.1$ and $\tilde{u}_2|_{\tau=0} = 1.0$

In all three cases, $\frac{d\tilde{u}_1}{d\tau}|_{\tau=0} = \frac{d\tilde{u}_2}{d\tau}|_{\tau=0} = 0$ and all other parameters have their standard case values. It is important to re-emphasize that the "second mode" graphs reflect the behavior of $-\tilde{u}_2(\tau)$ as in Section 2.5. As the figures show, the resulting vibrational behavior is greatly dependent on initial conditions. Figures 2.18 and 2.19 reveal that the "second mode" can make significant contributions to the overall behavior of the "combined modes" if the ratio of the initial value of $\tilde{u}_2$ to $\tilde{u}_1$ is sufficiently large.

The spectral analysis for Case A is shown in Figure 2.20. As with the earlier spectral analysis, the uncracked bar is compared with the cracked bar. Very little difference between the two graphs is noted. The spectrum for the cracked bar shows a response at the origin which represents the off-center response induced by the crack. The dominant peaks occur near the natural frequencies of the uncracked bar (i.e., near 1 and 3 for the first and second modes, respectively).

To conclude this section, the results of an investigation into the existence of beat phenomena in cracked bars are presented. Figures 2.21 through 2.23 provide time histories of the "combined modes", "first mode", and "second mode" for Case A studied earlier. The graphs indicate that a beat phenomenon does indeed exist. However, the transfer of energy does not take place *between* modes, as might be expected. Instead, the energy transfer appears to take place *within* the second mode alone. (Again, "second mode" implies $-\tilde{u}_2(\tau)$.) This behavior within the second mode affects the overall behavior as can be seen in Figure 2.21, where the slowly-varying amplitude of the overall motion with time is apparent.

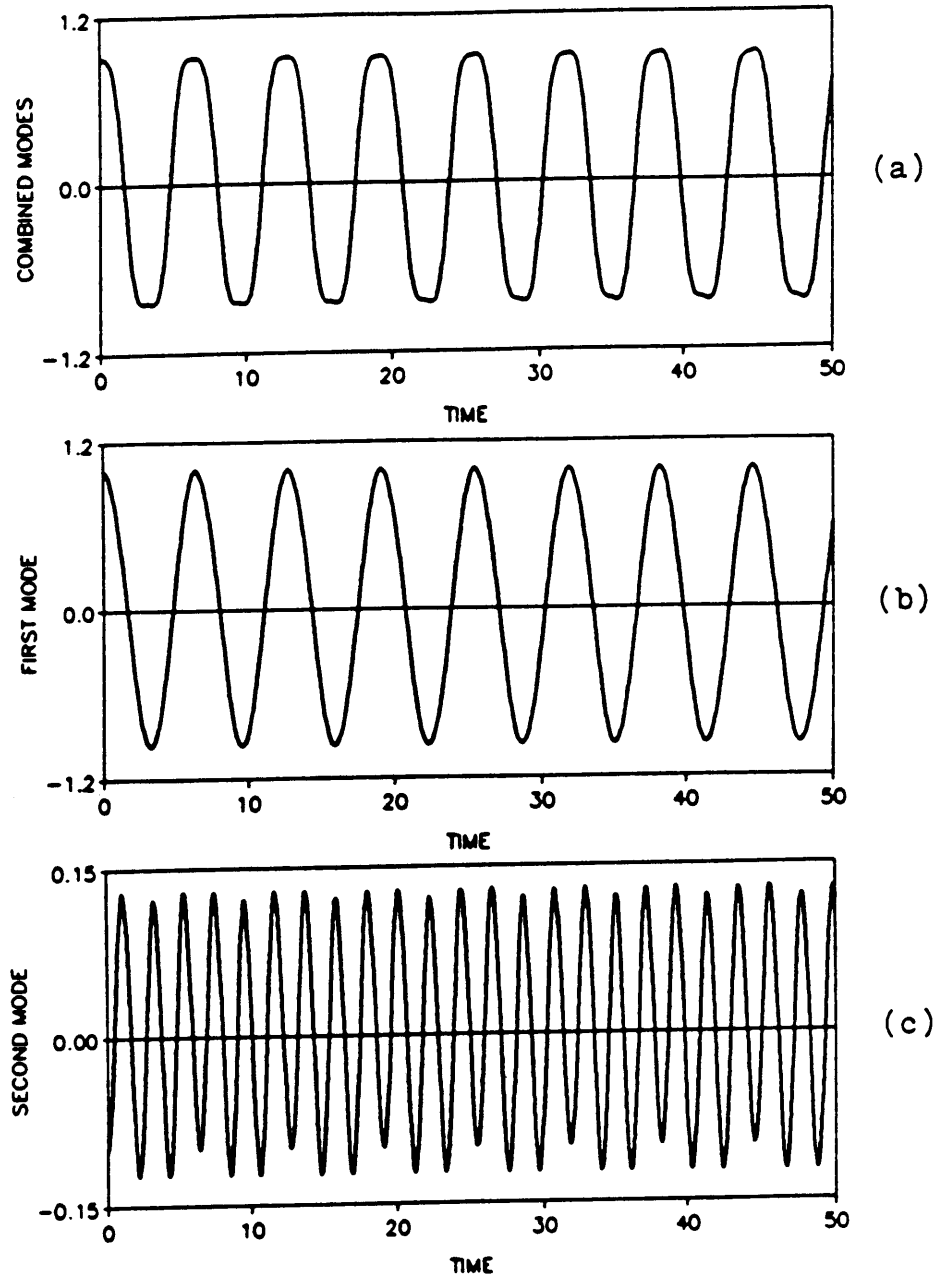

Figure 2.17. Time history plot (two-mode approximation) for free, undamped vibration (Case A): (a) $\tilde{u}_1 - \tilde{u}_2$; (b) $\tilde{u}_1$; (c) $-\tilde{u}_2$. Initial Conditions: $\tilde{u}_1|_{\tau=0} = 1.0$ and $\tilde{u}_2|_{\tau=0} = 0.1$.

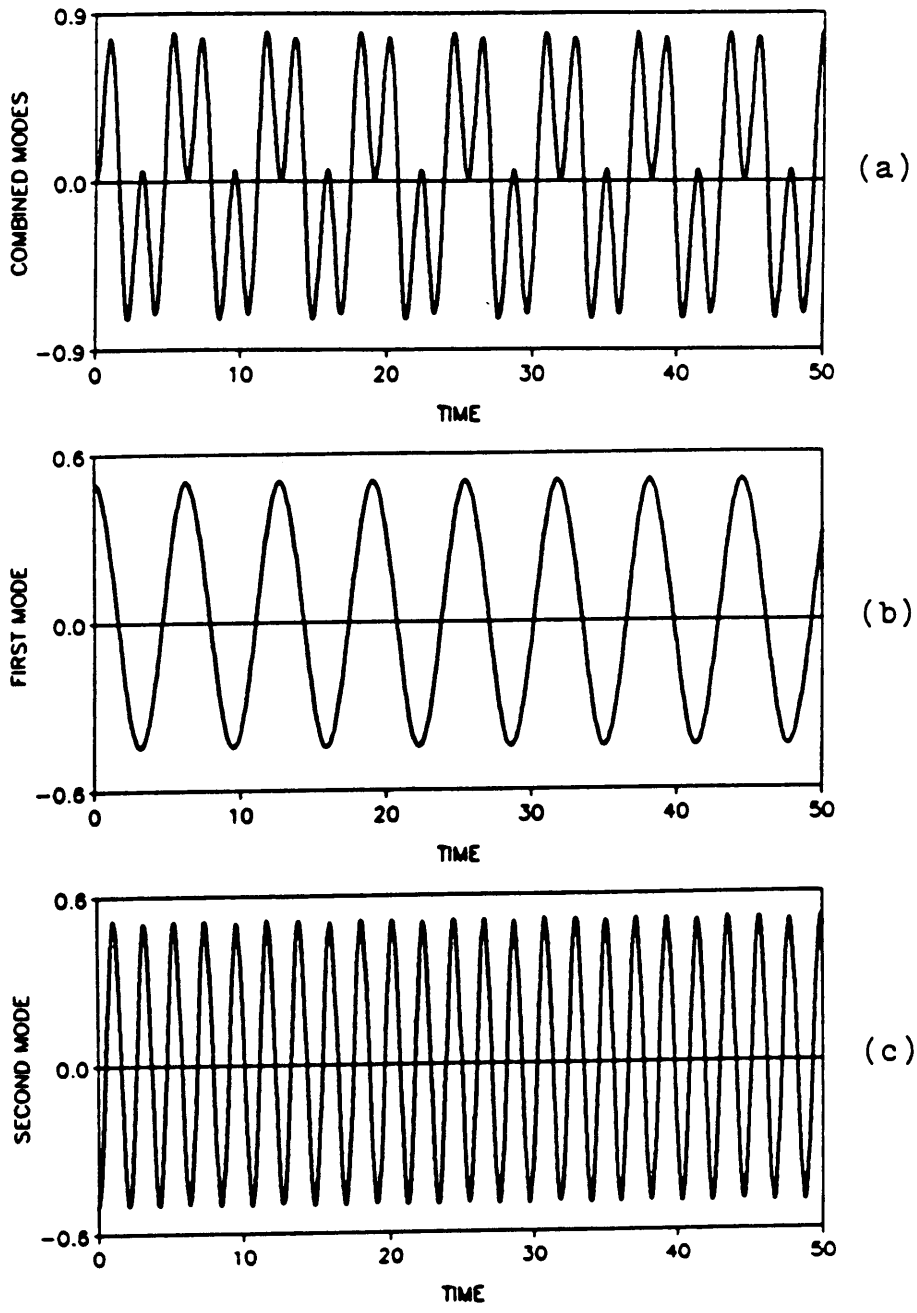

Figure 2.18. Time history plot (two-mode approximation) for free, undamped vibration (Case B): (a) $\tilde{u}_1 - \tilde{u}_2$; (b) $\tilde{u}_1$; (c) $-\tilde{u}_2$. Initial Conditions: $\tilde{u}_1|_{\tau=0} = 0.5$ and $\tilde{u}_2|_{\tau=0} = 0.5$.

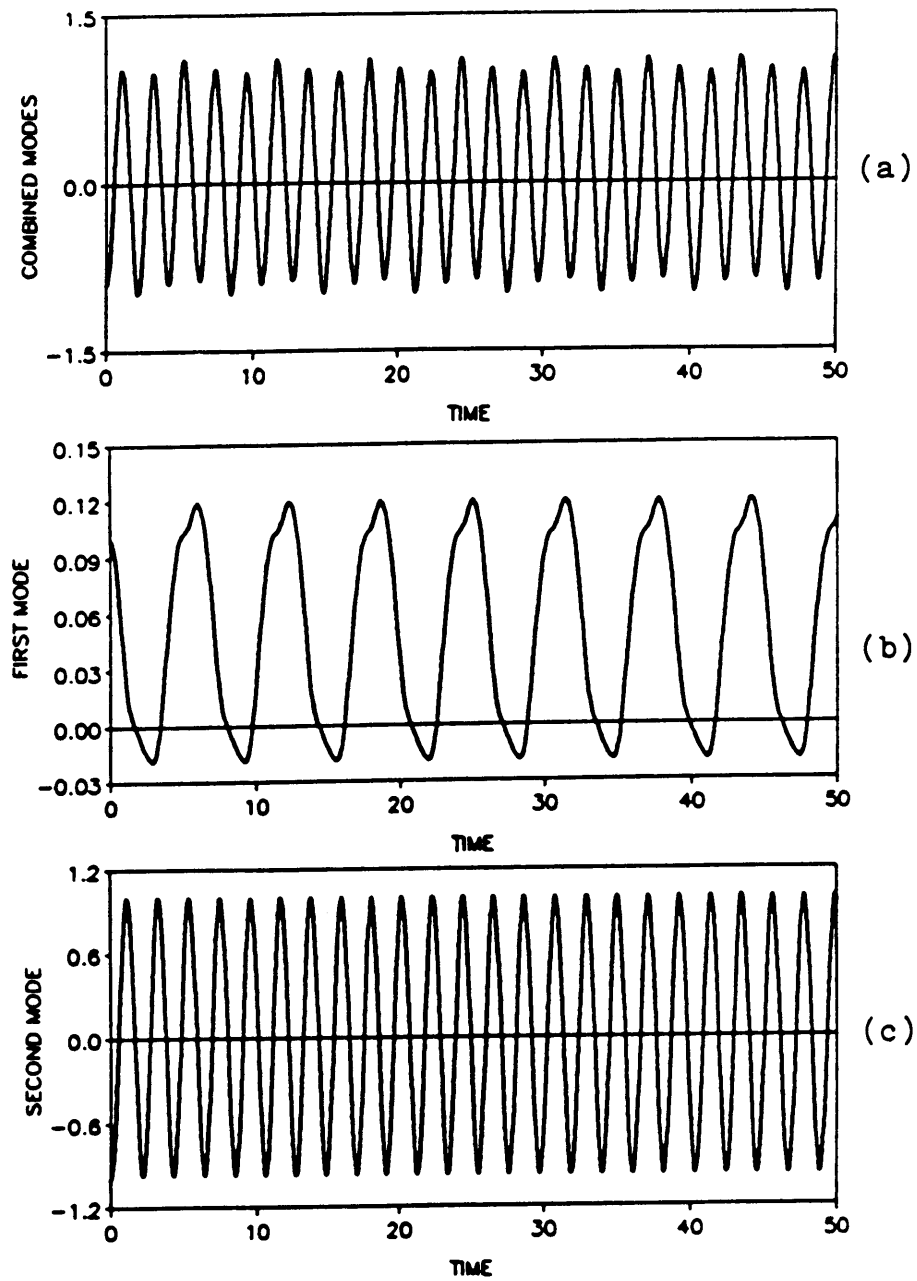

Figure 2.19. Time history plot (two-mode approximation) for free, undamped vibration (Case C): (a) $\tilde{u}_1 - \tilde{u}_2$; (b) $\tilde{u}_1$; (c) $-\tilde{u}_2$. Initial Conditions: $\tilde{u}_1|_{\tau=0} = 0.1$ and $\tilde{u}_2|_{\tau=0} = 1.0$.

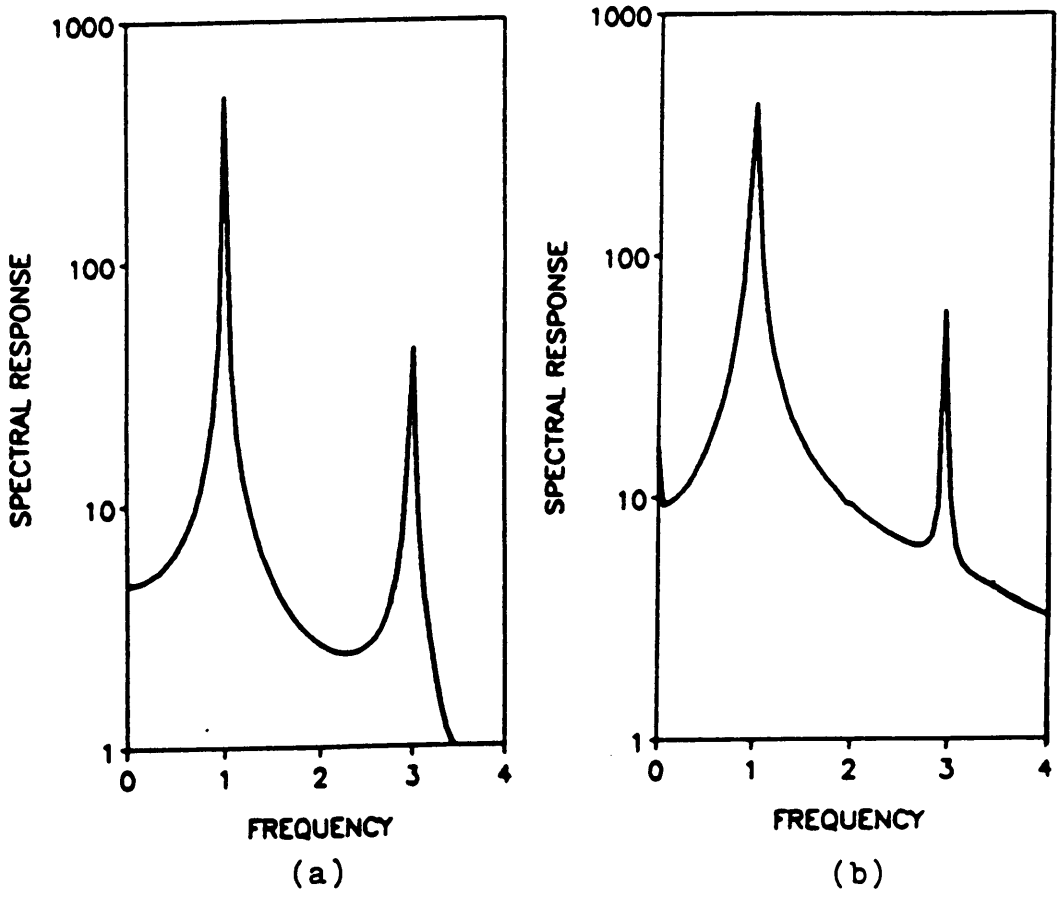

Figure 2.20. Spectra for free, undamped vibration (two-mode approximation, Case A): (a) Uncracked bar; (b) cracked bar. Responses occur near the natural frequencies of the uncracked bar. Spectral response scale factor = 1/500.

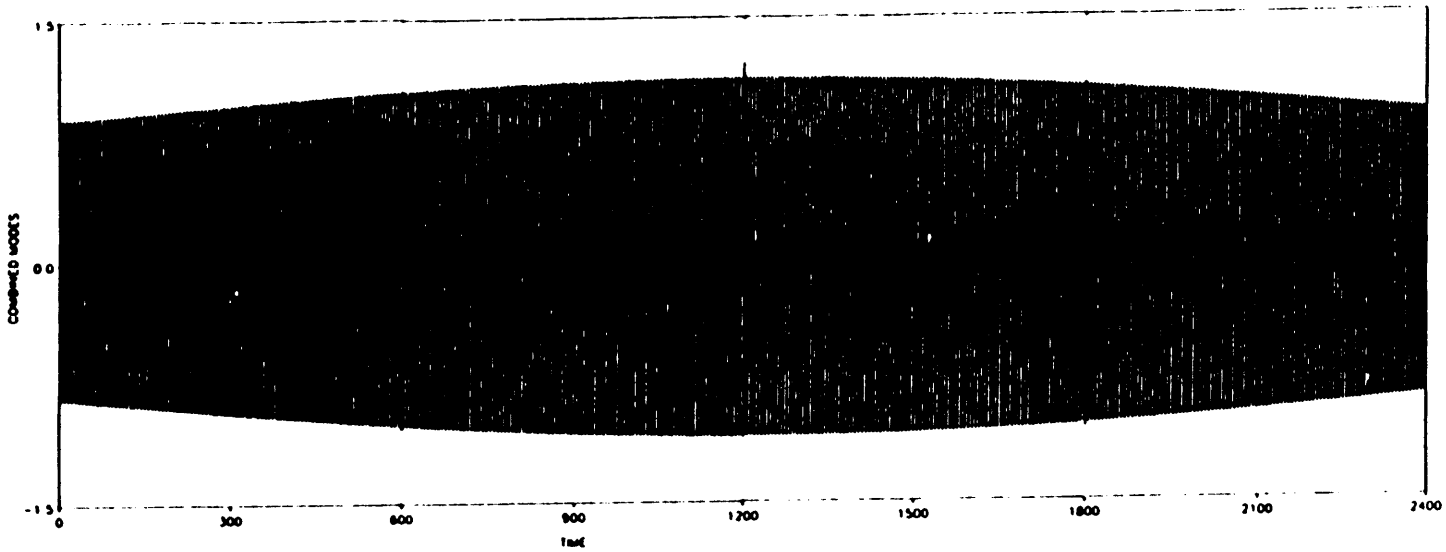

Figure 2.21. Beat phenomenon-combined modes (Case A): Beat phenomenon characterized by slowly varying amplitude over time.

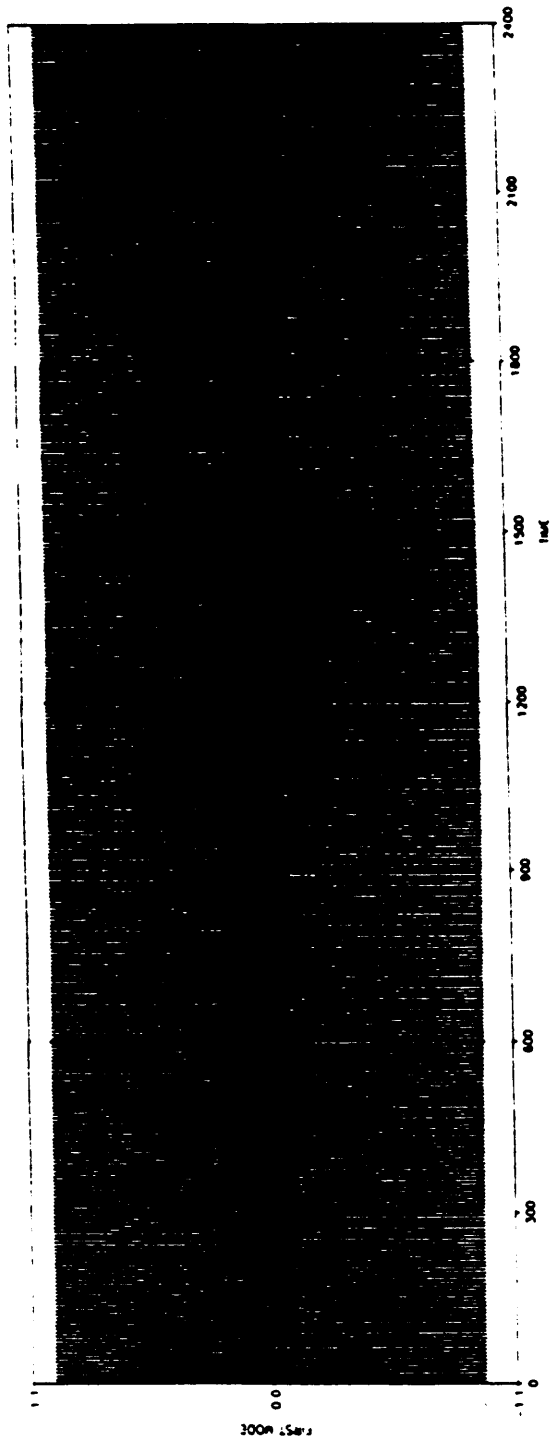

Figure 2.22. Beat phenomenon-first mode (Case A): Graph docsn't indicate the presence of any beat in this mode.

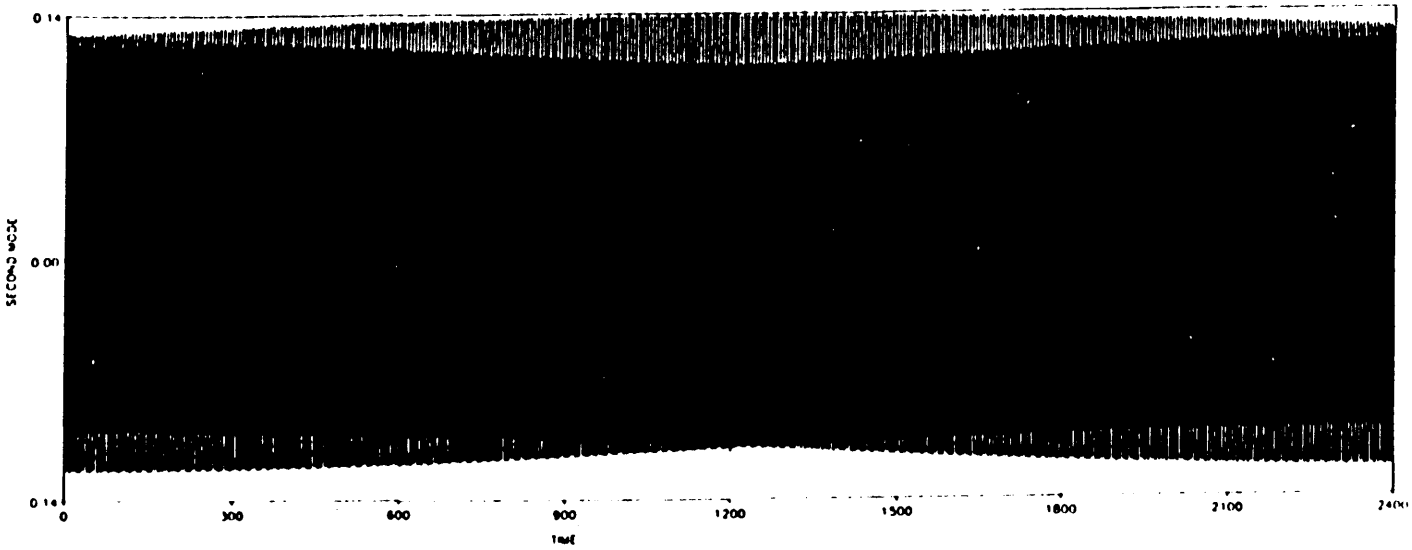

Figure 2.23. Beat phenomenon-second mode (Case A): Beat phenomenon is readily apparent.

2.7 Sensitivity Analysis

The final portion of the longitudinal vibration study consists of a sensitivity analysis. In particular, the sensitivity analysis to follow focuses on the sensitivity of the maximum end displacement to the onset of cracking.

Figure 2.24 presents the results of the sensitivity analysis described above. Figure 2.24(a) corresponds to a one-term, n = 1 approximation of the vibrational behavior, while Figure 2.24(b) applies to the two-term approximation. In both figures, the ordinate axis is the sensitivity measure, which is a forward difference quantity defined as

$$\text{sensitivity measure} = \frac{\Delta\tilde{u}_{max}}{\Delta\tilde{c}_{11}} \tag{2.38a}$$

where

$$\Delta\tilde{u}_{max} = \tilde{u}_{max}(\tilde{c}_{11} = 0.01) - \tilde{u}_{max}(\tilde{c}_{11} = 0.0) \tag{2.38b}$$

The abscissa represents the forcing frequency, $\tilde{\Omega}$, of the applied loading as shown in Figure 2.1(a). For both graphs, the crack location is at the middle of the bar ($\tilde{b} = 0.5$). The computed points are indicated by solid dots and are connected by straight lines.

The graphs in Figure 2.24 illustrate how the sensitivity measure is most significant near the lowest natural frequency, which is in the neighborhood of $\tilde{\omega} = 1$ for both the one-term and two-term approximations. This type of behavior agrees with the results of Wang and Zhang (1987) in their sensitivity study of transfer functions. The "unique" feature of each graph is the negative peak which occurs immediately after the maximum sensitivity measure. Wang and Zhang (1987) also present graphs with this feature. This negative peak seems to imply that the end displacement decreases as the compliance increases (stiffness decreases). Intuitively, this doesn't make sense. However, it must be noted that although the end displacement may decrease, internal displacements

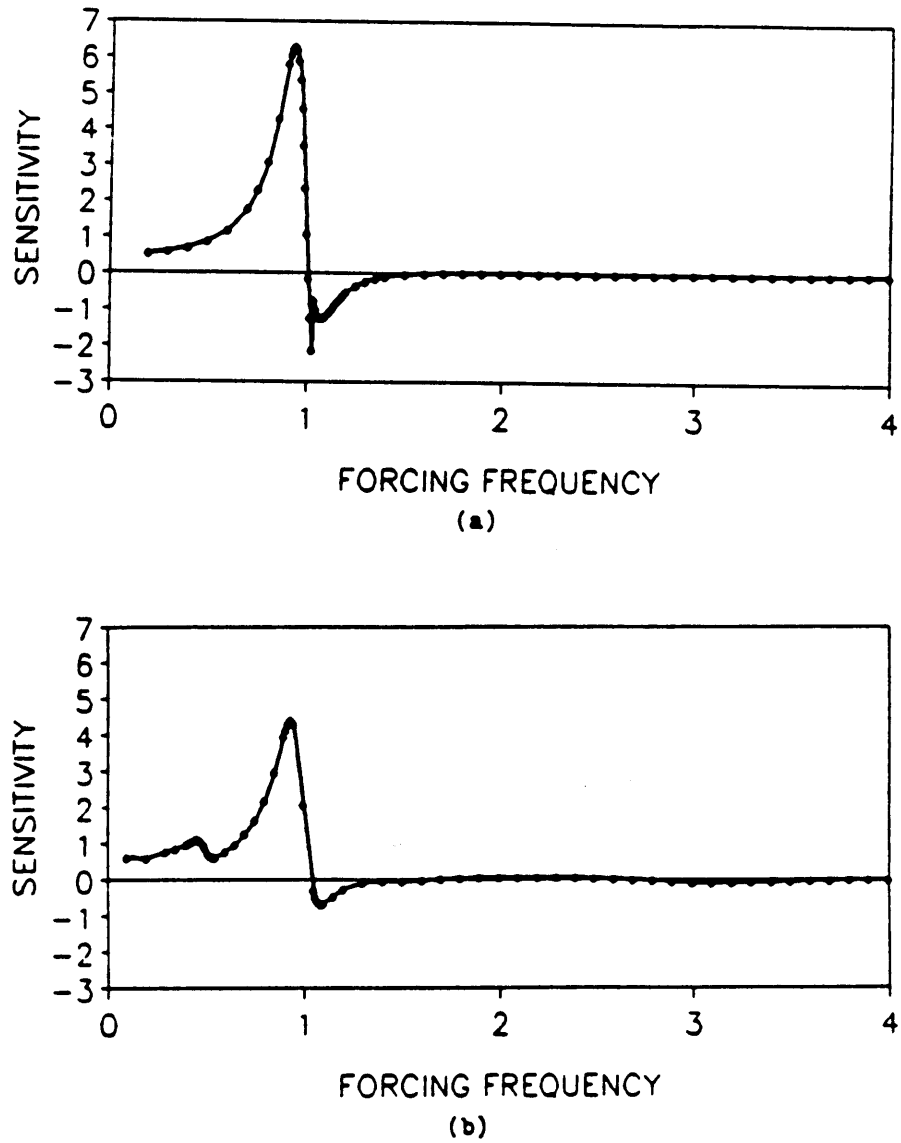

Figure 2.24. **Sensitivity of maximum response to the onset of a crack:** (a) Sensitivity of the one-term, $n=1$ approximation vs. forcing frequency $\tilde{\Omega}$; (b) Sensitivity of the two-term approximation vs. $\tilde{\Omega}$.

may increase. If intuition is correct, the negative peaks imply that the approximate solutions are only accurate for certain ranges of forcing frequency. Figure 2.24(a) shows that the one-term approximation may be good only for $\tilde{\Omega}$ less than 1. Note that the negative peak in Figure 2.24(b) has decreased in magnitude and that a much smaller positive peak occurs between $\tilde{\Omega} = 1$ and $\tilde{\Omega} = 3$. These two features of Figure 2.24(b) indicate that the two-term approximation is an improved approximation and may be accurate for $\tilde{\Omega}$ less than 2.

Chapter 3

Coupled Vibrations of a Rotating Timoshenko Shaft with a Crack

3.1 Physical Model

The modelling used here is the same as that used by Wauer (b). The following paragraphs summarize his description of the problem.

Figure 3.1(a) represents a uniform shaft of length L rotating at a constant angular speed Ω. It has a transverse surface crack at a distance b from the left end. In the equations to follow, it is assumed that only one such crack exists along the length of the shaft. The shaft is oriented in a stationary x,y,z coordinate system with the x-axis coinciding with the axis of the shaft (i.e., through the centroids of the cross-sections of the uncracked shaft). The positive z-axis is assumed to be in the direction of gravity (when the x-axis is horizontal), and the y-axis is located accordingly for a right-handed coordinate system.

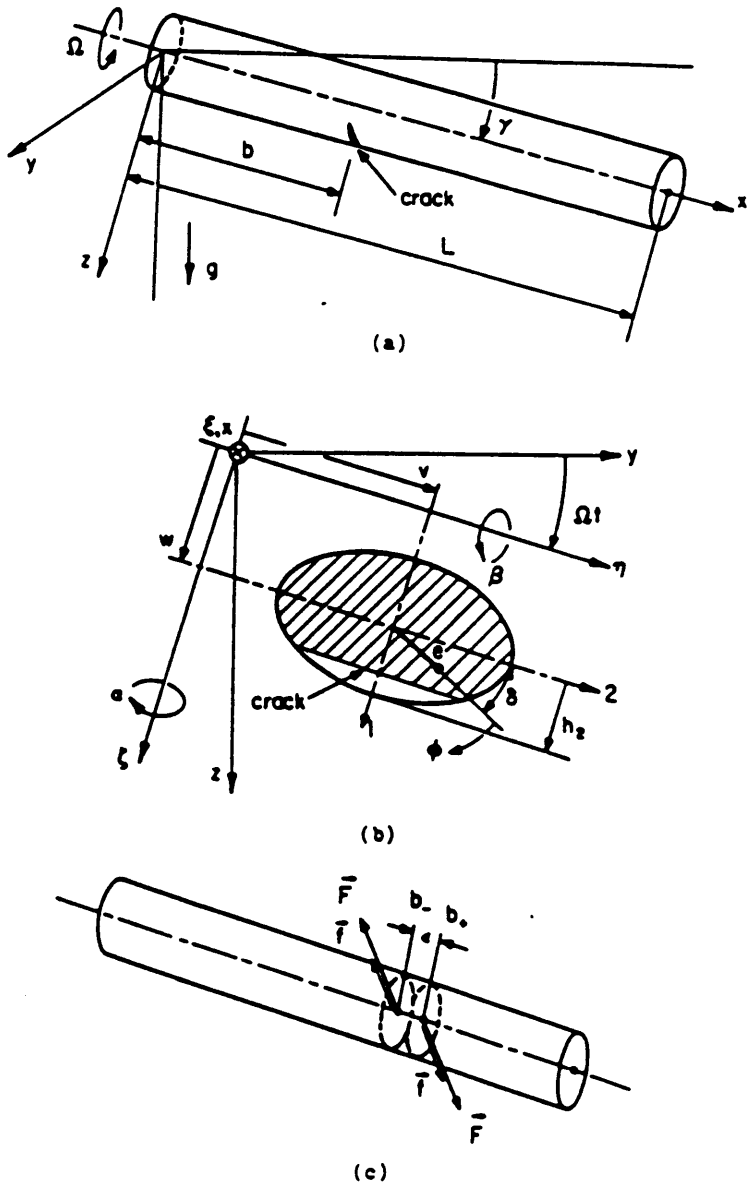

Figure 3.1. Models: (a) Physical model of the cracked shaft; (b) Definition of coordinate systems and crack position; (c) Uniform shaft with generalized force vectors $\vec{F}$ and $\vec{f}$ which model the local change in stiffness and damping for an open crack.

In the most general case, the shaft is noncircular but axially-symmetric and composed of a viscoelastic material. Also, the centroid of the cross-section is permitted to differ from the mass center of the shaft. Furthermore, the x-axis may be inclined with respect to the horizontal plane.

The following notation will be used to model the properties (dimensional quantities) of the shaft:

μ = mass per unit length

E = modulus of elasticity of the material (constant)

A = cross-sectional area of the shaft (constant)

I_1, I_2 = moments of inertia about the principal axes

J = torsional constant

G = shear modulus (constant)

κ_1, κ_2 = shape coefficients about principal axes

r_1, r_2 = radii of gyration about principal axes

h_2 = distance from the geometric center of the uncracked cross-section to the perimeter of the shaft (measured along the 1-axis)

b = crack location ($0 < b < L$)

e = eccentricity of center of mass

δ = location angle of center of mass

γ = angle between the x-axis and the horizontal plane

d_e = external viscous damping coefficient

d_i = internal (viscoelastic) damping coefficient

d_c = dry friction damping coefficient at the crack

ε = crack width parameter

t = time

g = acceleration of gravity

The displacements of the shaft are measured from a body-fixed rotating reference frame ξ,η,ζ, with the ξ-axis coinciding with the x-axis of the stationary x,y,z coordinate system (see Figure 3.1(b)). The plane 1,2 coordinate system represents the principal axes of the cross-section. The crack is assumed to have a straight edge and to be oriented such that its edge is parallel to the 2-axis, which is the worst orientation (Wauer, b; Muszynska, 1982). In all pairs of quantities with subscripts 1 and 2, the quantities with subscript 2 are the smaller of the two for a noncircular shaft. In relation to the rotating ξ,η,ζ coordinate system, the 2-axis is parallel with the η-axis (see Figure 3.1(b)).

To completely describe the motion of the shaft, six displacements are needed (see Figure 3.1(b)). The Timoshenko shaft is assumed to be flexible both longitudinally and torsionally with displacements u(x,t) and ϕ(x,t), respectively. The transverse displacement in the strong direction is v(x,t), while w(x,t) represents the transverse displacement in the weak direction. Finally, α(x,t) is the angle of inclination of the cross-section about the weak axis, while β(x,t) is the corresponding angle of inclination about the strong axis.

3.2 Mathematical Model

The details of the derivation of the governing equations of motion will not be discussed here - the interested reader is referred to Wauer (b). However, several general comments are warranted. First, the mathematical model accounts for gyroscopic effects, shear deformation and rotatory inertia. Secondly, as in Chapter 2, the effect of a crack is represented by two pairs of generalized force vectors $\vec{F}$ and $\vec{f}$ which model the change in stiffness and damping, respectively, due to the crack (see Figure 3.1(c)). The magnitudes of these forces are dependent on the crack depth, the loading (if any), and the geometry of the shaft. Finally, unlike Chapter 2, the crack in the shaft is one-sided and therefore is not a symmetric discontinuity.

The six equations of motion derived by Wauer (b), presented here in modified form, are as follows:

$$\begin{aligned}&\mu u_{tt} + d_e\mu u_t + (1-\Lambda)d_c\delta(x-b)\mu u_t - \mathrm{E}\Lambda(u_{xx} + d_i u_{txx}) - \mu g \sin\gamma \\ &\quad - \Lambda[\delta(x-b_+) - \delta(x-b_-)](F_x + f_x) = 0\end{aligned} \tag{3.1a}$$

$$\begin{aligned}&\mu(v_{tt} - 2\Omega w_t - \Omega^2 v) + d_e\mu(v_t - \Omega w) + (1-\Lambda)d_c\delta(x-b)\mu(v_t - \Omega w) \\ &- \kappa_1 \mathrm{GA}[v_{xx} - \alpha_x + d_i(v_{txx} - \alpha_{tx})] - e\mu(\Omega^2 + 2\Omega\phi_t)\cos\delta - e\mu(\phi_{tt} - \Omega^2\phi)\sin\delta \\ &\quad - \mu g \cos\gamma \sin\Omega t - \Lambda[\delta(x-b_+) - \delta(x-b_-)](F_\eta + f_\eta) = 0\end{aligned} \tag{3.1b}$$

$$\begin{aligned}&\mu(w_{tt} + 2\Omega v_t - \Omega^2 w) + d_e\mu(w_t + \Omega v) + (1-\Lambda)d_c\delta(x-b)\mu(w_t + \Omega v) \\ &- \kappa_2 \mathrm{GA}[w_{xx} + \beta_x + d_i(w_{txx} + \beta_{tx})] - e\mu(\Omega^2 + 2\Omega\phi_t)\sin\delta + e\mu(\phi_{tt} - \Omega^2\phi)\cos\delta \\ &\quad - \mu g \cos\gamma \cos\Omega t - \Lambda[\delta(x-b_+) - \delta(x-b_-)](F_\zeta + f_\zeta) = 0\end{aligned} \tag{3.1c}$$

$$\begin{aligned}&\mu r_1^2(\alpha_{tt} + \Omega^2\alpha) + d_e\mu r_1^2\alpha_t + (1-\Lambda)d_c\delta(x-b)\mu r_1^2\alpha_t \\ &- \mathrm{EI}_1(\alpha_{xx} + d_i\alpha_{txx}) - \kappa_1\mathrm{GA}[v_x - \alpha + d_i(v_{tx} - \alpha_t)] \\ &\quad - \Lambda[\delta(x-b_+) - \delta(x-b_-)](M_\zeta + m_\zeta) = 0\end{aligned} \tag{3.1d}$$

$$\begin{aligned}&\mu r_2^2(\beta_{tt} + \Omega^2\beta) + d_e\mu r_2^2\beta_t + (1-\Lambda)d_c\delta(x-b)\mu r_2^2\beta_t \\ &- \mathrm{EI}_2(\beta_{xx} + d_i\beta_{txx}) + \kappa_2\mathrm{GA}[w_x + \beta + d_i(w_{tx} + \beta_t)] \\ &\quad - \Lambda[\delta(x-b_+) - \delta(x-b_-)](M_\eta + m_\eta) = 0\end{aligned} \tag{3.1e}$$

$$\mu(r_1^2 + r_2^2)\phi_{tt} + d_e\mu(r_1^2 + r_2^2)\phi_t + (1 - \Lambda)d_c\delta(x - b)\mu(r_1^2 + r_2^2)\phi_t$$
$$- GJ(\phi_{xx} + d_i\phi_{txx}) - e\mu(v_{tt} - 2\Omega w_t - \Omega^2 v)\sin\delta + e\mu(w_{tt} + 2\Omega v_t - \Omega^2 w)\cos\delta \qquad (3.1f)$$
$$- e\mu g\cos\gamma\cos(\delta + \Omega t) - \Lambda[\delta(x - b_+) - \delta(x - b_-)](M_x + m_x) = 0$$

In the above equations, the subscripts x and t represent partial derivatives with respect to the axial coordinate and time, respectively. The equations apply for $0 < x < L$. The major modification from Wauer (b) in the above presentation is that both the open and closed crack equations are represented by incorporating the Λ notation as used in Chapter 2. Mathematically,

$$\Lambda = \begin{cases} 1 \text{ for an open crack} \\ 0 \text{ for a closed crack} \end{cases} \qquad (2.3)$$

The values of the components of the generalized force vectors $\vec{F}$ and $\vec{f}$ are determined by the same general approach as that used in Chapter 2. The details are discussed by Wauer (b). Their values are as follows, where the right-hand sides are evaluated at $x = b_+$:

$$F_x + f_x = c_{11}\frac{(EA)^2}{\varepsilon}[u_x + d_i u_{tx}] + c_{15}\frac{E^2 I_2 A}{\varepsilon}[\beta_x + d_i\beta_{tx}] \qquad (3.2a)$$

$$F_\eta + f_\eta = c_{22}\frac{(\kappa_1 GA)^2}{\varepsilon}[v_x - \alpha + d_i(v_{tx} - \alpha_t)] + c_{26}\frac{\kappa_1 G^2 JA}{\varepsilon}[\phi_x + d_i\phi_{tx}] \qquad (3.2b)$$

$$F_\zeta + f_\zeta = c_{33}\frac{(\kappa_2 GA)^2}{\varepsilon}[w_x + \beta + d_i(w_{tx} + \beta_t)] \qquad (3.2c)$$

$$M_\zeta + m_\zeta = c_{44}\frac{(EI_1)^2}{\varepsilon}[\alpha_x + d_i\alpha_{tx}] \qquad (3.2d)$$

$$M_\eta + m_\eta = c_{51}\frac{E^2 I_2 A}{\varepsilon}[u_x + d_i u_{tx}] + c_{55}\frac{(EI_2)^2}{\varepsilon}[\beta_x + d_i\beta_{tx}] \qquad (3.2e)$$

$$M_x + m_x = c_{62}\frac{\kappa_1 G^2 JA}{\varepsilon}[v_x - \alpha + d_i(v_{tx} - \alpha_t)] + c_{66}\frac{(GJ)^2}{\varepsilon}[\phi_x + d_i\phi_{tx}] \qquad (3.2f)$$

It is important to note that Wauer (b) derives equations (3.1) under the assumption of small eccentricity, so that e^2 is negligible with respect to $r_1^2 + r_2^2$. This assumption enables the mass moment of inertia to be evaluated about the geometric center instead of the mass center.

In order to arrive at a solution to the equations of motion, a set of boundary conditions is needed. For simplicity, a set of "simple support" boundary conditions is used here. At x = L, the shaft is supported such that axial and torsional motion is permitted, while at x = 0 this motion is restrained. Mathematically, the "simple support" boundary conditions are

$$u(0,t) = v(0,t) = w(0,t) = \alpha_x(0,t) = \beta_x(0,t) = \phi(0,t) = 0 \tag{3.3a}$$

$$u_x(L,t) = v(L,t) = w(L,t) = \alpha_x(l,t) = \beta_x(L,t) = \phi_x(L,t) = 0 \tag{3.3b}$$

These boundary conditions introduce symmetry into the model so that only crack locations between x = 0 and x = L/2 need be considered. As in Chapter 2, the Galerkin Method is applied to obtain approximate solutions. The set of functions used here, which satisfy all of the boundary conditions above, are

$$u(x, t) = \sum_{k=1}^{N} u_k(t) \sin \theta_k x \tag{3.4a}$$

$$v(x, t) = \sum_{k=1}^{N} v_k(t) \sin \frac{k\pi x}{L} \tag{3.4b}$$

$$w(x, t) = \sum_{k=1}^{N} w_k(t) \sin \frac{k\pi x}{L} \tag{3.4c}$$

$$\alpha(x, t) = \sum_{k=1}^{N} \alpha_k(t) \cos \frac{k\pi x}{L} \tag{3.4d}$$

$$\beta(x, t) = \sum_{k=1}^{N} \beta_k(t) \cos \frac{k\pi x}{L} \tag{3.4e}$$

$$\phi(x, t) = \sum_{k=1}^{N} \phi_k(t) \sin \theta_k x \tag{3.4f}$$

where, as in Chapter 2,

$$\theta_k = \frac{(2k-1)\pi}{2L} \tag{2.15}$$

These equations and their derivatives are substituted into equations (3.1). Then, following the Galerkin procedure as outlined in Chapter 2, approximate equations of motion are obtained. After nondimensionalization, they have the following form:

$$\begin{aligned}
&\frac{d^2\tilde{u}_n}{d\tau^2} + \tilde{d}_e \frac{d\tilde{u}_n}{d\tau} + (1-\Lambda)\tilde{d}_c(\sin \gamma_n \tilde{b}) \sum_{k=1}^{N} \left[\frac{d\tilde{u}_k}{d\tau} (\sin \gamma_k \tilde{b}) \right] \\
&\qquad + (2n-1)^2 \tilde{u}_n + (2n-1)^2 \tilde{d}_l \frac{d\tilde{u}_n}{d\tau} - \frac{\tilde{\mu} \sin \gamma}{(2n-1)} \\
&- 2\Lambda \tilde{c}_{11}(2n-1)(\cos \gamma_n \tilde{b}) \sum_{k=1}^{N} \left[(2k-1)(\cos \gamma_k \tilde{b})(\tilde{u}_k + \tilde{d}_l \frac{d\tilde{u}_k}{d\tau}) \right] \\
&+ 4\Lambda \tilde{c}_{15} \tilde{r}_2^2 (2n-1)(\cos \gamma_n \tilde{b}) \sum_{k=1}^{N} \left[k(\sin k\pi \tilde{b})(\tilde{\beta}_k + \tilde{d}_l \frac{d\tilde{\beta}_k}{d\tau}) \right] = 0
\end{aligned} \tag{3.5a}$$

$$\frac{d^2\tilde{v}_n}{d\tau^2} - 2\tilde{\Omega}\frac{d\tilde{w}_n}{d\tau} - \tilde{\Omega}^2\tilde{v}_n + \tilde{d}_e\left(\frac{d\tilde{v}_n}{d\tau} - \tilde{\Omega}\tilde{w}_n\right)$$

$$+ (1-\Lambda)\tilde{d}_c(\sin n\pi\tilde{b})\sum_{k=1}^{N}\left[(\sin k\pi\tilde{b})\left(\frac{d\tilde{v}_k}{d\tau} - \tilde{\Omega}\tilde{w}_k\right)\right] + 4\tilde{\kappa}_1 n^2\left(\tilde{v}_n + \tilde{d}_i\frac{d\tilde{v}_n}{d\tau}\right)$$

$$- \frac{4}{\pi}\tilde{\kappa}_1 n\left(\tilde{\alpha}_n + \tilde{d}_i\frac{d\tilde{\alpha}_n}{d\tau}\right) - \frac{2\tilde{e}}{n\pi}\tilde{\Omega}^2(\cos\delta)[1-(-1)^n] - \frac{\tilde{\mu}}{2n}\cos\gamma(\sin\tilde{\Omega}\tau)[1-(-1)^n]$$

$$- \frac{16}{\pi}\tilde{e}\tilde{\Omega}(\cos\delta)n(-1)^n\sum_{k=1}^{N}\frac{(-1)^k\frac{d\tilde{\phi}_k}{d\tau}}{[4n^2-(2k-1)^2]} \tag{3.5b}$$

$$- \frac{8}{\pi}\tilde{e}(\sin\delta)n(-1)^n\sum_{k=1}^{N}\frac{(-1)^k\left(\frac{d^2\tilde{\phi}_k}{d\tau^2} - \tilde{\Omega}^2\tilde{\phi}_k\right)}{[4n^2-(2k-1)^2]}$$

$$- \Lambda\frac{8}{\pi}\tilde{c}_{22}\tilde{\kappa}_1^2 n(\cos n\pi\tilde{b})\sum_{k=1}^{N}\left[(\cos k\pi\tilde{b})\left[k\pi\left(\tilde{v}_k + \tilde{d}_i\frac{d\tilde{v}_k}{d\tau}\right) - \left(\tilde{\alpha}_k + \tilde{d}_i\frac{d\tilde{\alpha}_k}{d\tau}\right)\right]\right]$$

$$- 4\Lambda\tilde{c}_{26}\tilde{\kappa}_1 n(\cos n\pi\tilde{b})\sum_{k=1}^{N}\left[(2k-1)(\cos\gamma_k\tilde{b})\left(\tilde{\phi}_k + \tilde{d}_i\frac{d\tilde{\phi}_k}{d\tau}\right)\right] = 0$$

$$\frac{d^2\tilde{w}_n}{d\tau^2} + 2\tilde{\Omega}\frac{d\tilde{v}_n}{d\tau} - \tilde{\Omega}^2\tilde{w}_n + \tilde{d}_e\left(\frac{d\tilde{w}_n}{d\tau} + \tilde{\Omega}\tilde{v}_n\right)$$

$$+ (1-\Lambda)\tilde{d}_c(\sin n\pi\tilde{b})\sum_{k=1}^{N}\left[(\sin k\pi\tilde{b})\left(\frac{d\tilde{w}_k}{d\tau} + \tilde{\Omega}\tilde{v}_k\right)\right] + 4\tilde{\kappa}_2 n^2\left(\tilde{w}_n + \tilde{d}_i\frac{d\tilde{w}_n}{d\tau}\right)$$

$$+ \frac{4}{\pi}\tilde{\kappa}_2 n\left(\tilde{\beta}_n + \tilde{d}_i\frac{d\tilde{\beta}_n}{d\tau}\right) - \frac{2\tilde{e}}{n\pi}\tilde{\Omega}^2(\sin\delta)[1-(-1)^n] - \frac{\tilde{\mu}}{2n}\cos\gamma(\cos\tilde{\Omega}\tau)[1-(-1)^n]$$

$$- \frac{16}{\pi}\tilde{e}\tilde{\Omega}(\sin\delta)n(-1)^n\sum_{k=1}^{N}\frac{(-1)^k\frac{d\tilde{\phi}_k}{d\tau}}{[4n^2-(2k-1)^2]} \tag{3.5c}$$

$$+ \frac{8}{\pi}\tilde{e}(\cos\delta)n(-1)^n\sum_{k=1}^{N}\frac{(-1)^k\left(\frac{d^2\tilde{\phi}_k}{d\tau^2} - \tilde{\Omega}^2\tilde{\phi}_k\right)}{[4n^2-(2k-1)^2]}$$

$$- \Lambda\frac{8}{\pi}\tilde{c}_{33}\tilde{\kappa}_2^2 n(\cos n\pi\tilde{b})\sum_{k=1}^{N}\left[(\cos k\pi\tilde{b})\left[k\pi\left(\tilde{w}_k + \tilde{d}_i\frac{d\tilde{w}_k}{d\tau}\right) + \left(\tilde{\beta}_k + \tilde{d}_i\frac{d\tilde{\beta}_k}{d\tau}\right)\right]\right] = 0$$

$$\tilde{r}_1^2\left(\frac{d^2\tilde{\alpha}_n}{d\tau^2}+\tilde{d}_e\frac{d\tilde{\alpha}_n}{d\tau}+\tilde{\Omega}^2\tilde{\alpha}_n\right)+(1-\Lambda)\tilde{d}_c\tilde{r}_1^2(\cos n\pi\tilde{b})\sum_{k=1}^{N}\left[\frac{d\tilde{\alpha}_k}{d\tau}(\cos k\pi\tilde{b})\right]$$
$$+4\tilde{r}_1^2n^2\left(\tilde{\alpha}_n+\tilde{d}_i\frac{d\tilde{\alpha}_n}{d\tau}\right)-\frac{4}{\pi^2}\tilde{\kappa}_1\left[n\pi\left(\tilde{v}_n+\tilde{d}_i\frac{d\tilde{v}_n}{d\tau}\right)-\left(\tilde{\alpha}_n+\tilde{d}_i\frac{d\tilde{\alpha}_n}{d\tau}\right)\right] \tag{3.5d}$$
$$-8\Lambda\tilde{c}_{44}\tilde{r}_1^4n(\sin n\pi\tilde{b})\sum_{k=1}^{N}\left[k(\sin k\pi\tilde{b})\left(\tilde{\alpha}_k+\tilde{d}_i\frac{d\tilde{\alpha}_k}{d\tau}\right)\right]=0$$

$$\tilde{r}_2^2\left(\frac{d^2\tilde{\beta}_n}{d\tau^2}+\tilde{d}_e\frac{d\tilde{\beta}_n}{d\tau}+\tilde{\Omega}^2\tilde{\beta}_n\right)+(1-\Lambda)\tilde{d}_c\tilde{r}_2^2(\cos n\pi\tilde{b})\sum_{k=1}^{N}\left[\frac{d\tilde{\beta}_k}{d\tau}(\cos k\pi\tilde{b})\right]$$
$$+4\tilde{r}_2^2n^2\left(\tilde{\beta}_n+\tilde{d}_i\frac{d\tilde{\beta}_n}{d\tau}\right)+\frac{4}{\pi^2}\tilde{\kappa}_2\left[n\pi\left(\tilde{w}_n+\tilde{d}_i\frac{d\tilde{w}_n}{d\tau}\right)+\left(\tilde{\beta}_n+\tilde{d}_i\frac{d\tilde{\beta}_n}{d\tau}\right)\right]$$
$$+4\Lambda\tilde{c}_{51}\tilde{r}_2^2n(\sin n\pi\tilde{b})\sum_{k=1}^{N}\left[(2k-1)(\cos\gamma_k\tilde{b})\left(\tilde{u}_k+\tilde{d}_i\frac{d\tilde{u}_k}{d\tau}\right)\right] \tag{3.5e}$$
$$-8\Lambda\tilde{c}_{55}\tilde{r}_2^4n(\sin n\pi\tilde{b})\sum_{k=1}^{N}\left[k(\sin k\pi\tilde{b})\left(\tilde{\beta}_k+\tilde{d}_i\frac{d\tilde{\beta}_k}{d\tau}\right)\right]=0$$

$$(\tilde{r}_1^2+\tilde{r}_2^2)\left(\frac{d^2\tilde{\phi}_n}{d\tau^2}+\tilde{d}_e\frac{d\tilde{\phi}_n}{d\tau}\right)+(1-\Lambda)\tilde{d}_c(\tilde{r}_1^2+\tilde{r}_2^2)(\sin\gamma_n\tilde{b})\sum_{k=1}^{N}\left[\frac{d\tilde{\phi}_k}{d\tau}(\sin\gamma_k\tilde{b})\right]$$
$$+\tilde{G}\tilde{J}(2n-1)^2\left(\tilde{\phi}_n+\tilde{d}_i\frac{d\tilde{\phi}_n}{d\tau}\right)-\frac{\tilde{e}\tilde{\mu}(\cos\gamma)\cos(\delta+\tilde{\Omega}\tau)}{(2n-1)}$$
$$-\frac{8}{\pi}\tilde{e}(\sin\delta)(-1)^n\sum_{k=1}^{N}\frac{(-1)^kk\left(\frac{d^2\tilde{v}_k}{d\tau^2}-2\tilde{\Omega}\frac{d\tilde{w}_k}{d\tau}-\tilde{\Omega}^2\tilde{v}_k\right)}{[4k^2-(2n-1)^2]}$$
$$+\frac{8}{\pi}\tilde{e}(\cos\delta)(-1)^n\sum_{k=1}^{N}\frac{(-1)^kk\left(\frac{d^2\tilde{w}_k}{d\tau^2}+2\tilde{\Omega}\frac{d\tilde{v}_k}{d\tau}-\tilde{\Omega}^2\tilde{w}_k\right)}{[4k^2-(2n-1)^2]} \tag{3.5f}$$
$$-\Lambda\left(\frac{4}{\pi}\right)\tilde{c}_{62}\tilde{\kappa}_1(2n-1)(\cos\gamma_n\tilde{b})\sum_{k=1}^{N}\left[(\cos k\pi\tilde{b})\left[k\pi\left(\tilde{v}_k+\tilde{d}_i\frac{d\tilde{v}_k}{d\tau}\right)-\left(\tilde{\alpha}_k+\tilde{d}_i\frac{d\tilde{\alpha}_k}{d\tau}\right)\right]\right]$$
$$-2\Lambda\tilde{c}_{66}(2n-1)(\cos\gamma_n\tilde{b})\sum_{k=1}^{N}\left[(2k-1)(\cos\gamma_k\tilde{b})\left(\tilde{\phi}_k+\tilde{d}_i\frac{d\tilde{\phi}_k}{d\tau}\right)\right]=0$$

where the nondimensional quantities are defined as

$$\tau = \frac{\pi}{2L}\sqrt{\frac{EA}{\mu}}\, t \tag{3.6a}$$

$$\tilde{u}_n = \frac{1}{L} u_n \ , \ \tilde{v}_n = \frac{1}{L} v_n \ , \ \tilde{w}_n = \frac{1}{L} w_n \tag{3.6b}$$

$$\tilde{\alpha}_n = \alpha_n \ , \ \tilde{\beta}_n = \beta_n \ , \ \tilde{\phi}_n = \phi_n \tag{3.6c}$$

$$\tilde{\kappa}_1 = \kappa_1 \frac{G}{E} \ , \ \tilde{\kappa}_2 = \kappa_2 \frac{G}{E} \ , \ \tilde{G} = \frac{G}{E} \tag{3.6d}$$

$$\tilde{\mu} = \frac{16gL}{\pi^3 EA}\mu \ , \ \tilde{J} = \frac{J}{AL^2} \tag{3.6e}$$

$$\tilde{c}_{11} = \frac{EA}{L} c_{11} \ , \ \tilde{c}_{51} = EA c_{51} \ , \ \tilde{c}_{15} = EA c_{15} \tag{3.6f}$$

$$\tilde{c}_{55} = EAL c_{55} \ , \ \tilde{c}_{22} = \frac{EA}{L} c_{22} \ , \ \tilde{c}_{33} = \frac{EA}{L} c_{33} \tag{3.6g}$$

$$\tilde{c}_{26} = \frac{GJ}{L^2} c_{26} \ , \ \tilde{c}_{62} = \frac{GJ}{L^2} c_{62} \ , \ \tilde{c}_{44} = EAL c_{44} \ , \ \tilde{c}_{66} = \frac{(GJ)^2}{EAL^3} c_{66} \tag{3.6h}$$

$$\tilde{\Omega} = \frac{2L}{\pi}\sqrt{\frac{\mu}{EA}}\,\Omega \tag{3.6i}$$

$$\tilde{e} = \frac{1}{L} e \ , \ \tilde{r}_1 = \frac{1}{L} r_1 \ , \ \tilde{r}_2 = \frac{1}{L} r_2 \ , \ \tilde{b} = \frac{1}{L} b \tag{3.6j}$$

$$\gamma_k = \theta_k L = \frac{2k-1}{2}\pi \tag{3.6k}$$

$$\tilde{d}_e = \frac{2L}{\pi}\sqrt{\frac{\mu}{EA}}\, d_e \ , \ \tilde{d}_i = \frac{\pi}{2L}\sqrt{\frac{EA}{\mu}}\, d_i \ , \ \tilde{d}_c = \frac{4}{\pi}\sqrt{\frac{\mu}{EA}}\, d_c \tag{3.6l}$$

Following the same logic as in Chapter 2, the crack is assumed to be either completely open or completely closed at a given time. This means that the above approximate equations of motion are linear within each period of time in which the crack remains open or closed. This "breathing" crack behavior requires a transition condition to determine when the value of Λ changes. For the shaft presented here, an open crack is identified as a condition in which the elongation of all of the points on the crack face is positive. Otherwise, the crack is considered closed. Thus, the transition condition is when the elongation mentioned above changes sign. Mathematically, in dimensional form, this can be written as (Wauer, b)

$$(u_x - h_2\beta_x)\big|_{x=b} \begin{cases} \geq 0 \text{ for an open crack} \\ < 0 \text{ for a closed crack} \end{cases} \tag{3.7}$$

where h_2 is the smaller of the radii of an oval cross-section (see Figure 3.1(b)) and the subscript x represents a partial derivative with respect to the axial coordinate. In the solution of the nondimensional equations, an L/R ratio (length/radius) is needed. If this ratio is prescribed using the value of h_2 (see Figure 3.1(b)) for R, then the nondimensional $\tilde{h}_2$ can be defined as $\tilde{h}_2 = R/L$. Therefore, the nondimensional form of the transition condition (3.7), in terms of the approximate solutions for $u(x, t)$ and $\beta(x, t)$, is

$$\sum_{k=1}^{N} [\tilde{u}_k(\tau)\gamma_k(\cos\gamma_k\tilde{b}) + (\frac{R}{L})\tilde{\beta}_k(\tau)(k\pi)(\sin k\pi\tilde{b})] \begin{cases} \geq 0 \text{ for an open crack} \\ < 0 \text{ for a closed crack} \end{cases} \tag{3.8}$$

Many investigators, such as Mayes and Davies (1980) and Bachschmid et al. (1984), comment that the breathing crack behavior for shafts depends on shaft weight and unbalance. These factors are accounted for in the equations of motion by the $\tilde{\mu}$ and $\tilde{e}$ terms and therefore are accounted for in the transition condition.

3.3 Shaft Parameters

As discussed in Chapter 2, the presence of a crack will decrease the stiffness of the shaft. As the crack depth increases, the stiffness will decrease further. Since this thesis focuses on compliance (which is the inverse of the stiffness), the compliance of the cracked section will increase for larger crack depths. However, unlike the longitudinal case, the change in $\tilde{c}_{11}$ alone does not reflect the total change in stiffness characteristics of the shaft. Now that we are considering transverse and torsional displacements, more crack compliances are necessary to fully describe the resulting cracked shaft behavior. In fact, a 6×6 compliance matrix is needed, and the appropriate terms show up in equations (3.2a-f). Table 3.1 presents the 3 sets of crack depth ratios considered here and the corresponding values of the elements in the nondimensional compliance matrix. The notation a/D (= crack depth/shaft diameter) is that used by Papadopoulos and Dimarogonas (1987) for the circular shaft which they consider. The values from their paper have been nondimensionalized according to the notation used here and are functions of the L/R ratio previously described in conjunction with the transition condition. In the conversion of their nondimensional compliances, it is assumed that Poisson's ratio, ν, is equal to 0.3. Due to differences in the nondimensionalization procedure between this chapter and Chapter 2, the value of $\tilde{c}_{11}$ used for the shaft is one-half the value used for the bar of Chapter 2.

As in Chapter 2, it is convenient to define a set of standard parameters. In this chapter, primary attention is given to a circular shaft. The standard case to be investigated uses the following set of parameters:

$a/D = 0.2$

$L/R = 10$

$L = 5$ feet

Table 3.1. Values of compliance used for the rotating shaft

COMPLIANCE	a/D = 0.1	a/D = 0.2	a/D = 0.3
$\bar{c}_{11}$	$0.024\frac{R}{L}$	$0.170\frac{R}{L}$	$0.555\frac{R}{L}$
$\bar{c}_{22}$	$0.020\frac{R}{L}$	$0.114\frac{R}{L}$	$0.346\frac{R}{L}$
$\bar{c}_{33}$	$0.024\frac{R}{L}$	$0.160\frac{R}{L}$	$0.434\frac{R}{L}$
$\bar{c}_{44}$	$0.091\frac{L}{R}$	$0.190\frac{L}{R}$	$0.689\frac{L}{R}$
$\bar{c}_{55}$	$0.385\frac{L}{R}$	$2.550\frac{L}{R}$	$6.890\frac{L}{R}$
$\bar{c}_{66}$	$0.00034\frac{R^3}{L^3}$	$0.0040\frac{R^3}{L^3}$	$0.0136\frac{R^3}{L^3}$
$\bar{c}_{15} = \bar{c}_{51}$	0.091	0.740	2.090
$\bar{c}_{26} = \bar{c}_{62}$	$0.0072\frac{R^2}{L^2}$	$0.0600\frac{R^2}{L^2}$	$0.1330\frac{R^2}{L^2}$
NOTE: Values based on information from Papadopoulos and Dimarogonas, 1987			

$\tilde{r}_1 = \tilde{r}_2 = 0.05$

$\tilde{\kappa}_1 = \tilde{\kappa}_2 = 0.886\tilde{G}$

$\tilde{b} = 0.4$

$\tilde{e} = 0.01$

$\tilde{d}_c = 0.01$

$\tilde{d}_e = \tilde{d}_i = 0.1$

$\gamma = \delta = 0$

An L/R ratio of 10 is used to justify the use of equations (3.1) which model shear effects.

Some attention is given to an elliptical section with a radius ratio of 1.5. This changes the shape coefficients and the radii of gyration shown above to the following values:

$\tilde{r}_1 = 0.075$, $\tilde{r}_2 = 0.05$

$\tilde{\kappa}_1 = 0.90151\tilde{G}$, $\tilde{\kappa}_2 = 0.85877\tilde{G}$

The values for the dimensional shear coefficients are the same as used by Cowper (1966) with $\nu = 0.3$. Unless otherwise stated, all displacements are measured at $x/L = 0.7$.

3.4 Natural Frequencies of an Uncracked, Undamped Shaft

In order to get an idea of how the model behaves, an investigation of the natural frequencies of an uncracked, undamped shaft seems warranted. To this end, in the approximate equations (3.5a-f),

all $\tilde{c}_{ij}$ values are set to zero and the three damping coefficients $\tilde{d}_c$, $\tilde{d}_e$, and $\tilde{d}_i$ are also set to zero. This removes the crack and damping effects. Also, to remove the forcing of the system due to gravity and unbalance, $\tilde{\mu}$ and $\tilde{e}$ are set to zero. Next, to obtain a two-term approximation, N = 2 is used in equations (3.5a-f). By doing the above, the differential equations uncouple in sets. The equations for $\tilde{u}_n(x, \tau)$ and $\tilde{\phi}_n(x, \tau)$ become independent and have the form

$$\frac{d^2\tilde{u}_1}{d\tau^2} + \tilde{u}_1 = 0 \tag{3.9a}$$

$$\frac{d^2\tilde{u}_2}{d\tau^2} + 9\tilde{u}_2 = 0 \tag{3.9b}$$

$$(\tilde{r}_1^2 + \tilde{r}_2^2)\frac{d^2\tilde{\phi}_1}{d\tau^2} + \tilde{G}\tilde{J}\tilde{\phi}_1 = 0 \tag{3.10a}$$

$$(\tilde{r}_1^2 + \tilde{r}_2^2)\frac{d^2\tilde{\phi}_2}{d\tau^2} + 9\tilde{G}\tilde{J}\tilde{\phi}_2 = 0 \tag{3.10b}$$

where the subscripts on $\tilde{u}$ and $\tilde{\phi}$ represent the appropriate "mode" value. The term "mode" is not strictly correct for this nonlinear problem, as explained in Chapter 2, but will be used here for simplicity of explanation. The equations for $\tilde{v}_n(x, \tau)$, $\tilde{w}_n(x, \tau)$, $\tilde{\alpha}_n(x, \tau)$, and $\tilde{\beta}_n(x, \tau)$ remain coupled for each individual n value (n = 1,2). To facilitate presentation, and looking forward to the computation of natural frequencies, the reduced differential equations are not presented. Instead, the substitution

$$\begin{bmatrix} \tilde{v}_n \\ \tilde{w}_n \\ \tilde{\alpha}_n \\ \tilde{\beta}_n \end{bmatrix} = \begin{bmatrix} \tilde{V}_n \\ \tilde{W}_n \\ \tilde{A}_n \\ \tilde{B}_n \end{bmatrix} e^{i\tilde{\omega}\tau} \tag{3.11}$$

is made in the coupled sets of equations of motion. Then, for the first mode (n = 1), the equations of motion can be represented as the eigenvalue problem

$$\begin{bmatrix} g_{11} & g_{12} & g_{13} & g_{14} \\ g_{21} & g_{22} & g_{23} & g_{24} \\ g_{31} & g_{32} & g_{33} & g_{34} \\ g_{41} & g_{42} & g_{43} & g_{44} \end{bmatrix} \begin{bmatrix} \tilde{V}_1 \\ \tilde{W}_1 \\ \tilde{A}_1 \\ \tilde{B}_1 \end{bmatrix} = \begin{bmatrix} 0 \\ 0 \\ 0 \\ 0 \end{bmatrix} \tag{3.12}$$

where

$$g_{11} = -\tilde{\omega}^2 - \tilde{\Omega}^2 + 4\tilde{\kappa}_1 \tag{3.13a}$$

$$g_{12} = -2\tilde{\Omega}\tilde{\omega}i = -g_{21} \tag{3.13b}$$

$$g_{13} = g_{31} = -\frac{4}{\pi}\tilde{\kappa}_1 \tag{3.13c}$$

$$g_{14} = g_{41} = g_{23} = g_{32} = g_{34} = g_{43} = 0 \tag{3.13d}$$

$$g_{22} = -\tilde{\omega}^2 - \tilde{\Omega}^2 + 4\tilde{\kappa}_2 \tag{3.13e}$$

$$g_{24} = g_{42} = \frac{4}{\pi}\tilde{\kappa}_2 \tag{3.13f}$$

$$g_{33} = -\tilde{r}_1^2\tilde{\omega}^2 + \tilde{r}_1^2\tilde{\Omega}^2 + 4\tilde{r}_1^2 + \frac{4}{\pi^2}\tilde{\kappa}_1 \tag{3.13g}$$

$$g_{44} = -\tilde{r}_2^2\tilde{\omega}^2 + \tilde{r}_2^2\tilde{\Omega}^2 + 4\tilde{r}_2^2 + \frac{4}{\pi^2}\tilde{\kappa}_2 \tag{3.13h}$$

Similarly, for the second mode (n = 2), the eigenvalue problem becomes

$$\begin{bmatrix} h_{11} & h_{12} & h_{13} & h_{14} \\ h_{21} & h_{22} & h_{23} & h_{24} \\ h_{31} & h_{32} & h_{33} & h_{34} \\ h_{41} & h_{42} & h_{43} & h_{44} \end{bmatrix} \begin{bmatrix} \tilde{V}_2 \\ \tilde{W}_2 \\ \tilde{A}_2 \\ \tilde{B}_2 \end{bmatrix} = \begin{bmatrix} 0 \\ 0 \\ 0 \\ 0 \end{bmatrix} \tag{3.14}$$

where

$$h_{11} = -\tilde{\omega}^2 - \tilde{\Omega}^2 + 16\tilde{\kappa}_1 \tag{3.15a}$$

$$h_{12} = -2\tilde{\Omega}\tilde{\omega}i = -h_{21} \tag{3.15b}$$

$$h_{13} = h_{31} = -\frac{8}{\pi}\tilde{\kappa}_1 \tag{3.15c}$$

$$h_{14} = h_{41} = h_{23} = h_{32} = h_{34} = h_{43} = 0 \tag{3.15d}$$

$$h_{22} = -\tilde{\omega}^2 - \tilde{\Omega}^2 + 16\tilde{\kappa}_2 \tag{3.15e}$$

$$h_{24} = h_{42} = \frac{8}{\pi}\tilde{\kappa}_2 \tag{3.15f}$$

$$h_{33} = -\tilde{r}_1^2\tilde{\omega}^2 + \tilde{r}_1^2\tilde{\Omega}^2 + 16\tilde{r}_1^2 + \frac{4}{\pi^2}\tilde{\kappa}_1 \tag{3.15g}$$

$$h_{44} = -\tilde{r}_2^2\tilde{\omega}^2 + \tilde{r}_2^2\tilde{\Omega}^2 + 16\tilde{r}_2^2 + \frac{4}{\pi^2}\tilde{\kappa}_2 \tag{3.15h}$$

Note that $g_{12} \neq g_{21}$ and $h_{12} \neq h_{21}$, which creates nonsymmetry in the respective matrices. This nonsymmetry is caused by the gyroscopic effects taken into account in the mathematical model.

For equations (3.9a-b) and (3.10a-b), the natural frequencies of vibration can easily be obtained. The values of $\tilde{\omega}_1$ and $\tilde{\omega}_2$ for $\tilde{\phi}$ are functions of $\tilde{G}$, where from (3.6d),

$$\tilde{G} = \frac{G}{E} = \frac{1}{2(1+\nu)} = \frac{1}{2.6} \text{ for } \nu = 0.3 \tag{3.16}$$

For a circular section, the torsional constant $\tilde{J}$ equals $\tilde{r}_1^2 + \tilde{r}_2^2$, so that these terms cancel in equations (3.10a-b). Therefore, for a circle, the natural frequencies for $\tilde{u}$ are $\tilde{\omega}_1 = 1$ and $\tilde{\omega}_2 = 3$ while for $\tilde{\phi}$ they are $\tilde{\omega}_1 = 0.620$ and $\tilde{\omega}_2 = 1.86$. For an elliptical section, the natural frequencies for $\tilde{u}$ are unchanged. However, the value of $\tilde{J}$ is no longer $\tilde{r}_1^2 + \tilde{r}_2^2$. Using the standard values of Section 3.3, the natural frequencies for $\tilde{\phi}$ for an elliptical section are $\tilde{\omega}_1 = 0.572$ and $\tilde{\omega}_2 = 1.72$. Note that for both a circle and an ellipse, the natural frequencies are independent of the angular frequency, $\tilde{\Omega}$.

To obtain the natural frequencies for $\tilde{v}$, $\tilde{w}$, $\tilde{\alpha}$, and $\tilde{\beta}$, the matrices of equations (3.12) and (3.14) must be expanded. The resulting characteristic equation is a function of the cross-section and the angular frequency. Using the IMSL subroutine DZREAL to evaluate the roots of the characteristic equation for various values of $\tilde{\Omega}$, the plots of Figures 3.2 and 3.3 result for a circular and an elliptical section, respectively. Standard case parameters are used. In Figures 3.2(b) and 3.3(b), the portions of the graph near the origin are enlarged in order to more clearly see the behavior. In Figure 3.2, each curve touches the horizontal axis once, whereas in Figure 3.3 each curve intersects the horizontal axis twice. For a circular section, $\tilde{\kappa}_1 = \tilde{\kappa}_2$ and $\tilde{r}_1 = \tilde{r}_2$, which results in only four distinct eigenvalues (two for each mode) at $\tilde{\Omega} = 0$. However, for the ellipse, $\tilde{\kappa}_1$ is not equal to $\tilde{\kappa}_2$ and $\tilde{r}_1$ is not equal to $\tilde{r}_2$, which creates eight distinct eigenvalues (four for each mode). These eigenvalues, for $\tilde{\Omega} = 0$, are tabulated in Table 3.2 for both a circle and an ellipse.

Also presented in Table 3.2 are the critical speeds for the circle and ellipse. For our mathematical model, the critical speeds are those speeds at which the natural frequencies are zero, which correspond to the intersection points or tangential points of the curves with the vertical axis. Mathematically, at these speeds, the motion initially grows exponentially. In a physical situation, damping prevents unbounded motion and the critical speed is "..the rotational speed at which the maximum transverse vibrations occur during steady-state motion." (Reiff, 1979). Again, as with the natural frequencies, there are more critical speeds for an ellipse than there are for a circle.

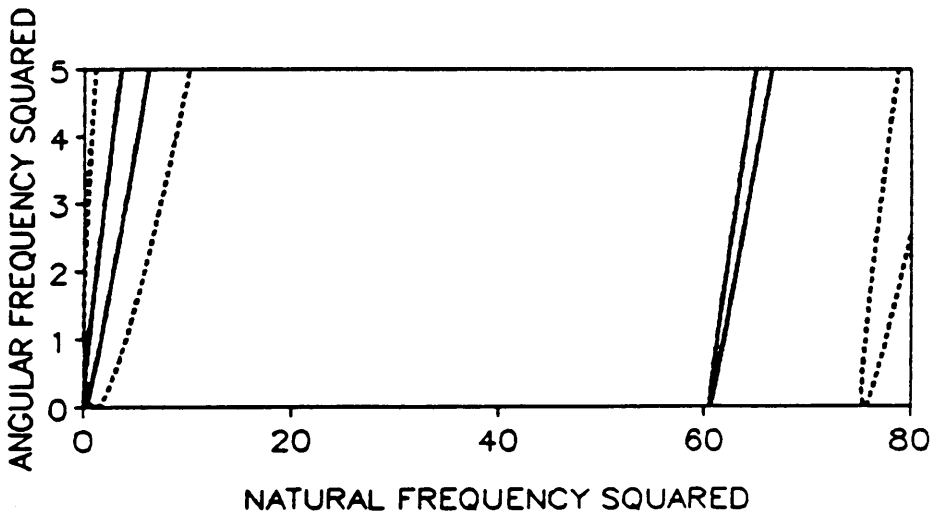

(a)

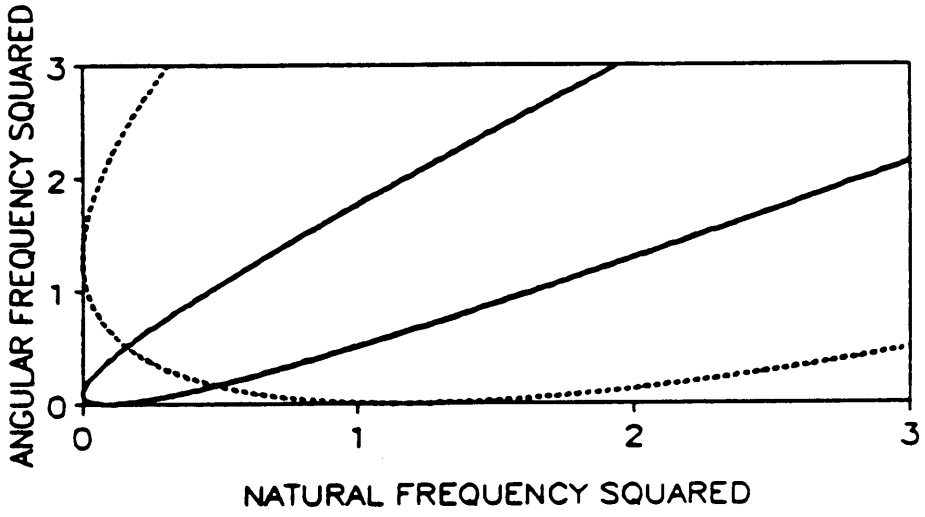

(b)

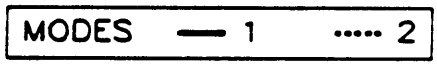

Figure 3.2. **Roots of characteristic equation for a circular section:** (a) Complete plot; (b) Enlarged view of the graph near the origin. Note that each curve touches the horizontal axis only once. Also, each of the two leftmost curves touches the vertical axis only once.

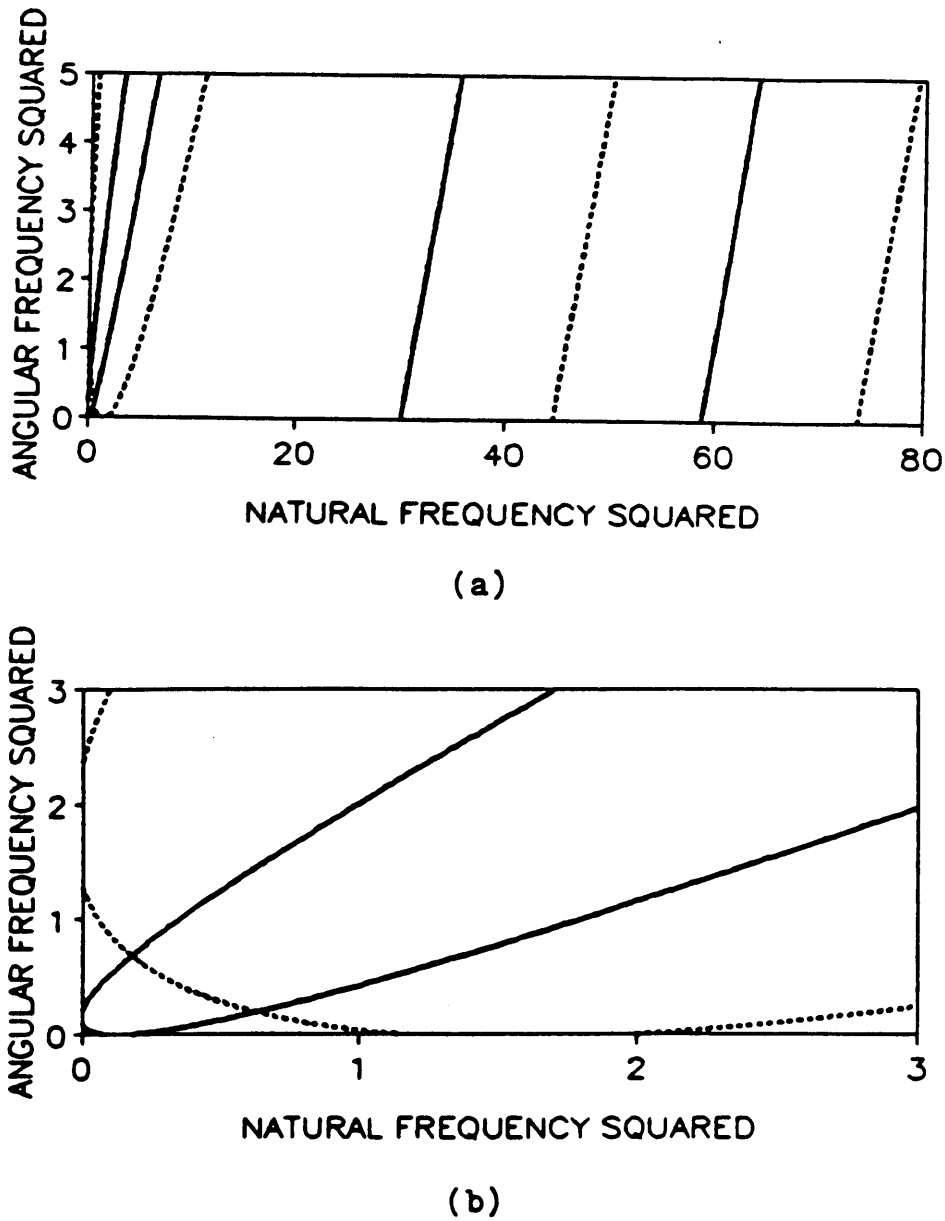

Figure 3.3. **Roots of characteristic equation for an elliptical section:** (a) Complete plot; (b) Enlarged view of the graph near the origin. Note that each curve intersects the horizontal axis twice. Also, each of the two leftmost curves touches the vertical axis twice.

Table 3.2. Critical speeds and natural frequencies (uncracked shaft)

CIRCLE				
	$\tilde{\Omega}^2 = 0$		$\tilde{\omega}^2 = 0$	
	$\tilde{\omega}^2$	$\tilde{\omega}$	$\tilde{\Omega}^2$	$\tilde{\Omega}$
MODE 1	0.060	0.245	0.094	0.307
	60.5	7.78		
MODE 2	1.18	1.09	1.30	1.14
	75.5	8.69		
ELLIPSE				
	$\tilde{\Omega}^2 = 0$		$\tilde{\omega}^2 = 0$	
	$\tilde{\omega}^2$	$\tilde{\omega}$	$\tilde{\Omega}^2$	$\tilde{\Omega}$
MODE 1	0.060	0.245	0.094	0.307
	0.179	0.423	0.200	0.447
	30.3	5.50		
	58.8	7.67		
MODE 2	1.16	1.08	1.29	1.14
	1.99	1.41	2.35	1.53
	44.7	6.69		
	73.7	8.58		

The lowest critical speed is significant for two reasons. First, most shafts operate at angular speeds below this critical speed. Secondly, if the operating speed is above this value, the presence of a crack may have little effect on the vibrational behavior (Henry and Okah-Avae, 1976). Grabowski (1980) and others have also noted the importance of the relationship between the running speed and the critical speed in crack detection. As a result of the above-stated facts, in the upcoming analysis of a cracked circular shaft, the operating speed will be chosen as $\tilde{\Omega} = 0.2$, which is approximately 65% of the lowest value tabulated in Table 3.2. The corresponding natural frequencies for $\tilde{v}$, $\tilde{w}$, $\tilde{\alpha}$, and $\tilde{\beta}$ (for the uncracked shaft) are tabulated in Table 3.3.

3.5 Solution

Due to the complexity of the equations, closed-form solutions are not practical, so that numerical integration is used exclusively. The IMSL subroutine DIVPAG is applied in all of the results to follow. The same basic program (as used in Chapter 2) is used in this chapter. The major modification is that the program now integrates twenty-four equations instead of four.

3.6 Cracked Shaft Behavior with No Mass Eccentricity

In this section, the value of $\tilde{e}$ will be set to zero in equations (3.5a-f), which means that these equations of motion now model a shaft in which the mass center and the geometric center coincide. For simplicity, only circular sections are investigated. Standard case parameters are used unless otherwise stated.

Equations (3.5a-f), in their most general form, reveal that the vibration of the shaft is a forced vibration problem since the terms involving $\tilde{e}$ and $\tilde{\mu}$ alone (i.e., terms in which neither a displacement nor its derivative is present) act as forcing functions. For $\tilde{e} = 0$, the forcing is reduced to that caused

Table 3.3. Natural frequencies (uncracked shaft) at $\tilde{\Omega} = 0.2$

CIRCLE		
	$\tilde{\Omega}^2 = 0.04$	
	$\tilde{\omega}^2$	$\tilde{\omega}$
MODE 1	0.011	0.105
	0.246	0.496
	60.5	7.78
	60.6	7.79
MODE 2	0.785	0.886
	1.60	1.26
	75.4	8.68
	75.8	8.71

by gravity. However, as it turns out, $\tilde{\mu}$ is so small that it contributes little to the response. To illustrate, for L = 5 feet, using a steel shaft, $\tilde{\mu} \simeq 2.99 \times 10^{-7}$. Therefore, since $\tilde{\mu}$ is so small, the problem is essentially a free vibration problem.

Three cases of initial conditions are considered in the results to follow; they are the initial conditions on the nondimensional functions of τ, not on the complete functions of x and t. For the two-term approximation, these initial conditions can be written as

CASE A: all first-mode displacements = 0.10

all second-mode displacements = 0.01

CASE B: all first-mode displacements = 0.05

all second-mode displacements = 0.05

CASE C: all first-mode displacements = 0.01

all second-mode displacements = 0.10

In all cases, the initial velocities of both modes are set to zero. As discussed in Chapter 2, for free vibration, the influence of the initial conditions can be significant, and using the above cases may indicate the relative importance of each mode to the overall motion.

Figures 3.4 through 3.7 compare the influence of the three cases of initial conditions on the four displacements which are readily measurable in a physical situation, namely deflections in the axial, horizontal, and vertical directions and the torsional displacement. These will be identified as $\tilde{X}$, $\tilde{Y}$, $\tilde{Z}$, and $\tilde{\phi}$, respectively. The $\tilde{Y}$ and $\tilde{Z}$ displacements (in the fixed coordinate system) are functions of the $\tilde{v}$ and $\tilde{w}$ displacements (in the rotating coordinate system) and are defined as

$$\tilde{Y} = \tilde{v}(x, \tau)\cos(\tilde{\Omega}\tau) - \tilde{w}(x, \tau)\sin(\tilde{\Omega}\tau) \tag{3.17a}$$

$$\tilde{Z} = \tilde{v}(x, \tau)\sin(\tilde{\Omega}\tau) + \tilde{w}(x, \tau)\cos(\tilde{\Omega}\tau) \tag{3.17b}$$

Figures 3.4, 3.5, 3.6, and 3.7 pertain to the undamped motion of $\tilde{X}$, $\tilde{Z}$, $\tilde{Y}$, and $\tilde{\phi}$, respectively. The shaft is cracked at $\tilde{b} = 0.4$. In each figure (and in subsequent figures), the thicker portions of each curve denote the periods in which the crack is open. It is observed that as the second mode is stimulated more, its participation becomes apparent by the frequency of motion. Note the similarity in Figures 3.4 and 3.7, which are for $\tilde{X}$ and $\tilde{\phi}$, respectively. This similarity results from the similarity of equations (3.5a) and (3.5f) (for a circular shaft) for $\tilde{e} = 0$ and $\tilde{\mu} = 0$, as shown in Section 3.4. Figure 3.8 shows a comparison of the corresponding spectra for Figure 3.4. (As discussed in Chapter 2, a conversion factor is needed to relate the spectral response to an amplitude of motion, and this factor is given in all figure captions where spectra are presented.). Note that the governing frequencies are near 1 and 3. This agrees with the results of Section 3.4 where it was shown that 1 and 3 are the natural frequencies of $\tilde{X}$ ($= \tilde{u}$) for an uncracked shaft. The frequencies for the cracked shaft are lower than those for the uncracked shaft, as expected, since the crack reduces the stiffness of the shaft.

Figure 3.9 presents the time histories for $\tilde{\alpha}$ and $\tilde{\beta}$ for Case A initial conditions. All other parameters are as discussed earlier. Since these displacements are typically not of interest (and are difficult to measure), they will not be shown in the upcoming figures. They are presented in Figure 3.9 only to give an indication of their general behavior.

Since one of the goals of this thesis is to study how cracks can be detected, a comparison of the behaviors of cracked shafts and uncracked shafts is necessary. Figures 3.10 through 3.13 provide this comparison for the undamped case. In each figure, the top row of graphs pertains to the uncracked shaft and the bottom row applies to the cracked shaft (a/D = 0.2). In each row, a time history plot and its corresponding spectrum are shown. In all four figures, Case A initial conditions

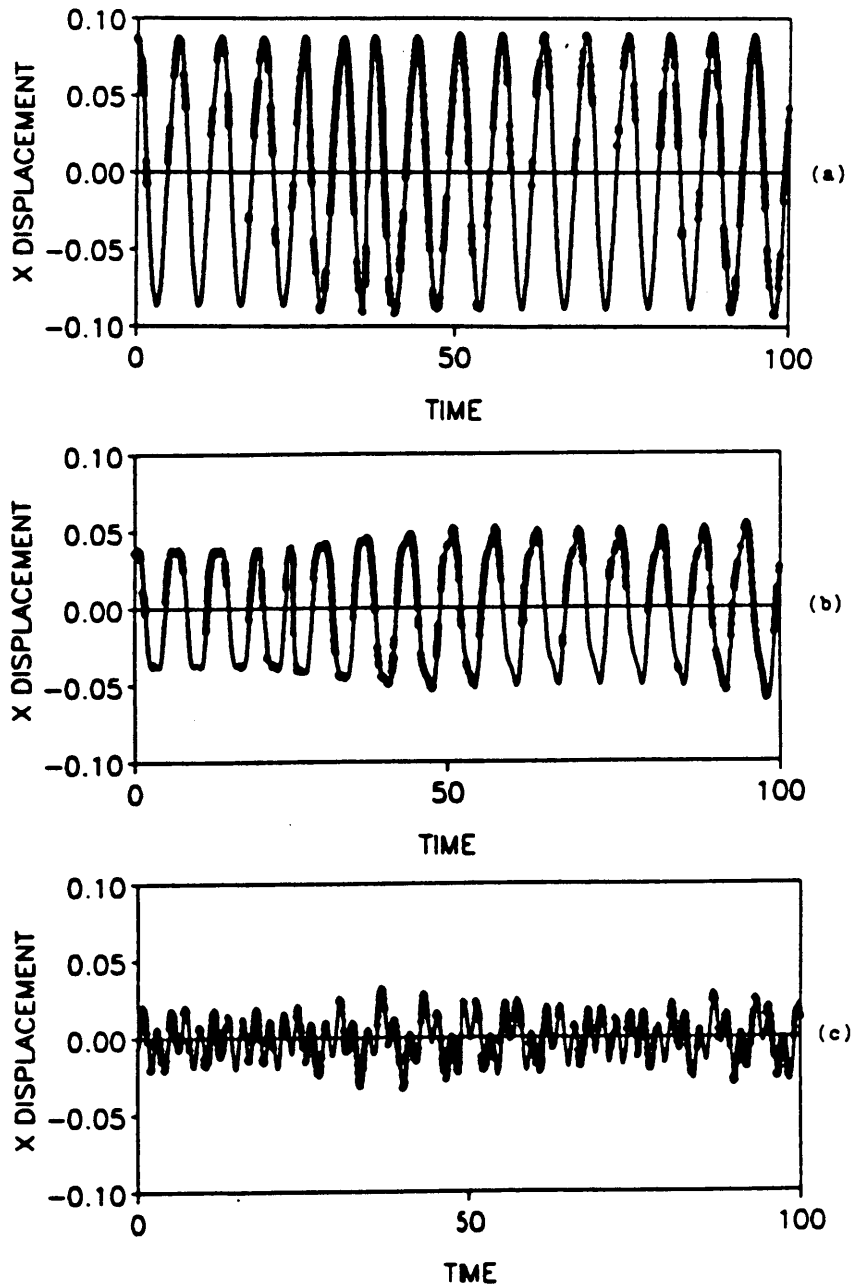

Figure 3.4. Time histories for $\tilde{X}$: (a) Case A initial conditions; (b) Case B initial conditions; (c) Case C initial conditions.

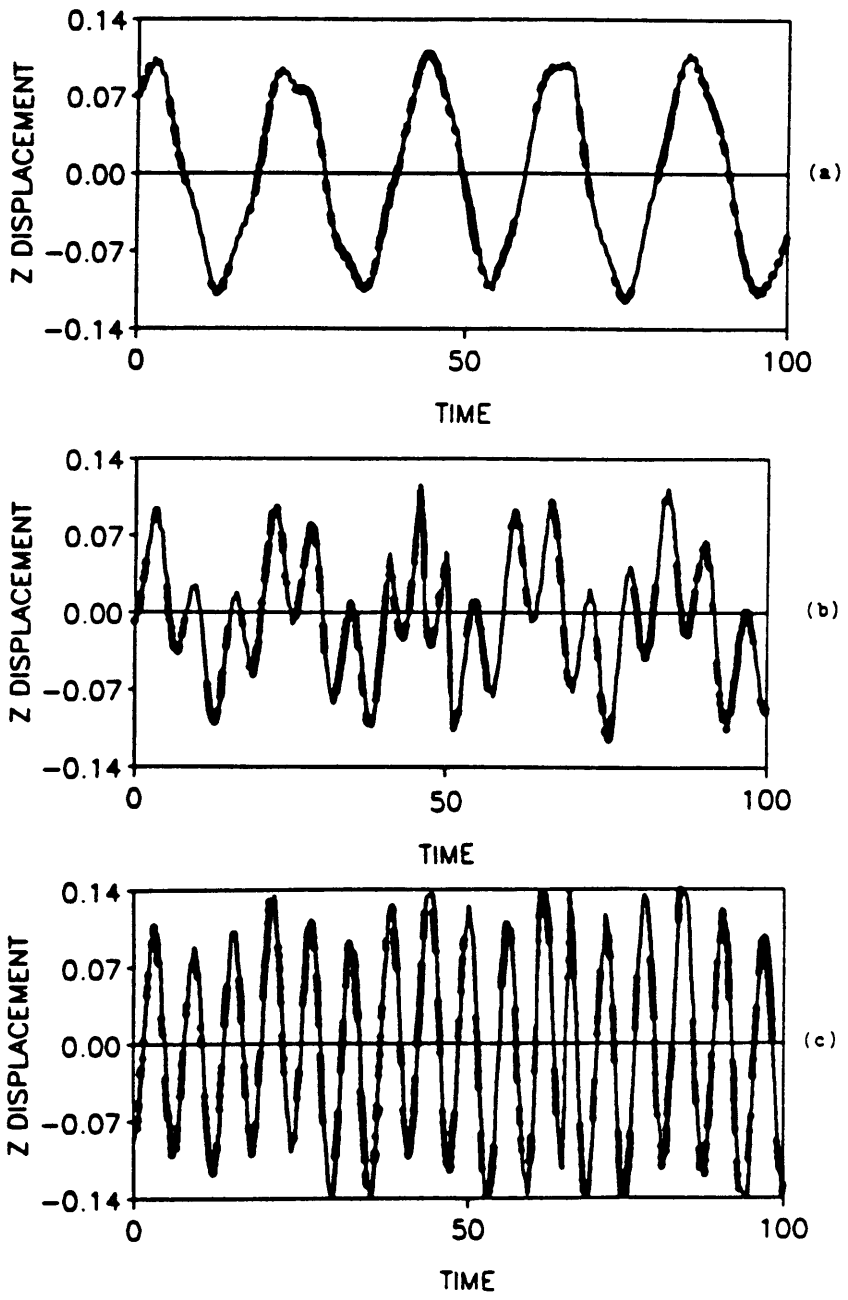

Figure 3.5. Time histories for $\tilde{Z}$: (a) Case A initial conditions; (b) Case B initial conditions; (c) Case C initial conditions.

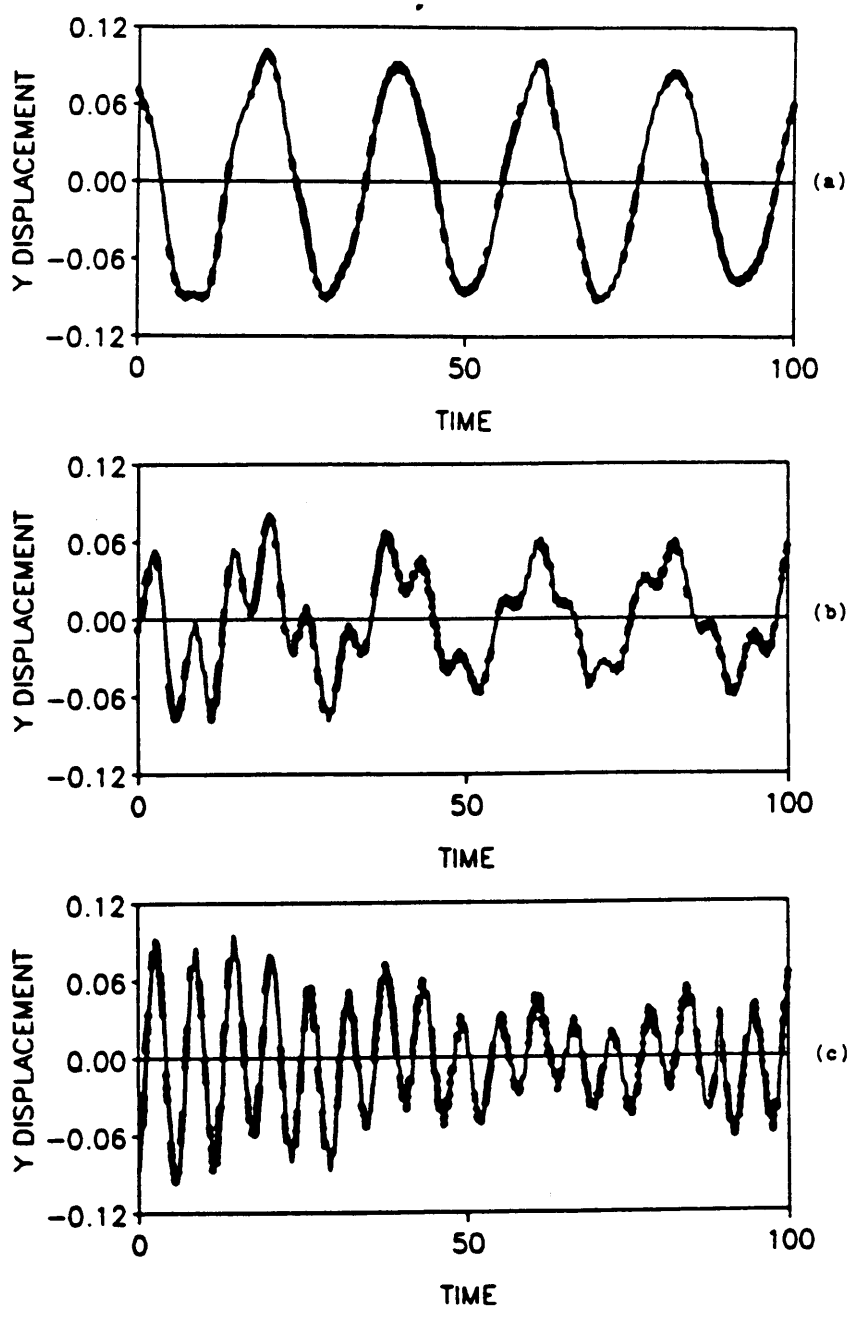

Figure 3.6. Time histories for $\tilde{Y}$: (a) Case A initial conditions; (b) Case B initial conditions; (c) Case C initial conditions.

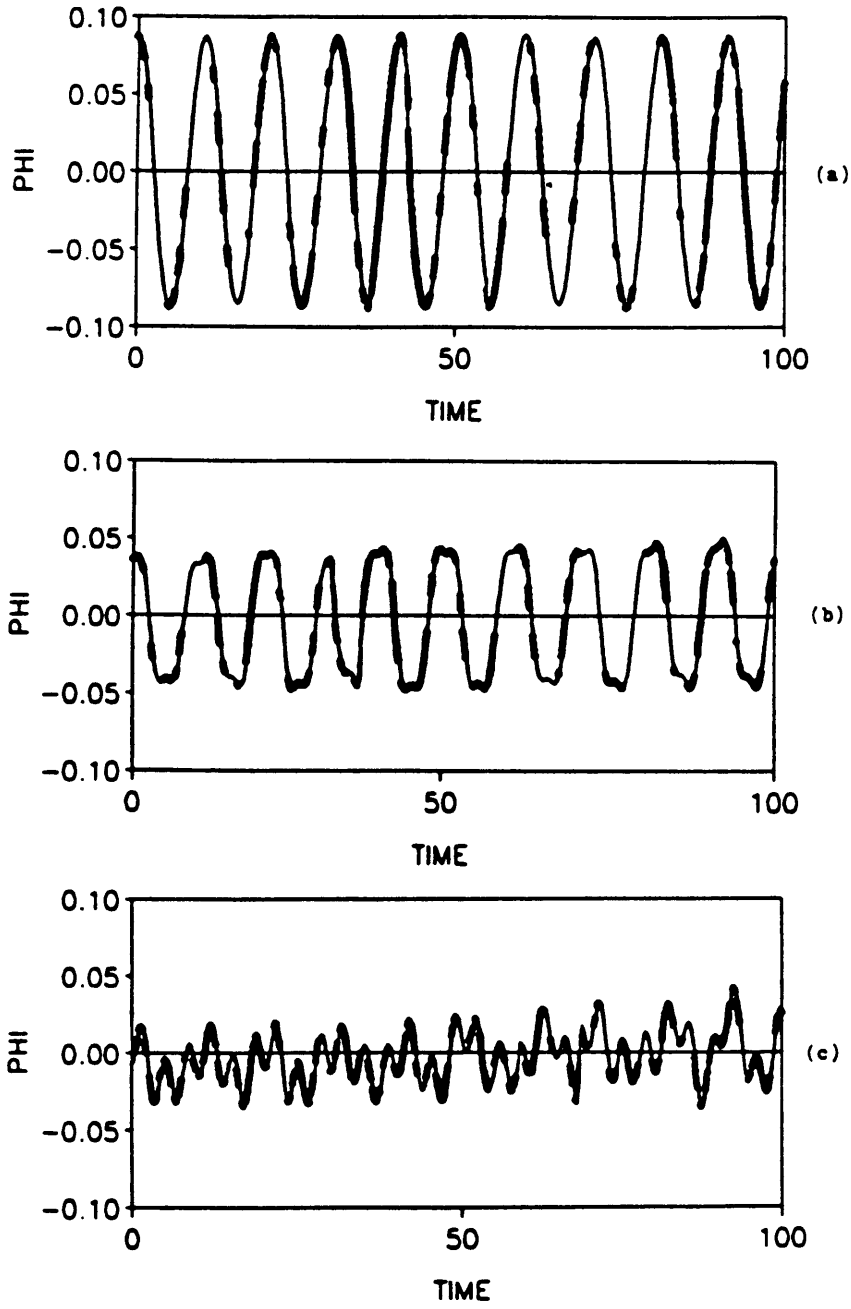

Figure 3.7. Time histories for $\tilde{\phi}$: (a) Case A initial conditions; (b) Case B initial conditions; (c) Case C initial conditions.

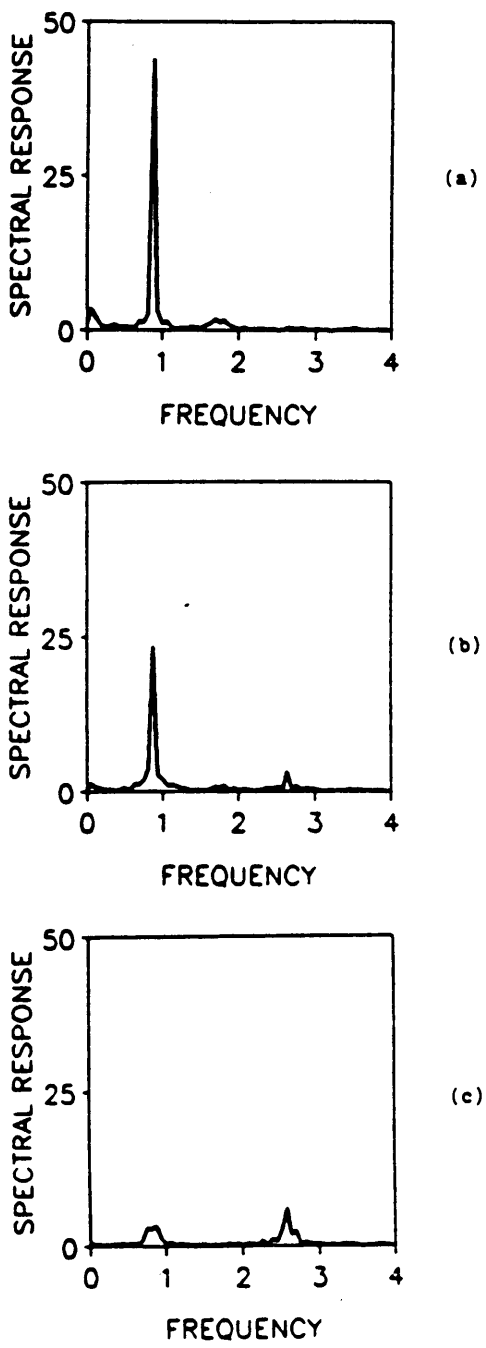

Figure 3.8. Spectra for the time histories of Figure 3.4: (a) Case A initial conditions; (b) Case B initial conditions; (c) Case C initial conditions. Spectral response scale factor = 1/500.

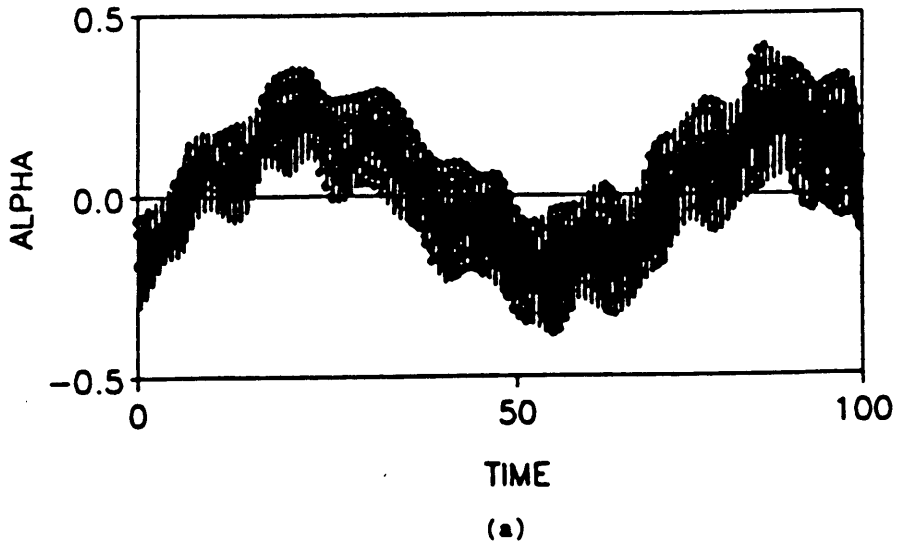

(a)

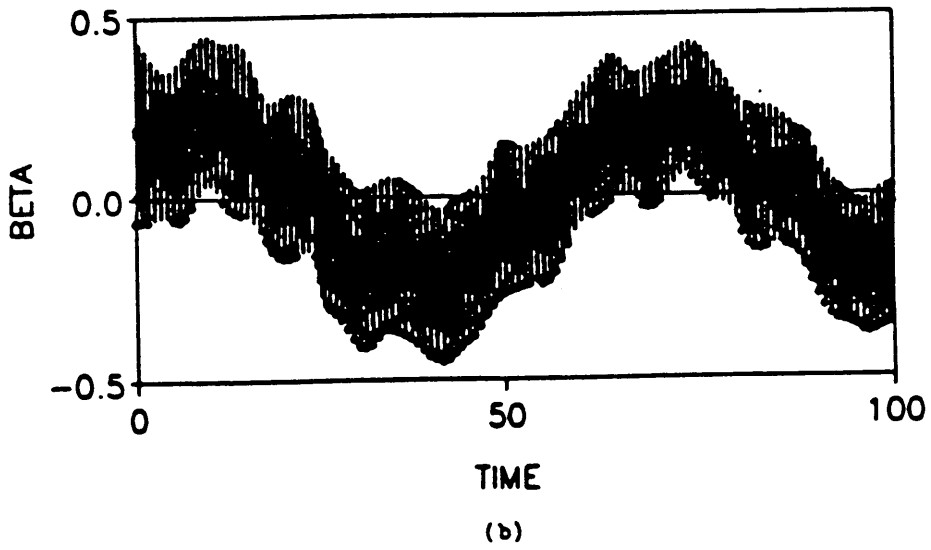

(b)

Figure 3.9. Time histories for $\tilde{\alpha}$ and $\tilde{\beta}$ for Case A initial conditions: (a) $\tilde{\alpha}$ vs. τ; (b) $\tilde{\beta}$ vs. τ.

are used. To achieve the uncracked shaft model from equations (3.5a-f), all $\tilde{c}_{ij}$ are set to zero and $\tilde{d}_c$ is set to zero. The time histories and spectra are virtually identical for the cracked and uncracked shafts. This agrees with the results of Chapter 2 for the free vibration behavior of cracked bars. Clearly, for the small crack depths considered here, observing the free vibration behavior does not provide a good means by which cracks can be detected.

So far, this section has focused on the undamped free vibration of the shaft. Figure 3.14 illustrates why damping has not been discussed. In Figure 3.14, the standard case values for damping are used, initial conditions are those of Case C, and a crack is present at $\tilde{b} = 0.4$. Since there is little forcing present due to $\tilde{\mu}$ when $\tilde{e} = 0$, the motion simply dies out due to damping and one does not see any significant effect of the crack.

3.7 Cracked Shaft Behavior with Mass Eccentricity

When $\tilde{e}$ is not equal to zero, the equations of motion are coupled together much more than for $\tilde{e} = 0$. In particular, the equation for $\tilde{\phi}$ becomes more complex since acceleration terms for $\tilde{v}$ and $\tilde{w}$ enter into the formulation. Also, the equations reflect that the shaft is now being forced by the mass unbalance created by a nonzero $\tilde{e}$.

Figures 3.15 and 3.16 represent the behavior of a cracked shaft (standard case) undergoing undamped vibration with $\tilde{e} = 0.01$. Figure 3.15 provides time history plots and spectra for $\tilde{X}$ and $\tilde{Z}$, while Figure 3.16 provides the corresponding results for $\tilde{Y}$ and $\tilde{\phi}$. By comparing Figure 3.15 with Figures 3.10(c) and (d) and 3.11(c) and (d), it is obvious that the eccentricity does not have a major influence on these motions. Similarly, by comparing Figure 3.16(a) and (b) with Figure 3.12(c) and (d), one also notices little change. However, the $\tilde{\phi}$ graphs in Figure 3.16(c) and (d) are drastically different from those in Figure 3.13(c) and (d) corresponding to a cracked shaft without eccentricity. This change is the result of the added terms in the $\tilde{\phi}$ equation, as discussed earlier. The eccentricity

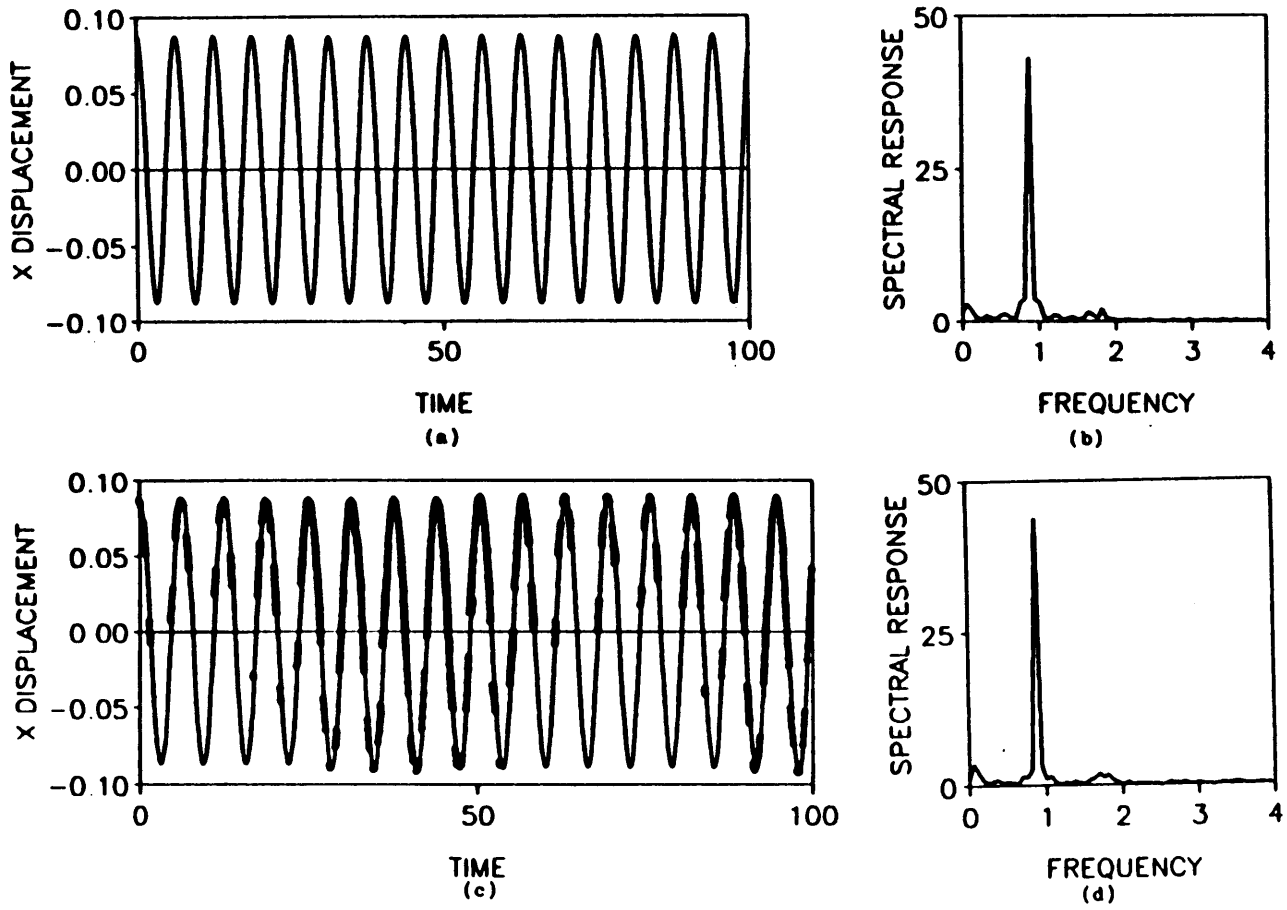

Figure 3.10. Comparison of uncracked and cracked shafts (free vibration, Case A) - $\tilde{X}$: (a) Uncracked shaft time history; (b) Spectrum for (a); (c) Cracked shaft time history; (d) Spectrum for (c). Spectral response scale factor = 1/500.

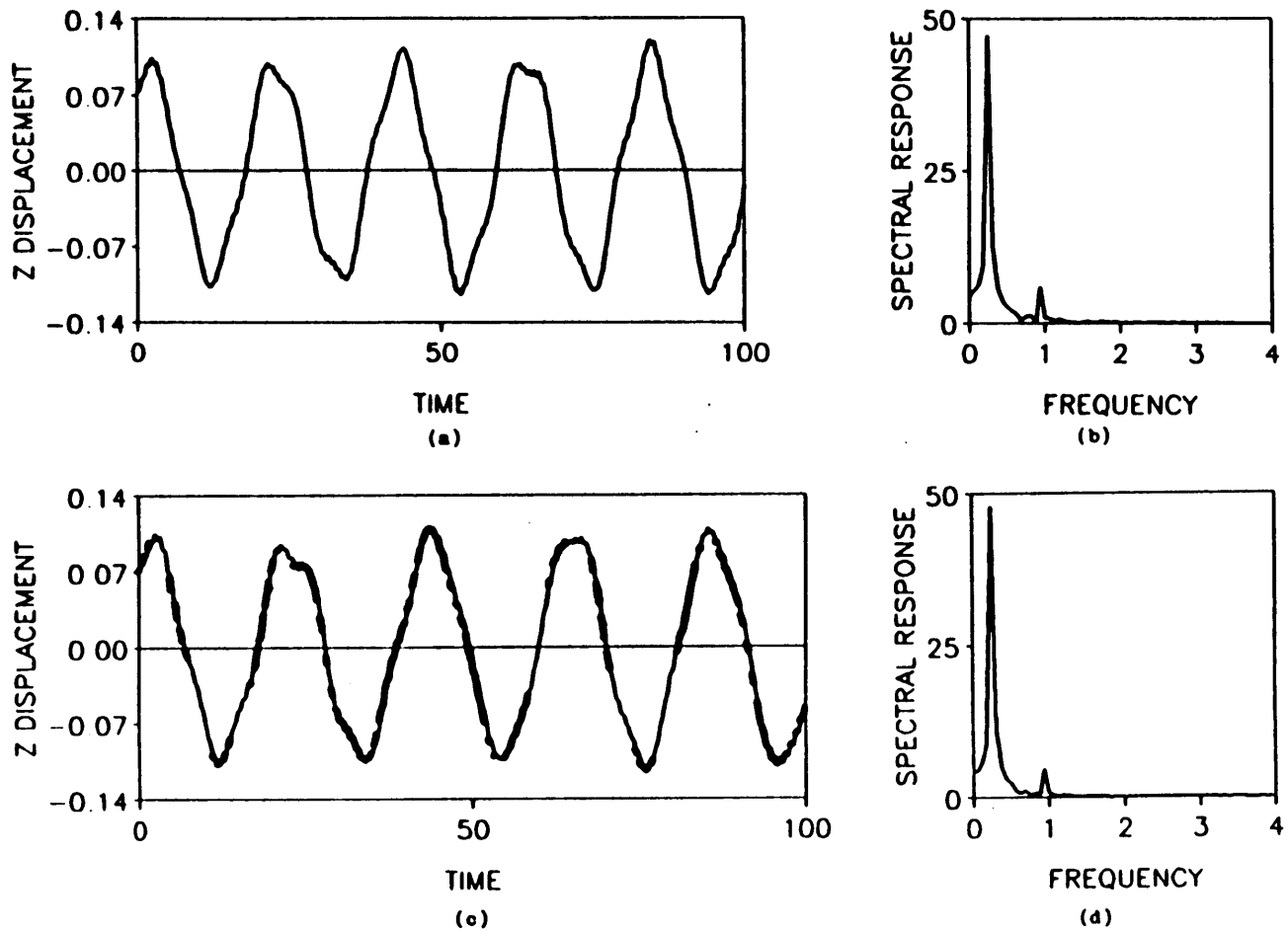

Figure 3.11. Comparison of uncracked and cracked shafts (free vibration, Case A) - $\tilde{Z}$: (a) Uncracked shaft time history; (b) Spectrum for (a); (c) Cracked shaft time history; (d) Spectrum for (c). Spectral response scale factor = 1/500.

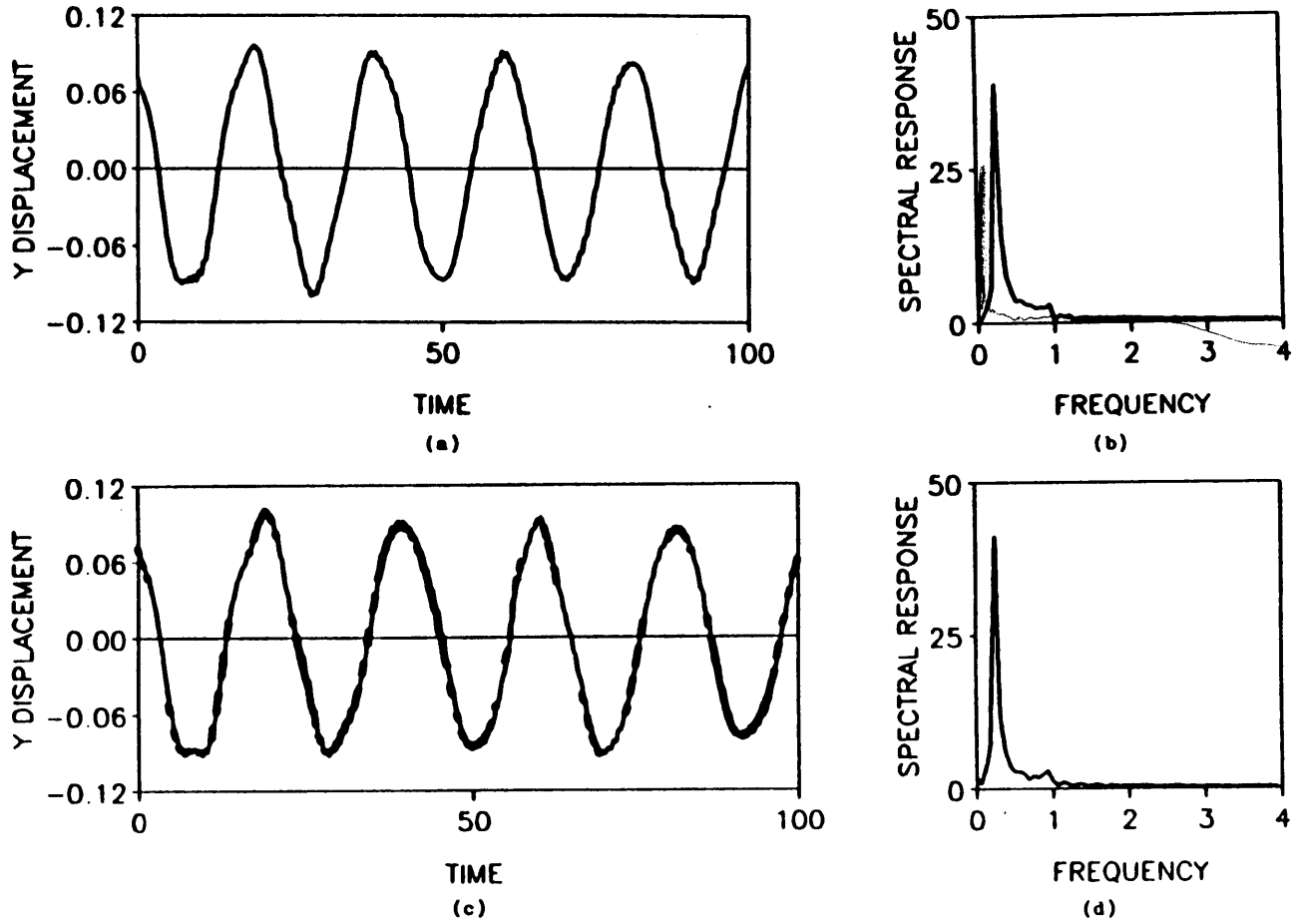

Figure 3.12. Comparison of uncracked and cracked shafts (free vibration, Case A) - $\tilde{Y}$: (a) Uncracked shaft time history; (b) Spectrum for (a); (c) Cracked shaft time history; (d) Spectrum for (c). Spectral response scale factor = 1/500.

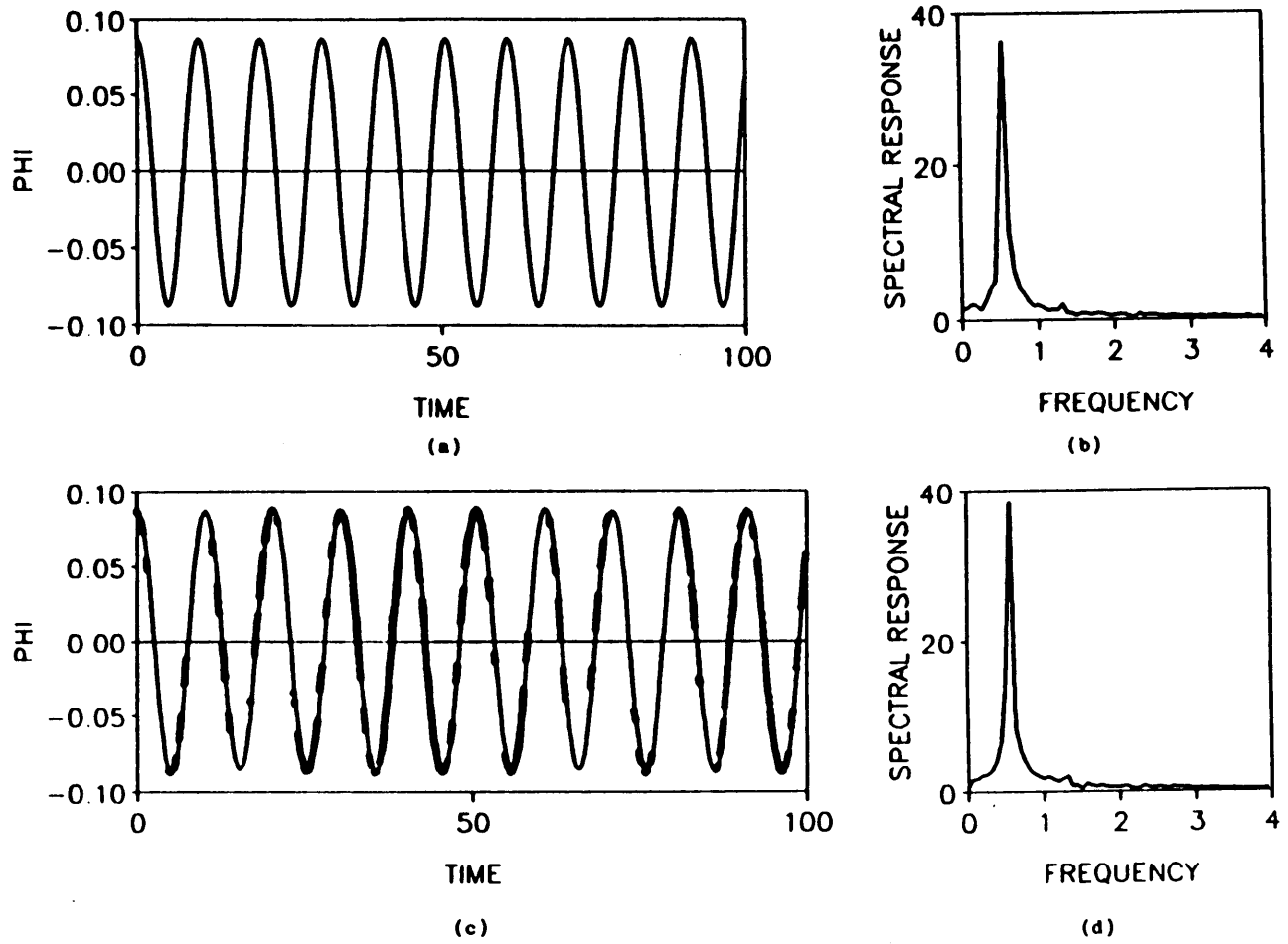

Figure 3.13. Comparison of uncracked and cracked shafts (free vibration, Case A) - $\tilde{\phi}$: (a) Uncracked shaft time history; (b) Spectrum for (a); (c) Cracked shaft time history; (d) Spectrum for (c). Spectral response scale factor = 1/500.

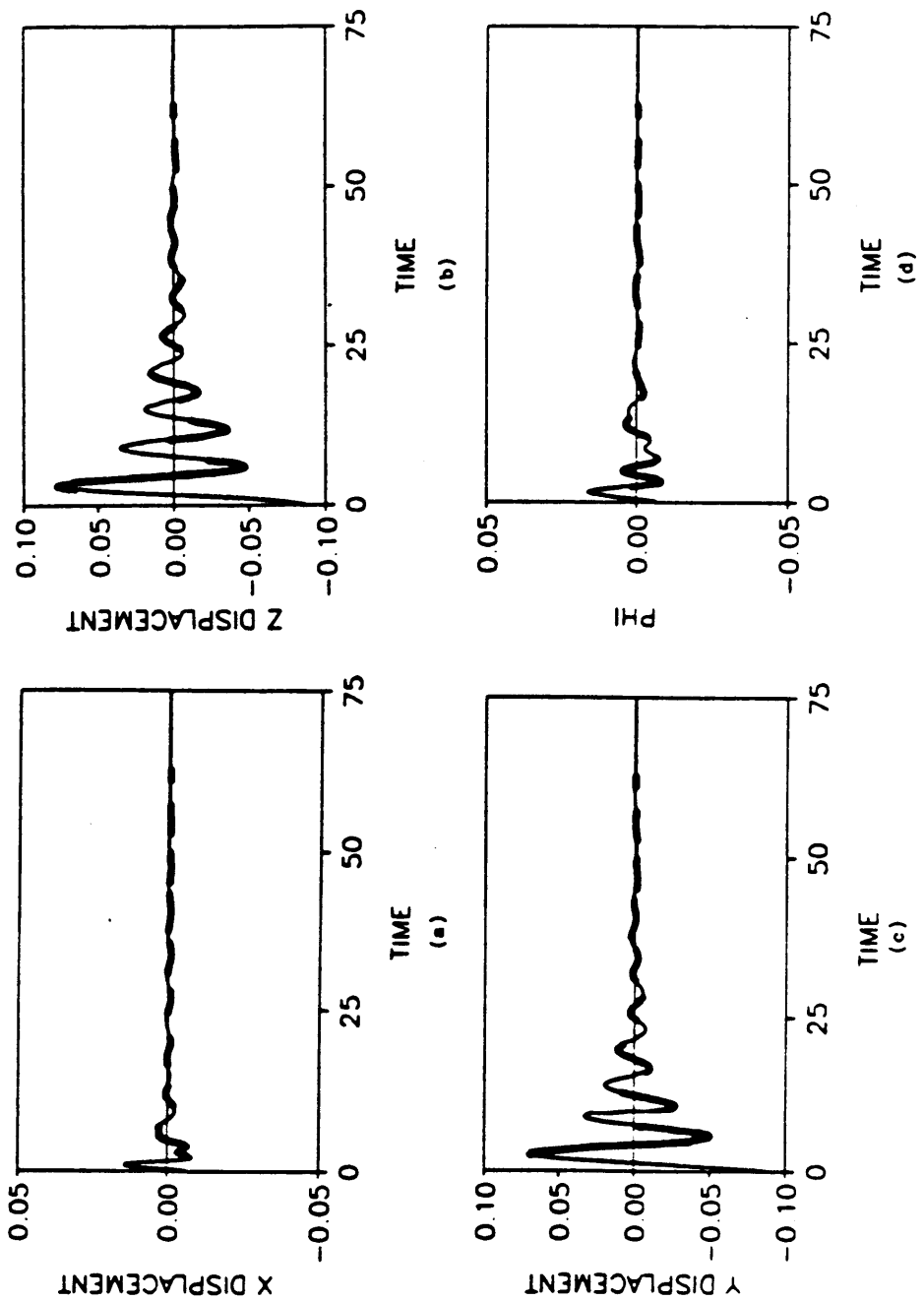

Figure 3.14. Effect of damping when $\tilde{c} = 0$: (a) Time history for $\tilde{X}$; (b) Time history for $\tilde{Z}$; (c) Time history for $\tilde{Y}$; (d) Time history for $\tilde{\phi}$.

introduces more frequencies into the motion. However, there doesn't appear to be any regularity in the new frequencies, i.e., they do not appear to be integer multiples or fractions of the natural frequency. Unfortunately, such behavior change is not isolated to cracked shafts with eccentricity. Figure 3.17 presents the behavior of $\tilde{\phi}$ for an uncracked shaft with eccentricity, with all other conditions identical to those in Figure 3.16. By comparing Figure 3.17 with Figure 3.13, it is obvious that the same type of change in behavior results for both cracked and uncracked shafts subject to mass unbalance. Hence, crack detection based on imposing mass eccentricity does not appear promising.

One final remark concerning mass eccentricity seems warranted here. Other investigators (for example, Schmied and Krämer, 1984; Kujath, 1986) also incorporate eccentricity into their models of cracked shafts. However, their models assume massless shafts; the inertia force terms of their models are derived from concentrated masses (disks) along the shaft. If the center of mass of the disk does not coincide with the geometric center of the shaft, mass unbalance results. Contrary to this, the shaft modelled in this thesis has a uniformly distributed mass and no concentrated disk masses. Intuitively, it seems appropriate that the results discussed here for nonzero $\tilde{e}$ are not very exciting since the mass unbalance is distributed over the shaft. If the model were modified to incorporate eccentric disk masses, more interesting behavior might result.

3.8 Cracked Shaft Subjected to Impact

In Chapter 2, it was observed that forcing the bar enabled one to determine whether or not a crack was present. If a crack was present, harmonics of the forcing frequency were observed in the spectrum (see Figure 2.13). In this chapter, the forcing of the system (due to gravity and/or unbalance) has proven not to be sufficient to create any change in the frequency spectrum of a cracked shaft. Therefore, additional forcing of the system might be required to create the changes described above.

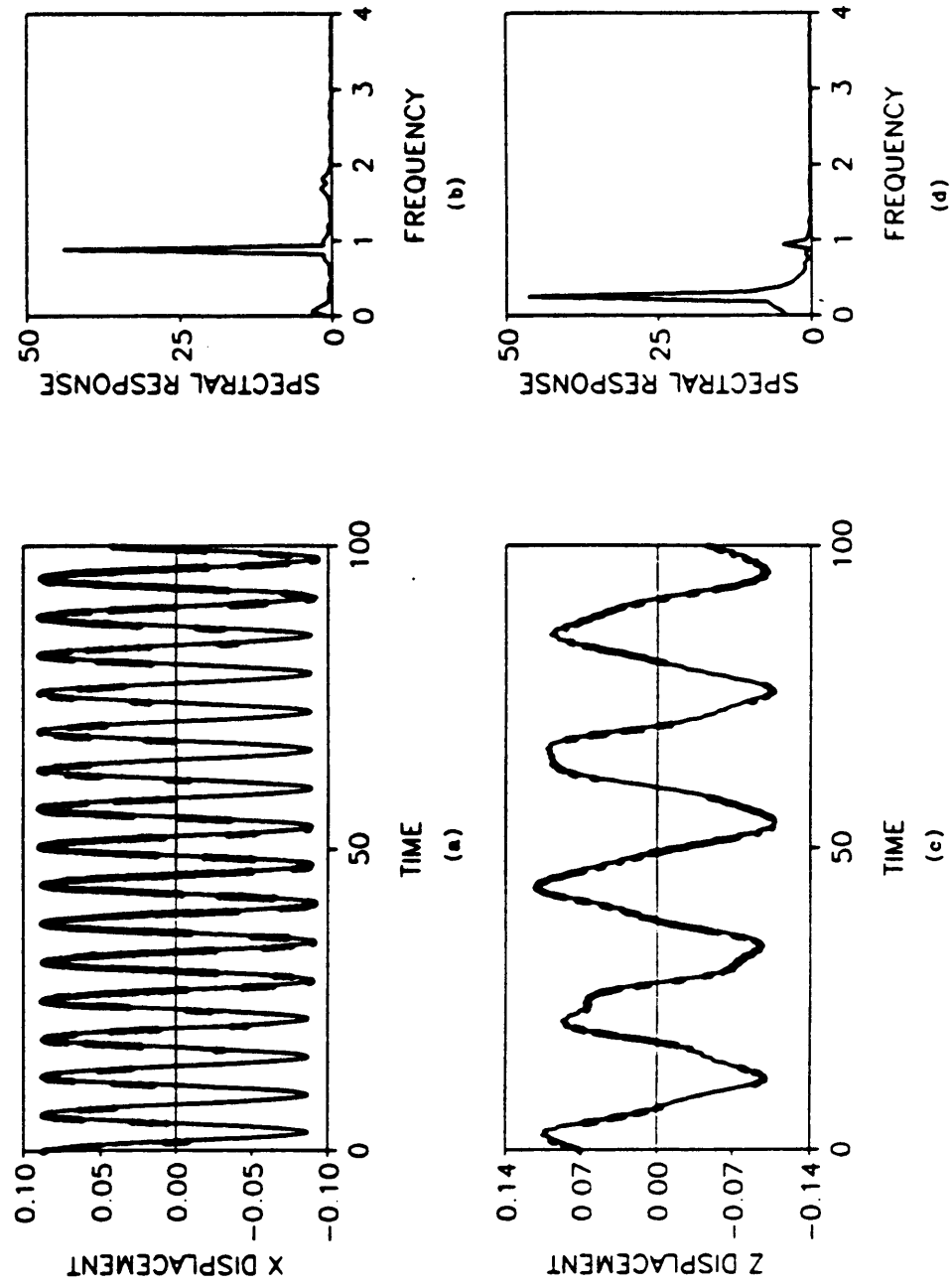

Figure 3.15. Behavior of $\tilde{X}$ and $\tilde{Z}$ for $\tilde{\epsilon} = 0.01$ (cracked shaft): (a) Time history for $\tilde{X}$; (b) Spectrum of (a); (c) Time history for $\tilde{Z}$; (d) Spectrum of (c). Spectral response scale factor = 1/500.

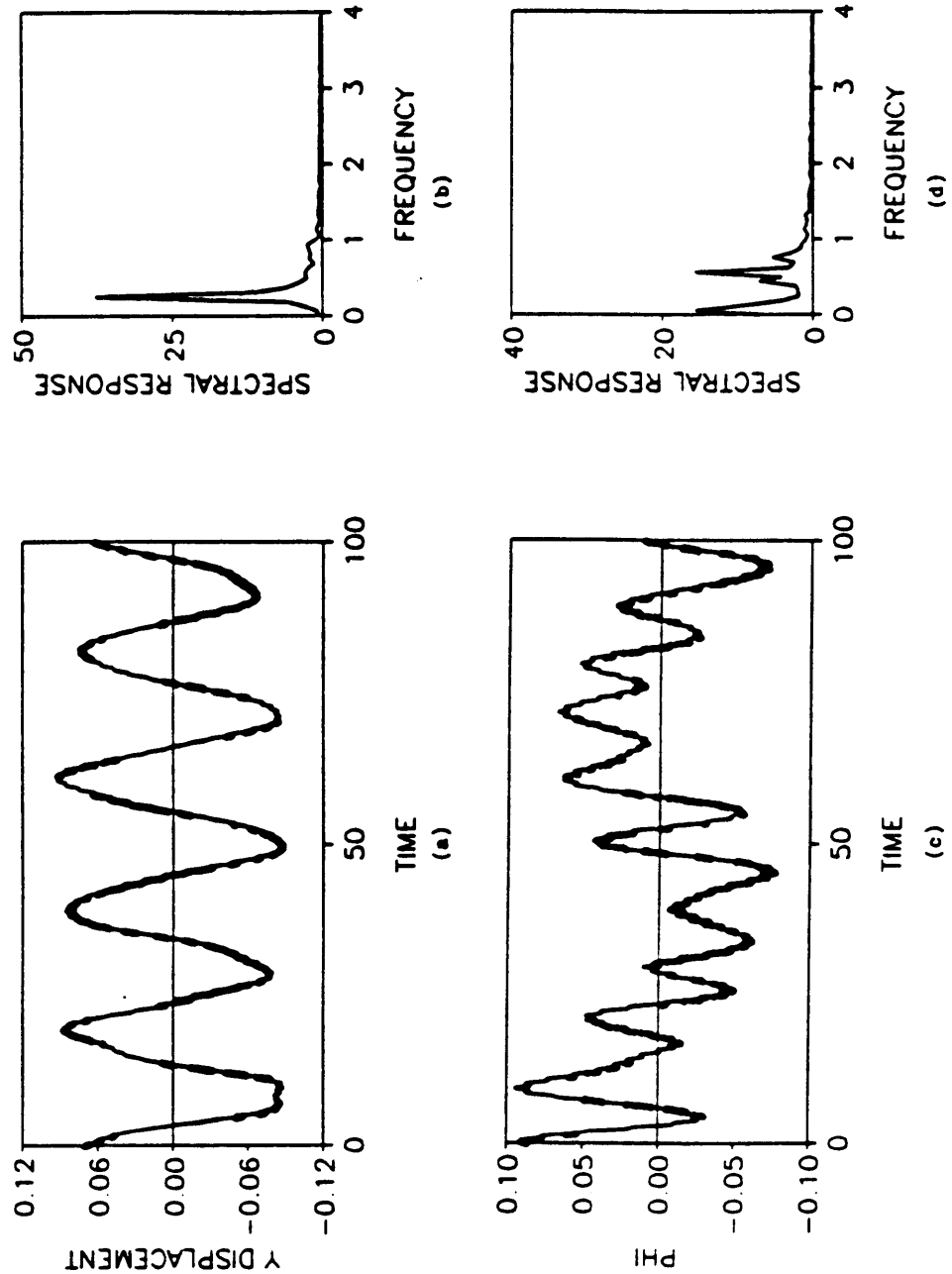

Figure 3.16. Behavior of $\tilde{Y}$ and $\tilde{\phi}$ for $\tilde{e} = 0.01$ (cracked shaft): (a) Time history for $\tilde{Y}$; (b) Spectrum of (a); (c) Time history for $\tilde{\phi}$; (d) Spectrum of (c). Spectral response scale factor = 1/500.

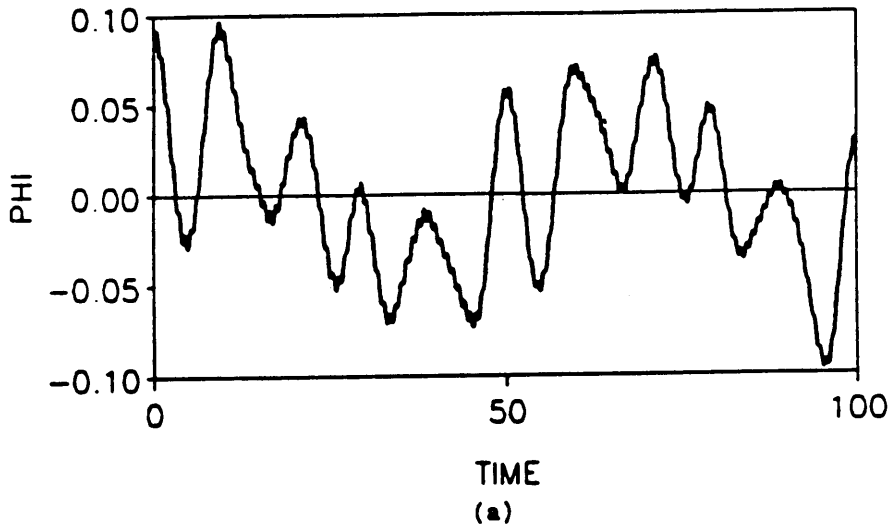

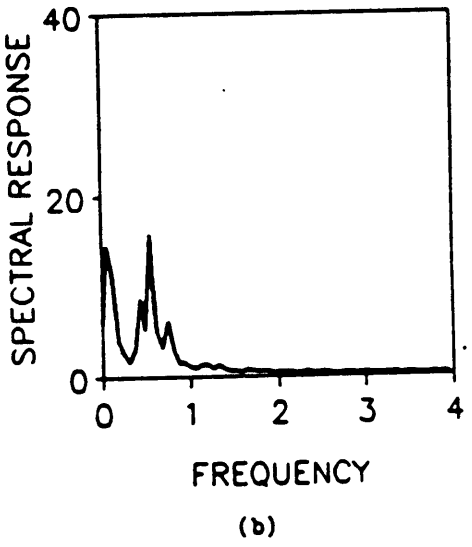

Figure 3.17. **Behavior of $\tilde{\phi}$ for $\tilde{\epsilon} = 0.01$ (uncracked shaft):** (a) Time history for $\tilde{\phi}$; (b) Spectrum of (a). Spectral response scale factor = 1/500.

There are several options by which the system may be "forced", such as by varying the rotating speed $\tilde{\Omega}$ in time or by applying external loads. However, it is desirable to force the system in such a manner that equations (3.5a-f) remain unchanged. If $\tilde{\Omega}$ becomes a function of time, the equations are no longer valid since they are derived under the assumption of constant rotating speed. If external forcing is applied (for example, an axial harmonic force), the boundary conditions change and the equations are no longer valid. However, if an impact loading is used in the axial direction, the boundary conditions still apply and no assumptions are violated. Therefore, impact loading appears to be the easiest way to force the system.

Figures 3.18 through 3.21 present the time history plots and corresponding spectra for $\tilde{X}$ and $\tilde{Z}$. Since the system is now forced, damping can be incorporated without the problems discussed in Section 3.6. Case B initial conditions are used, although the importance of the initial conditions is only in determining whether or not the crack is open or closed at $\tau = 0$. The impact is incorporated in the numerical integration routine by subtracting 0.1 from the velocity of the n = 1 component of $\tilde{u}$ when τ is a multiple of 5. This leads to an impact frequency ($\tilde{\omega}_I$) of 1.257. No eccentricity is permitted ($\tilde{e} = 0$) and $\tilde{\mu} = 2.99 \times 10^{-7}$. All other parameters assume their standard case values.

In Figures 3.18(a) and (b), the $\tilde{X}$ results for an uncracked shaft ($c_{ij} = 0$, $\tilde{d}_c = 0$) are presented, while Figures 3.18(c) and (d) show the results for a cracked shaft with a/D = 0.1. Figures 3.19(a) and (b) apply to $\tilde{X}$ for a/D = 0.2 and Figures 3.19(c) and (d) apply to $\tilde{X}$ for a/D = 0.3. From these graphs, it is observed that no significant change is seen in the $\tilde{X}$ motion when a crack is present. The presence of the impact loading is obvious by the steady-state periodic behavior. The dominant impact frequency and integer multiples of this frequency appear for both the cracked and uncracked shafts.

In Figures 3.20 and 3.21, the behavior of $\tilde{Z}$ is presented for the conditions of Figures 3.18 and 3.19, respectively. Unlike the $\tilde{X}$ results, the $\tilde{Z}$ results show a distinct difference between the cracked shaft and the uncracked shaft (similar results were obtained for $\tilde{Y}$). The uncracked spectrum shows a narrow range of frequencies corresponding to the decaying motion. The cracked shaft spectrum

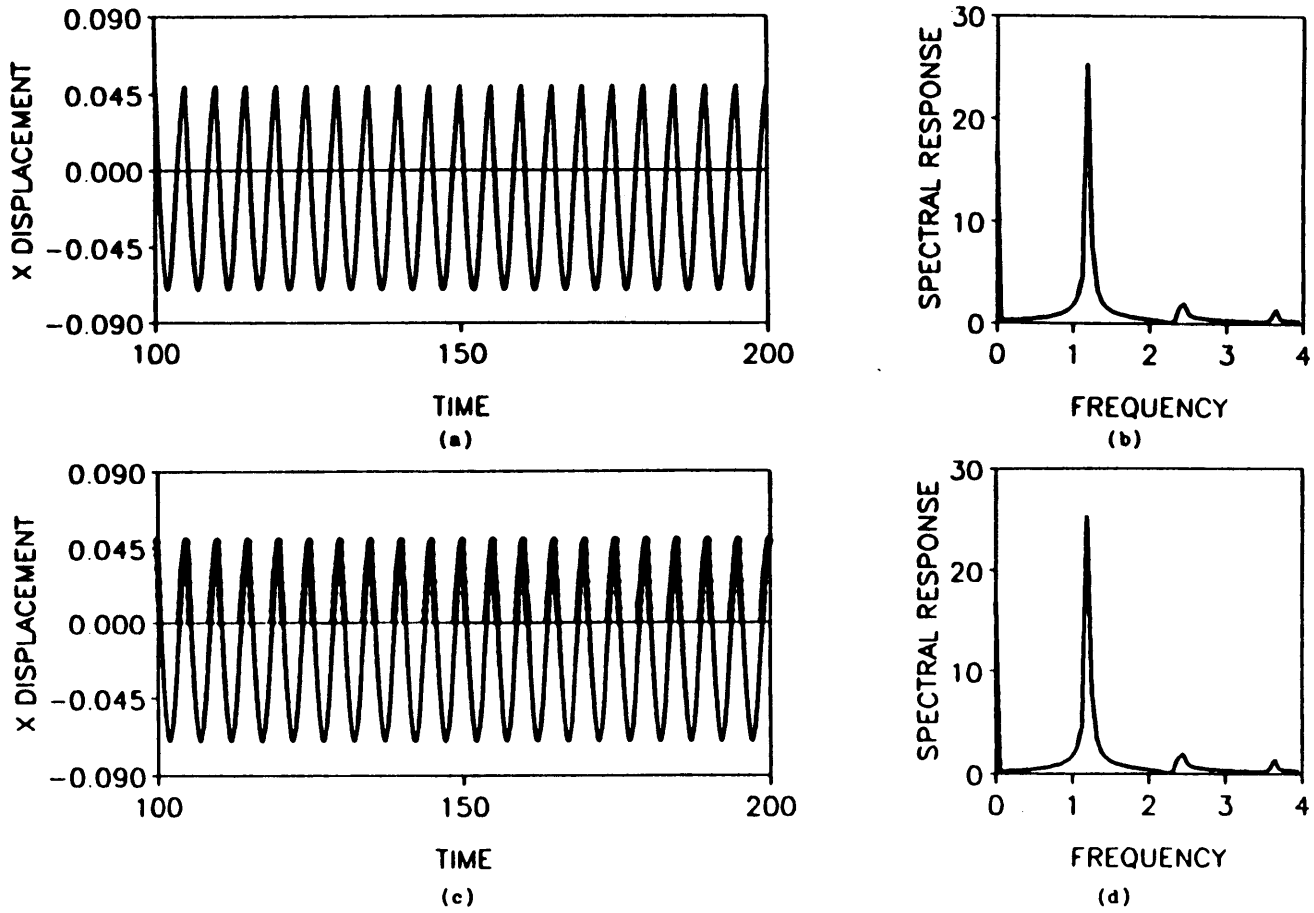

Figure 3.18. Behavior of $\tilde{X}$ for a/D = 0 and 0.1: (a) Time history for a/D = 0 (uncracked shaft); (b) Spectrum of (a); (c) Time history for a/D = 0.1; (d) Spectrum of (c). Spectral response scale factor = 1/500.

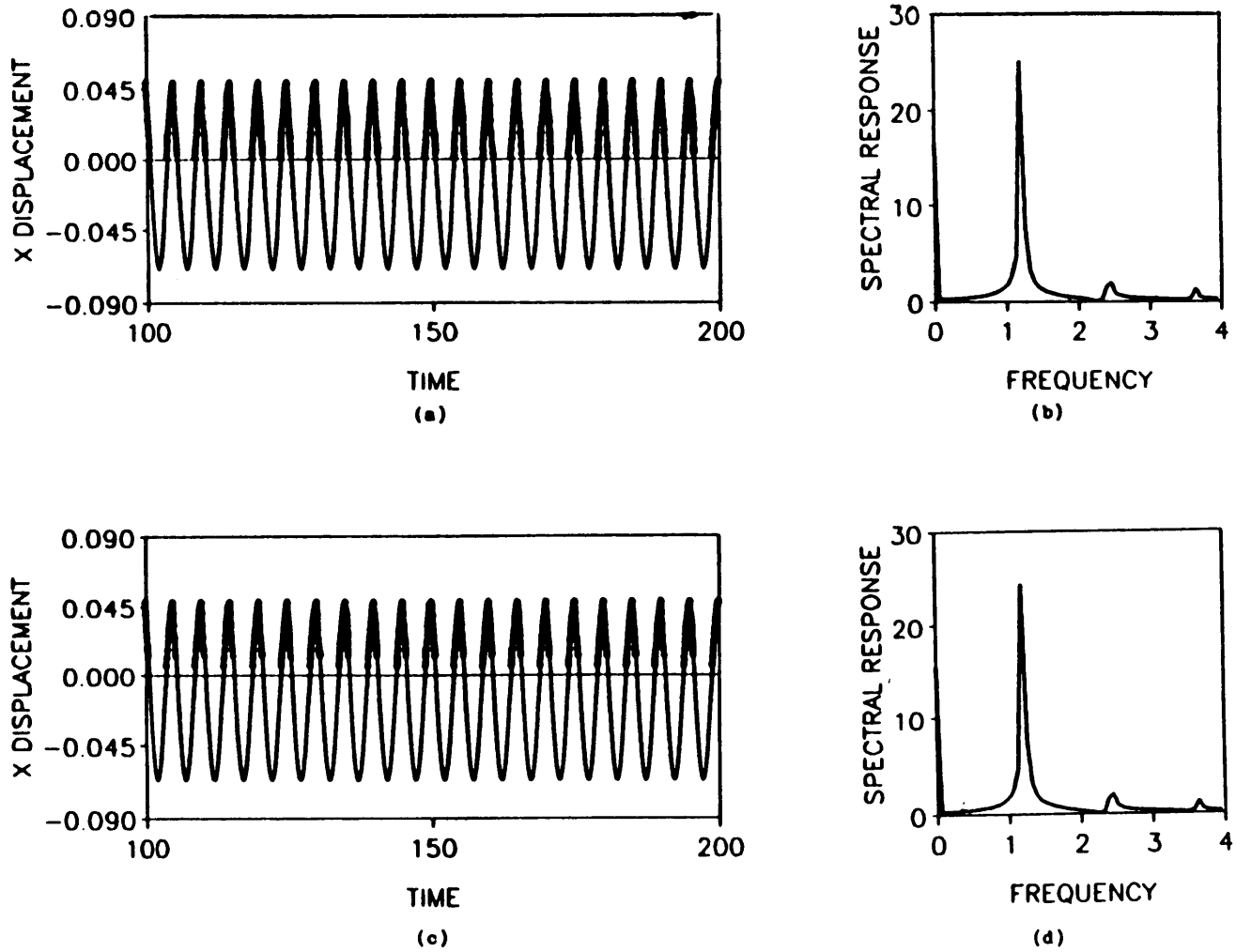

Figure 3.19. Behavior of $\tilde{X}$ for a/D = 0.2 and 0.3: (a) Time history for a/D = 0.2; (b) Spectrum of (a); (c) Time history for a/D = 0.3; (d) Spectrum of (c). Spectral response scale factor = 1/500.

shows three distinct frequencies, none of which correspond to the frequency peak for the uncracked shaft. The same three frequencies appear for the cracked shaft regardless of the a/D ratio. Note that unlike Chapter 2, the additional frequencies for the cracked shaft are not integer multiples of the first peak. Instead, the pattern of the frequencies suggests that the two higher frequencies represent the sum and difference, respectively, of the rotating frequency ($\tilde{\Omega} = 0.2$) and the impact frequency ($\tilde{\omega}_I = 1.257$). This was verified numerically by performing a spectral analysis of the time history from $\tau = 100$ to $\tau = 1100$ (not shown here). This range provided more points and therefore reduced the discretization error in the spectra procedure. The exact frequencies are $\tilde{\Omega} = 0.2$, $\tilde{\omega}_I - \tilde{\Omega} = 1.057$, and $\tilde{\omega}_I + \tilde{\Omega} = 1.457$; the improved spectral analysis gave peaks at 0.203, 1.061, and 1.460.

The presence of $\tilde{\Omega}$, $\tilde{\omega}_I - \tilde{\Omega}$, and $\tilde{\omega}_I + \tilde{\Omega}$ in the cracked shaft spectra can be explained by examining Figure 3.22, which provides the spectra ($100 < \tau < 1100$) for $\tilde{w}$ for both a/D = 0 (uncracked) and a/D = 0.2. The spectrum for the uncracked shaft reveals a range of small frequencies corresponding to the decaying motion. This explains the spectrum of Figure 3.20(b). For the cracked shaft, there are two distinct peaks at 0 and $\tilde{\omega}_I$. The same pattern occurs for $\tilde{v}$. Therefore, the steady-state motions of $\tilde{v}$ and $\tilde{w}$ might be approximated as the sum of a constant and a harmonic function with frequency $\tilde{\omega}_I$. If such approximations are valid, then equations (3.17) show that $\tilde{Z}$ and $\tilde{Y}$ will be composed of harmonic functions with frequencies of $\tilde{\Omega}$, $\tilde{\omega}_I - \tilde{\Omega}$, and $\tilde{\omega}_I + \tilde{\Omega}$ as shown in Figures 3.20 and 3.21.

By comparing Figure 3.20(b) with Figures 3.20(d) and Figures 3.21(b) and (d), it appears that the uncracked shaft is unaffected by the axial impact (i.e., the frequencies do not appear to be related to $\tilde{\omega}_I$). This can be explained by equations (3.1a-f). For the uncracked shaft, $\tilde{u}$ is uncoupled from any other displacement (since sag of the shaft is neglected in the model). Therefore, the effect of an axial impact is not felt by any other displacement. This is the reason for the narrow range of frequencies (within the one "peak") which are related to the frequencies of the decaying motion; the impact frequency is not present. However, when a crack is present, $\tilde{u}$ becomes coupled with $\tilde{\beta}$, which in turn is coupled with $\tilde{w}$ and $\tilde{v}$. Therefore, the effect of the axial impact is transmitted

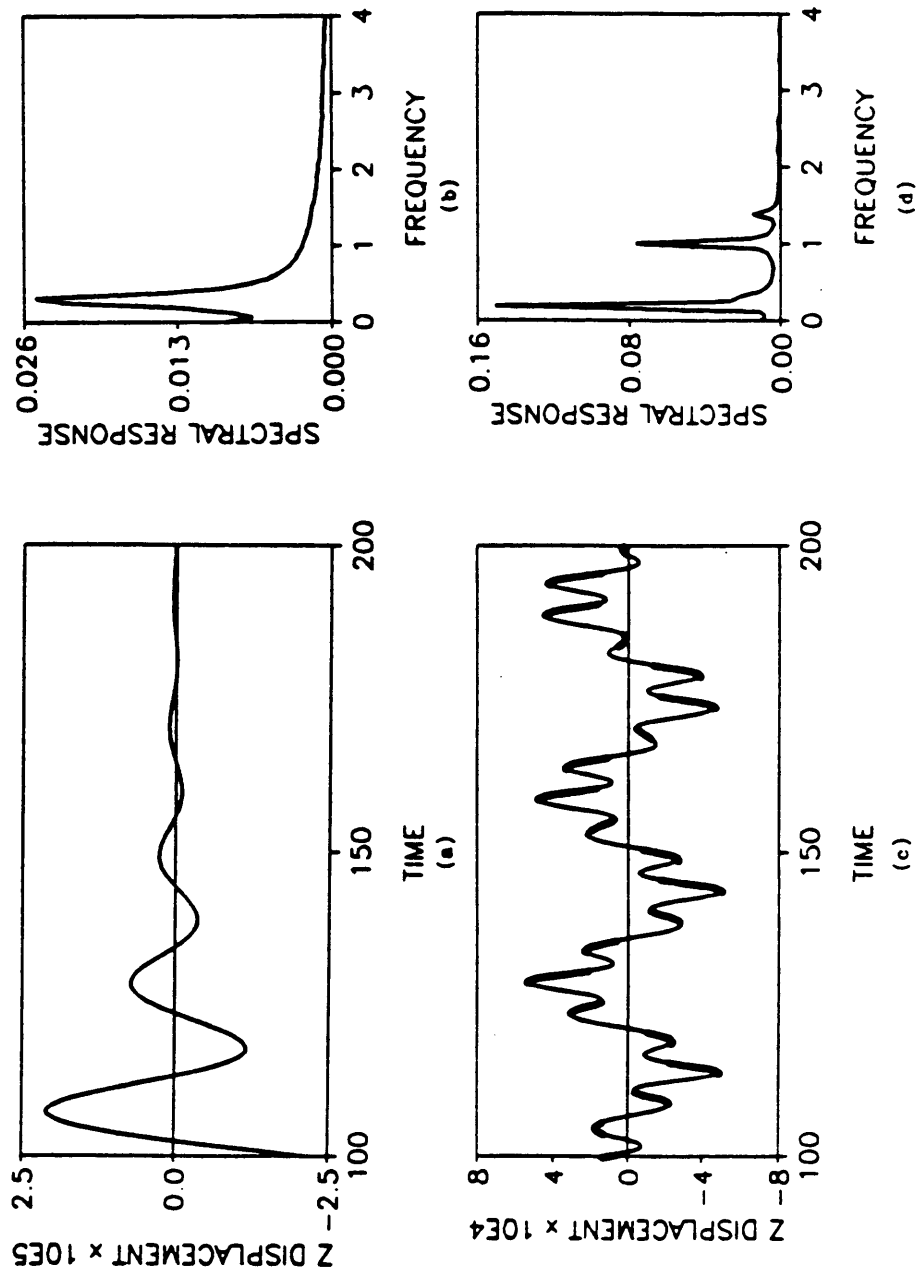

Figure 3.20. Behavior of $\tilde{Z}$ for a/D = 0 and 0.1: (a) Time history for a/D = 0 (uncracked shaft); (b) Spectrum of (a); (c) Time history for a/D = 0.1; (d) Spectrum of (c). Spectral response scale factor = 1/500.

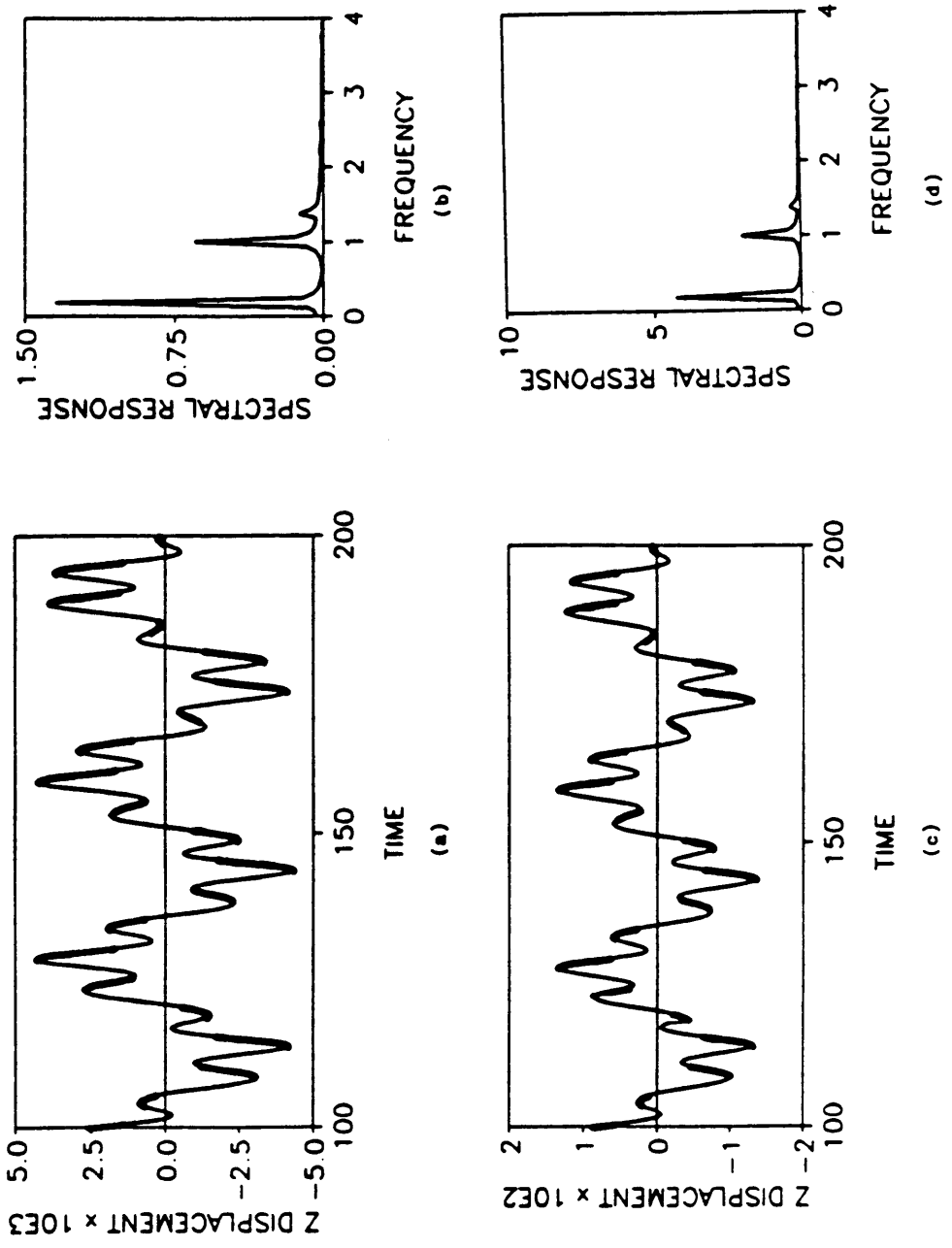

Figure 3.21. Behavior of $\tilde{Z}$ for a/D = 0.2 and 0.3: (a) Time history for a/D = 0.2; (b) Spectrum of (a); (c) Time history for a/D = 0.3; (d) Spectrum of (c). Spectral response scale factor = 1/500.

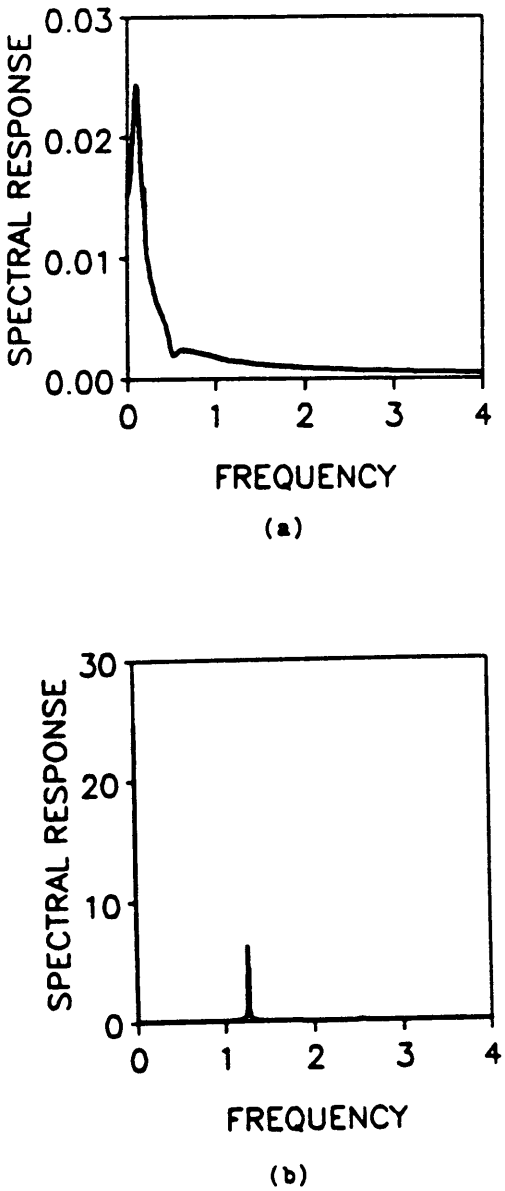

Figure 3.22. Spectra of $\tilde{w}$ for uncracked and cracked shaft: (a) Uncracked shaft; (b) Cracked shaft (a/D = 0.2). Spectral response scale factor = 1/5000.

to the $\tilde{w}$ and $\tilde{v}$ motions, which then comes into $\tilde{Z}$ by equations (3.17). As discussed above, the cracked shaft spectra show three frequencies which are related to the impact frequency, $\tilde{\omega}_I$, and the rotating frequency, $\tilde{\Omega}$. The same three frequencies appear regardless of the a/D ratio of the cracked shaft.

As a final observation, note how the magnitude of the $\tilde{Z}$ motion (steady-state) increases with a/D, with a corresponding increase in spectral response amplitude. Similar results were obtained for the horizontal motion, $\tilde{Y}$, and are not shown here. This relationship is presented in Figure 3.23. The open circles correspond to the actual data points and a smooth curve is fit through these points. It is significant to note that the amplitude changes dramatically with crack depth.

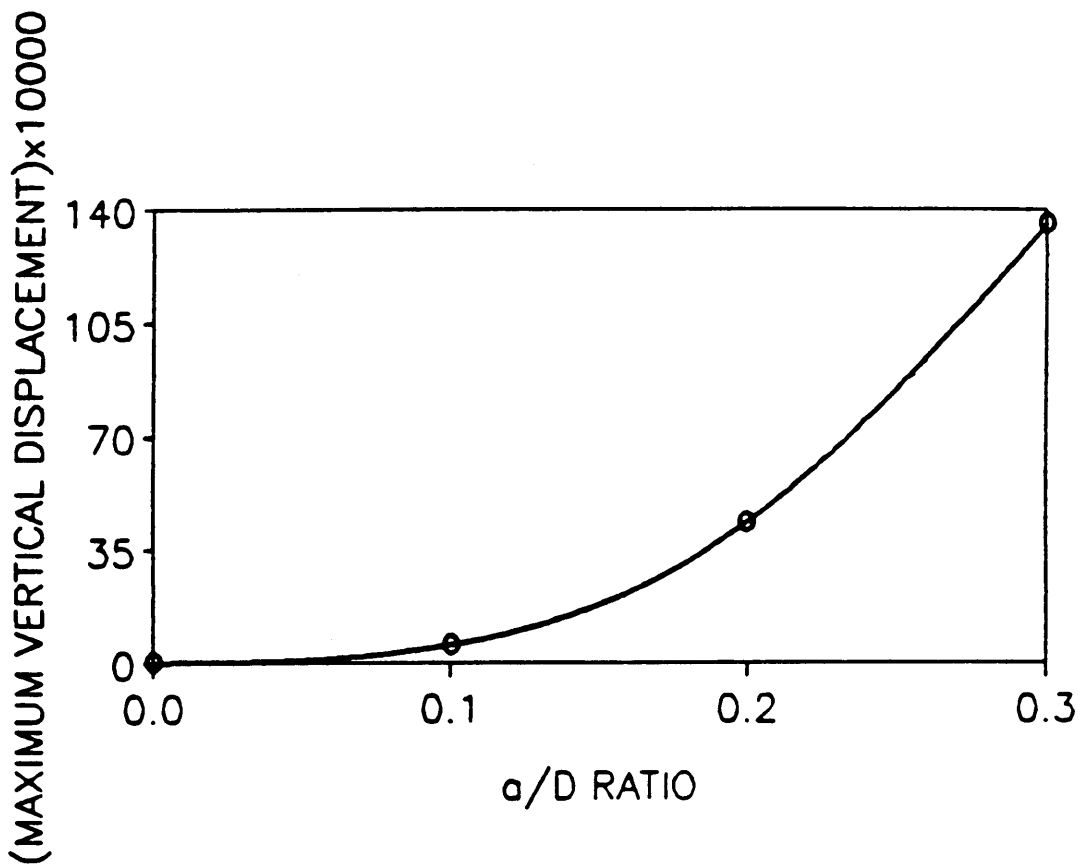

Figure 3.23. Maximum steady-state $\tilde{Z}$ vs. a/D: Note the nonlinear increase in $\tilde{Z}$ as a/D increases.

Chapter 4

Conclusions/Future Research

4.1 Conclusions

This thesis has considered the problem of crack detection in structural members from a purely mathematical standpoint. The research has focused on how the presence of a crack affects the vibrational behavior. Two cases were investigated: the longitudinal vibration of a cracked bar and the coupled vibrations of a cracked, rotating, Timoshenko shaft. In both cases, Galerkin's Method was used to obtain approximate solutions to the equations of motion. These approximate solutions were then used to investigate the influence of crack position, crack depth, forcing frequency, and other parameters on the resulting behavior. Spectral analysis was used to observe the component frequencies of the motion, and a sensitivity analysis was conducted in the longitudinal case. The three conclusions outlined below were drawn from the results.

1) In the longitudinal vibration study (Chapter 2), it was observed that the assumption of an "always open" crack may not accurately reflect the vibrational behavior of a cracked bar. The influence of a breathing crack can be significant.

2) The sensitivity analysis of Chapter 2 concluded that the largest change in steady-state response (forced system) at the onset of cracking occurred at forcing frequencies just below the lowest natural frequency. However, at higher frequencies, the model predicted that the end deflection of the bar may actually decrease at the onset of cracking. This apparent inconsistency was observed to diminish as more terms were taken in the approximate solution.

3) As others have concluded, small cracks are very difficult to detect. The results presented here support this for unforced systems. However, forcing the system externally and monitoring the spectrum of the steady-state motion seems to provide a method of detecting cracks. A crack will introduce additional frequencies in the spectrum as compared to the spectrum of the uncracked system (see Figure 2.13 and Figure 3.19).

In conclusion, as Petroski (1981) noted, simple models cannot be expected to give an exact representation of behavior. However, they can provide insight and possibly indicate order of magnitude results. This has been the underlying goal of this research.

4.2 Future Research

This thesis has only "scratched the surface" of the problem of detecting cracks based on mathematical models. With the models and solutions presented here, there are many other combinations of parameters which should be investigated. This is especially true for the cracked rotating shaft. Future research efforts may want to consider the possibilities outlined below.

- In the rotating shaft study, only one crack position was used. The relationship between crack location and vibration behavior is important, as was observed in Chapter 2, and should be investigated.

• The rotating shaft equations are derived under the assumption of a constant angular speed. Nilsson (1982) comments that cracks are more evident when a rotor passes through resonance than during normal operation. Mayes and Davies (1980) note that "...it is now certain that examination of the changes in vibrational behavior of a machine during rundown will show the presence of a crack before the depth for catastrophic failure has been reached." Since the equations presented here are restricted, a future investigation might look into the derivation of the equations to see what modifications are needed to handle run-up and run-down.

• One of the major conclusions of this thesis is that some type of forcing of the system is required to enable one to detect a small crack. In the study of the cracked bar, external forcing was incorporated directly into the equations of motion. However, in the shaft study, the equations only provide forcing due to gravity and mass eccentricity. Therefore, it might prove interesting to develop equations of motion for the shaft which incorporate some type of external forcing. Possible choices for this forcing might include torsional, axial, or transverse loading.

• The shaft considered here is a "simply-supported" shaft, which is a highly idealized situation. Future research might improve the mathematical models presented here by considering the stiffness and damping properties of the supports, as was studied by Neilson and Barr (1988a, 1988b).

• The values of damping used here may or may not accurately reflect true operating conditions in practice. Future research might look into determining better values.

• In the impact study, only one impact magnitude and frequency was considered. Future research might look at how various impact magnitudes and frequencies affect the vibrational behavior and the corresponding frequency spectrum.

References

Bachschmid, N., Diana, G., and Pizzigoni, B., 1984, "The Influence of Unbalance on Cracked Rotors." *Vibrations in Rotating Machinery*, The Institution of Mechanical Engineers, Mechanical Engineering Publications Ltd, London, pp. 193-198.

Bapat, C.N., and Sankar, S., 1986, "Periodic and Chaotic Motions of a Mass-Spring System Under Harmonic Force" *Journal of Sound and Vibration*, Vol. 108, pp. 533-536.

Bert, C.W., and Gordaninejad, F., 1985, "Forced Vibration of Timoshenko Beams Made of Multimodular Materials." *Journal of Vibration, Acoustics, Stress, and Reliability in Design*, Vol. 107, pp. 98-105.

Chang, H.-Y., and Petroski, H.J., 1986, "On Detecting a Crack by Tapping a Beam" *International Journal of Pressure Vessels and Piping*, Vol. 22, pp. 41-55.

Choi, Y.-S., and Noah, S.T., 1987, "Nonlinear Steady-State Response of a Rotor-Support System." *Journal of Vibration, Acoustics, Stress, and Reliability in Design*, Vol. 109, pp. 255-261.

Choi, Y.-S., and Noah, S.T., 1988, "Forced Periodic Vibration of Unsymmetric Piecewise-Linear Systems." *Journal of Sound and Vibration*, Vol. 121, pp. 117-126.

Cowper, G.R., 1966, "The Shear Coefficient in Timoshenko's Beam Theory." *Journal of Applied Mechanics*, Vol. 33, pp. 335-340.

Dentsoras, A.J., and Dimarogonas, A.D., 1983, "Resonance Controlled Fatigue Crack Propagation in a Beam Under Longitudinal Vibrations." *International Journal of Fracture*, Vol. 23, pp. 15-22.

Dragani, R., and Repaci, A., 1979, "Influence of Viscous-Coulomb Damping on a System with Stops." *Mechanics Research Communications*, Vol. 6, pp. 283-288.

Feng, W.Q., Zhang, K.Y., and Wu, X.Y., 1989, "Research on the Change of Modal Parameters of a Beam Resulted From a Slot." *Proceedings, 7th International Modal Analysis Conference*, Las Vegas, Vol. II, pp. 1100-1108.

Gasch, R., Person, M., and Weitz, B., 1988, "Dynamic Behaviour of the Laval Rotor with a Cracked Hollow Shaft - A Comparison of Crack Models." *Vibrations in Rotating Machinery*, The Institution of Mechanical Engineers, Mechanical Engineering Publications Ltd, London, pp. 463-472.

Grabowski, B., 1980, "The Vibrational Behavior of a Turbine Rotor Containing a Transverse Crack." *Journal of Mechanical Design*, Vol. 102, pp. 140-146.

Grabowski, B, 1982, "Shaft Vibrations In Turbomachinery Excited by Cracks." *Rotordynamic Instability Problems in High-Performance Turbomachinery*, NASA Conference Publication 2250, pp. 81-97.

Grabowski, B., 1984, "The Vibrational Behaviour of a Rotating Shaft Containing a Transverse Crack." *Dynamics of Rotors - Stability and System Identification*, O. Mahrenholtz, ed., Springer-Verlag, Vienna, pp. 423-465.

Gudmundson, P., 1982, "Eigenfrequency Changes of Structures Due to Cracks, Notches or Other Geometrical Changes." *Journal of the Mechanics and Physics of Solids*, Vol. 30, pp. 339-353.

Gudmundson, P., 1983, "The Dynamic Behaviour of Slender Structures with Cross-Sectional Cracks." *Journal of the Mechanics and Physics of Solids*, Vol. 31, pp. 329-345.

Haisty, B.S., and Springer, W.T., 1985, "The Longitudinal Vibration Characteristics of a Uniform Beam Containing Two Symmetric Discontinuities." *Proceedings, 1985 SEM Spring Conference*, Las Vegas, pp. 389-395.

Henry, T.A., and Okah-Avae, B.E., 1976, "Vibrations in Cracked Shafts." *Vibrations in Rotating Machinery*, The Institution of Mechanical Engineers, Mechanical Engineering Publications Ltd, London, pp. 15-19.

Ichimonji, M., and Watanabe, S., 1988, "The Dynamics of a Rotor System with a Shaft Having a Slant Crack (A Qualitative Analysis Using a Simple Rotor Model)." *JSME International Journal*, Vol. 31, pp. 712-718.

Kirmser, P.G., 1944, "The Effect of Discontinuities of [*sic*] the Natural Frequency of Beams." *Proceedings, ASTM*, Vol. 44, pp. 897-904.

Kujath, M.R., 1986, "Identification of Fractures in Rotors." *Proceedings of the International Conference on Rotordynamics*, Tokyo, pp. 379-383.

Maezawa, S., 1961, "Perfect Fourier Series Solution for Feedback Control System with a Piecewise-Linear Element Subjected to Sinusoidal Input (An Example of Dead Zone Element)." *Bulletin of the JSME*, Vol. 4, pp. 499-507.

Maezawa, S., and Furukawa, S., 1973, "Superharmonic Resonance in Piecewise-Linear System (Effect of Damping and Stability Problem)." *Bulletin of the JSME*, Vol. 16, pp. 931-941.

Maezawa, S., Kumano, H., and Minakuchi, Y., 1980, "Forced Vibrations in an Unsymmetric Piecewise-Linear System Excited by General Periodic Force Functions." *Bulletin of the JSME*, Vol. 23, pp. 68-75.

Mayes, I.W., and Davies, W.G.R., 1980, "A Method of Calculating the Vibrational Behaviour of Coupled Rotating Shafts Containing a Transverse Crack." *Vibrations in Rotating Machinery*, The Institution of Mechanical Engineers, Mechanical Engineering Publications Ltd., London, pp. 17-27.

Miller, G.R., and Butler, M.E., 1988, "Periodic Response of Elastic-Perfectly Plastic SDOF Oscillator." *Journal of Engineering Mechanics*, Vol. 114, pp. 536-550.

Muszynska, A., 1982, "Shaft Crack Detection." *Proceedings, 7th Machinery Dynamics Seminar*, Edmonton, Canada, pp. 4.1-4.49.

Natsiavas, S., (a) "Periodic Response and Stability of Oscillators with Symmetric Trilinear Restoring Force." accepted for publication in *Journal of Sound and Vibration.*

Natsiavas, S., (b) "On the Dynamics of Oscillators with Bilinear Damping and Stiffness." submitted for publication.

Neilson, R.D., and Barr, A.D.S., 1987, "Spectral Features of the Response of a Rigid Rotor Mounted on Discontinuously Nonlinear Supports." *Proceedings, 7th World Congress on The Theory of Machines and Mechanisms*, Bautista, E., Garcia-Lomas, J., and Navarro, A., eds., Sevilla, Spain, Pergamon Press, Oxford, pp. 1799-1803.

Neilson, R.D., and Barr, A.D.S., 1988a, "Dynamics of a Rigid Rotor Mounted on Discontinuously Non-Linear Elastic Supports." *Proceedings of the Institution of Mechanical Engineers*, Vol. 202, No. C5, pp. 369-376.

Neilson, R.D., and Barr, A.D.S., 1988b, "Response of Two Elastically Supported Rigid Rotors Sharing a Common Discontinuously Non-Linear Support." *Vibrations in Rotating Machinery*, The Institution of Mechanical Engineers, Mechanical Engineering Publications Ltd, London, pp. 589-598.

Nilsson, L.R.K., 1982, "On the Vibration Behaviour of a Cracked Rotor." *Proceedings, Rotordynamic Problems in Power Plants*, Rome, International Federation for Theory of Machines and Mechanisms, pp. 515-524.

Papadopoulos, C.A., and Dimarogonas, A.D., 1987, "Coupled Longitudinal and Bending Vibrations of a Rotating Shaft with an Open Crack." *Journal of Sound and Vibration*, Vol. 117, pp. 81-93.

Papadopoulos, C.A., and Dimarogonas, A.D., 1988, "Coupled Longitudinal and Bending Vibrations of a Cracked Shaft." *Journal of Vibration, Acoustics, Stress, and Reliability in Design*, Vol. 110, pp. 1-8.

Petroski, H.J., and Glazik, J.L.,Jr., 1980, "Effects of Cracks on the Response of Circular Cylindrical Shells." *Nuclear Technology*, Vol. 51,pp. 303-316.

Petroski, H.J., 1981, "Simple Static and Dynamic Models for the Cracked Elastic Beam." *International Journal of Fracture*, Vol. 17, pp. 71-76.

Reiff, D.E., 1979, *The Acceleration of a Journal-Bearing Rotor Through the Critical Speed.*, Master's Thesis, Virginia Polytechnic Institute and State University, Blacksburg, Virginia.

Rogers, J.D., and Hollingshead, J.R., 1988, "Flaw Identification From Forced Vibration Testing." *Proceedings, 6th International Modal Analysis Conference*, Vol. II, Kissimmee, Florida, pp. 1414-1419.

Schmalhorst, B.K., 1988, "Numerical Simulation of Cracked Rotor's Vibrations Due to Measured Crack Shapes." *Proceedings, 2nd International Symposium on Transport Phenomena, Dynamics and Design of Rotating Machinery*, Vol. 2, Honolulu, pp. 271-285.

Schmied, J., and Krämer, E., 1984, "Vibrational Behaviour of a Rotor with a Cross-Sectional Crack." *Vibrations in Rotating Machinery*, The Institution of Mechanical Engineers, Mechanical Engineering Publications Ltd, London, pp. 183-192.

Shaw, S.W., 1985a, "The Dynamics of a Harmonically Excited System Having Rigid Amplitude Constraints (Part 1: Subharmonic Motions and Local Bifurcations)." *Journal of Applied Mechanics*, Vol. 52, pp. 453-458.

Shaw, S.W., 1985b, "The Dynamics of a Harmonically Excited System Having Rigid Amplitude Constraints (Part 2: Chaotic Motions and Global Bifurcations)." *Journal of Applied Mechanics*, Vol. 52, pp. 459-464.

Shaw, S.W., 1986, "On the Dynamic Response of a System with Dry Friction." *Journal of Sound and Vibration*, Vol. 108, pp. 305-325.

Shaw, S.W., and Holmes, P.J., 1983, "A Periodically Forced Piecewise-Linear Oscillator." *Journal of Sound and Vibration*, Vol. 90, pp. 129-155.

Skrikerud, P.E., and Bachmann, H., 1986, "Discrete Crack Modelling for Dynamically Loaded, Unreinforced Concrete Structures." *Earthquake Engineering and Structural Dynamics*, Vol. 14, pp. 297-315.

Springer, W.T., Lawrence, K.L., and Lawley, T.J., 1987, "The Effect of a Symmetric Discontinuity on Adjacent Material in a Longitudinally Vibrating Uniform Beam." *Experimental Mechanics*, Vol. 27, pp. 168-171.

Thompson, J.M.T., Bokaian, A.R., and Ghaffari, R., 1983, "Subharmonic Resonances and Chaotic Motions of a Bilinear Oscillator." *IMA Journal of Applied Mathematics*, Vol. 31, pp. 207-234.

Thompson, J.M.T., and Ghaffari, R., 1983, "Complex Dynamics of Bilinear Systems: Bifurcational Instabilities Leading to Chaos." *Collapse: The Buckling of Structures in Theory and Practice*, Thompson, J.M.T. and Hunt, G.W., eds., Cambridge University Press, Cambridge, England, pp. 161-174.

Thompson, J.M.T., and Elvey, J.S.N., 1984, "Elimination of Sub-Harmonic Resonances of Compliant Marine Structures." *International Journal of Mechanical Sciences*, Vol. 26, pp. 419-426.

Thompson, J.M.T., and Stewart, H.B., 1986, *Nonlinear Dynamics and Chaos*, John Wiley and Sons, Chichester, England, pp. 291-309.

Thomson, W.J., 1949, "Vibration of Slender Bars with Discontinuities in Stiffness." *Journal of Applied Mechanics*, Vol. 17, pp. 203-207.

Wang, W., and Zhang, A., 1987, "Sensitivity Analysis in Fault Vibration Diagnosis of Structures." *Proceedings of the 5th International Modal Analysis Conference*, Vol. 1, pp. 496-501.

Watanabe, T., 1984, "Forced Vibration of Nonlinear System with Symmetrical Piecewise-Linear Characteristics." *Bulletin of the JSME*, Vol. 27, pp. 1493-1498.

Wauer, J., (a), "On the Dynamics of Cracked Rotors - A Literature Survey.", accepted for publication in *Applied Mechanics Reviews*.

Wauer, J., (b), "Modelling and Formulation of Equations of Motion for Cracked Rotating Shafts.", accepted for publication in *International Journal of Solids and Structures.*

Wen, B.C., and Wang, Y.B., 1988, "Theoretical Research, Calculation and Experiments of Cracked Shaft Dynamic Response." *Vibrations in Rotating Machinery*, The Institution of Mechanical Engineers, Mechanical Engineering Publications Ltd, London, pp. 473-478.

Zastrau, B., 1985, "Vibration of Cracked Structures." *Archives of Mechanics*, Vol. 37, pp. 731-743.

Bibliography

Bachschmid, N., 1983, "A Method for Calculating the Dynamic Behaviour of Cracked Shafts." *Proceedings, 6th International Federation for Theory of Machines and Mechanisms Conference*, Vol. 2, New Delhi, pp. 1343-1346.

Bently, D.E., and Muszynska, A., 1986, "Early Detection of Shaft Cracks on Fluid-Handling Machines." *Proceedings, International Symposium on Fluid Machinery Troubleshooting*, American Society of Mechanical Engineers, PWR-Vol. 2, pp. 53-58.

Bosmans, R.F., 1985, "Cracked Rotor Demonstration." *Instability in Rotating Machinery*, NASA Conference Publication 2409, pp. 443-446.

Christides, S., and Barr, A.D.S., 1984, "One-Dimensional Theory of Cracked Bernoulli-Euler Beams." *International Journal of Mechanical Sciences*, Vol. 26, pp. 639-648.

Dimarogonas, A.D., and Paipetis, S.A., 1983, *Analytical Methods in Rotor Dynamics*, Chapter 6, Applied Science Publishers, London.

Ehrich, F.F., 1987, "High Order Subharmonic Response of High Speed Rotors in Bearing Clearance." *Rotating Machinery Dynamics*, 11th Biennial Conference on Mechanical Vibrations and Noise, Muszynska, A. and Simonis, J.C., eds., Boston, American Society of Mechanical Engineers, New York, DE-Vol. 2, pp. 167-174.

Herbert, R.G., 1987, "Turbine-Alternator Run-Down Vibration Analysis: Automated Crack Detection." *Rotating Machinery Dynamics*, Vol. 2, 11th Biennial Conference on Mechanical Vibration and Noise, Boston, American Society of Mechanical Engineers, New York, DE-Vol. 2, pp. 631-636.

Inagaki, T., Kanki, H., and Shiraki, K., 1982, "Transverse Vibrations of a General Cracked-Rotor Bearing System." *Journal of Mechanical Design*, Vol. 104, pp. 345-355.

Ju, F.D., and Mimovich, M., 1986, "Modal Frequency Method in Diagnosis of Fracture Damage in Structures." *Proceedings, 4th International Modal Analysis Conference*, Los Angeles, Vol. 2, pp. 1168-1174.

Mayes, I.W., and Davies, W.G.R., 1976, "The Vibrational Behavior of a Rotating Shaft System Containing a Transverse Crack." *Vibrations in Rotating Machinery*, The Institution of Mechanical Engineers, Mechanical Engineering Publications Ltd, London, pp. 53-65.

Mayes, I.W., 1977, "Crack Propagation in Rotating Shafts." ASME paper 77-DET-164.

Mayes, I.W., and Davies, W.G.R., 1984, "Analysis of the Response of a Multi-Rotor-Bearing System Containing a Transverse Crack in a Rotor." *Journal of Vibration, Acoustics, Stress, and Reliability in Design*, Vol. 106, pp. 139-145.

Meirovitch, L., 1986, *Elements of Vibration Analysis*, 2nd ed., McGraw-Hill Book Company, New York.

Natsiavas, S., and Babcock, C.D., 1988, "Behavior of Unanchored Fluid-Filled Tanks Subjected to Ground Excitation." *Journal of Applied Mechanics*, Vol. 55, pp. 654-659.

Papadopoulos, C.A., and Dimarogonas, A.D., 1987, "Stability of Cracked Rotors in the Coupled Vibration Mode." *Rotating Machinery Dynamics*, 11th Biennial Conference on Mechanical Vibration and Noise, Boston, American Society of Mechanical Engineers, New York, DE-Vol.2, pp. 25-34.

Parekh, V.N., and Carlson, R.L., 1977, "Effects of a Localized Region of Damage on the Parametric Excitation of a Bar." *International Journal of Mechanical Sciences*, Vol. 19, pp. 547-553.

Rauch, A., 1985, "Shaft Cracking Supervision of Heavy Turbine Rotors by FMM Method." *Proceedings, 3rd International Modal Analysis Conference*, Vol. II, Orlando, pp. 714-722.

Rogers, G.W., Rau, C.A.,Jr., Kottke, J.J., and Menning, R.H., 1982, "Analysis of a Turbine Rotor Containing a Transverse Crack at Oak Creek Unit 17." *Rotordynamic Instability Problems in High-Performance Turbomachinery*, NASA Conference Publication 2250, pp. 33-44.

Shaw, J., and Shaw, S.W., 1989, "The Onset of Chaos in a Two-Degree-of-Freedom Impacting System." *Journal of Applied Mechanics*, Vol.56, pp. 168-174.

Tamura, A., Iwata, Y., and Sato, H., 1988, "Unstable Vibration of a Rotor with a Transverse Crack." *Vibrations in Rotating Machinery*, The Institution of Mechanical Engineers, Mechanical Engineering Publications Ltd, London, pp. 647-653.

Watanabe, T., 1978, "Forced Vibration of Continuous System with Nonlinear Boundary Conditions." *Journal of Mechanical Design*, Vol. 100, pp. 487-491.

The vita has been removed from the scanned document